Laser Cooled Rubidium Atoms in the $5D_{5/2}$ Level: Excitation, Photoionization and Collisions

Bruce C. Duncan, Ph.D.

University of Connecticut, 2001

A series of experiments is performed on cold ^{85}Rb atoms confined in a magneto-optical trap. A variation of Stimulated Raman adiabatic passage (STIRAP) is used to transfer population from the $5S_{1/2}$ ground state to the $5D_{5/2}$ state with an efficiency exceeding 80%. This process relies on moderately intense pulses arriving in the counterintuitive order, i.e., the upper transition ($5P \rightarrow 5D$) driven before the lower transition ($5S \rightarrow 5P$). There is reasonable agreement with computer simulations, excepting a marked discrepancy between measured intensities and those used in the simulations. With a large ensemble of 5D atoms available, the 5D photoionization cross section at four different laser wavelengths (1064, 788, 647 and 532 nm) is determined via trap loss measurements. The theoretical calculations agree well with the experimental results (17.7, 10.9, 7.6 and 5.2 Mb, respectively). An experiment to measure the 5S-5D collisional rate constant sets an order-of-magnitude upper bound of 10^{-10} cm^3/s, assuming all atoms are 5S-5D pairs.

Laser Cooled Rubidium Atoms in the $5D_{5/2}$ Level: Excitation, Photoionization and Collisions

Bruce C. Duncan

B.A., Wesleyan University, 1974

M.A.R., Yale University, 1978

B.S., Worcester Polytechnic Institute, 1990

M.S., University of Connecticut, 1992

A Dissertation

Submitted in Partial Fullfilment of the

Requirements for the Degree of

Doctor of Philosophy

at the

University of Connecticut

2001

APPROVAL PAGE

Doctor of Philosophy Dissertation

Laser Cooled Rubidium Atoms in the $5D_{5/2}$ Level: Excitation, Photoionization and Collisions

Presented by

Bruce C. Duncan, B.A., M.A.R., B.S., M.S.

Major Advisor

Phillip L. Gould

Associate Advisor

Juha Javanainen

Associate Advisor

George Gibson

University of Connecticut

2001

AD DEI GLORIAM MAIOREM

et in

dilectissimam memoriam

parentum

meorum carissimorum

ACKNOWLEDGEMENTS

Phil Gould	Wenko Süptitz	Vicente Sanchez-Villicana
Tim Grove	Mali Balasubramaniam	Manasse Mbonye
Chris Wallace	Matt Wright	David Tong
Dick Mindek	Terry Kennedy	Paul Generous
Alexander Estrin	Anguel Nikolov	Ed Eyler
Steve Gensemer	Dong Ik Lee	Marin Pichler
Jared Bartholomew	Melanie Kittle	Mary Stone
Howard Hayden	Win Smith	Doug Hamilton
Juha Javanainen	George Gibson	Quentin Kessel
Richard Jones	Marijan Kostrun	Marwan Rasamny
Paul Lett	John Weiner	Dave Perry
Matt Mackie	Bob Erickson	Hossein Sadeghpour

Kim Giard Dawn Rawlinson Lorraine Smurra Cecile Stanzione

St. Mark's Chapel, the choir, my family and Angel

TABLE OF CONTENTS

1. Introduction 1

1.1 Prolegomena 1

1.2 History 5

1.3 Theory 8

2. Apparatus 14

3. Stimulated Raman Adiabatic Passage 28

3.1 Introduction and Theory 28

3.2 Set-up and Techniques 33

3.3 Results 44

4. Photoionization 59

4.1 Introduction and Theory 59

4.2 Contribution of the 6P State to the Measured PI Cross Section . . . 69

4.3 Set-up and Technique 79

4.4 Theoretical Calculations 82

4.5 Results 84

5. Collisions 88

5.1 Introduction and Theory 88

5.2 Determination of Density Regime 100

5.3 Set-up and Technique 103

5.4 Results 105

5.5 Conclusions 112

A. Calibration of the PMT 118

B. STIRAP Calculations 120
B.1 Obtaining the STIRAP Wave Function 120
B.2 Determining the Dipole Matrix Element 125
B.3 Relevant Clebsh-Gordan Coefficients 133
B.4 Code for STIRAP Simulations 138

C. IGOR Macros 144
C.1 Macros Used in the STIRAP Experiment 144
C.2 Macros Used in the Photoionization Experiment 148
C.3 Macros Used in the Collisions Experiment 152

D. LabVIEW Programs 167

LIST OF FIGURES

1.1 Some energy levels of rubidium. The solid lines indicate the STIRAP laser wavelengths. The detuning is indicated by Δ_1. Not all states or transitions are shown, and the drawing is not to scale. 3

1.2 The various three level system configurations. The $5S \rightarrow 5P \rightarrow 5D$ case in rubidium is a cascade system. 4

1.3 Zeeman-shifted energy levels and $\sigma+/\sigma-$ polarized light. A magnetic field proportional to x is assumed. The laser is detuned to ω_L. An atom going in the $+x$ direction will come into resonance with $\sigma-$ polarized light and will undergo a $\Delta m = -1$ transition. Repeated scattering of such photons will impart momentum to drive the atom back towards $x = 0$. 12

2.1 Schematic of trap apparatus. The vertical trap and repump beams are not shown. 16

2.2 AntiHelmholtz coils with circularly polarized light. 17

2.3 Energy levels for a ^{85}Rb trap. The trap laser light at 780 nm is slightly red-detuned from the cycling transition. Off-resonant excitation into the $5P_{3/2}$ F' = 3 state allows optical pumping of population into the $5S_{1/2}$ F = 2 ground state. The light at 795 nm provides repumping out of that ground state. 18

2.4 Laser current driver with negative polarity. 20

2.5 Circuit for the photodiode not employing subtraction, used with the two-photon spectroscopy for the 776 nm laser. 21

2.6 Circuit for the 80 MHz tunable AOM driver. Recent versions of the circuit have the components split into three separate circuits. . . . 23

2.7 Circuit for controlling the current to the antiHelmholtz coils. The manual switch is single pull, double throw. In the configuration as drawn, the antiHelmholtz coils receive current in two of the three switch settings. Were the power supply to be plugged into the alternate BNC, then the coils would receive current in only one setting. 24

3.1 Some energy levels of rubidium. The solid lines indicate the STIRAP laser wavelengths. The dotted lines indicate spontaneous emission from the various states. The detuning is indicated by Δ_1. Not all states or transitions are shown (the 4D is omitted), and the drawing is not to scale. 29

3.2 Time evolution of the atomic populations from simulations. The Rabi rates are $\Omega_1 = \Omega_3 = 6\Gamma$. The one-photon detuning is 7.5 Γ. The pulse widths are 33 ns. Inset (a) shows the evolution when the pulses are in the counter-intuitive order by 20 ns. Inset (b) is for coincident pulses. The solid line indicates the 5D state, the dashed the 5P and the dotted the 5S. The upper frames indicate the pulse timings: the solid line is Ω_1, the dotted line is Ω_3. 34

3.3 The timing scheme for the STIRAP experiment. The repump beam is on continuously. The downtime for the trap beam is typically 1 μs. The 776 nm STIRAP pulse is usually centered in the trap downtime. Here Δt indicates the delay between the STIRAP pulses. 36

3.4 Raw 780 nm fluorescence. 38

3.5 Averaged and normalized 780 nm fluorescence. Also note the non-linear character of the ramp voltage. 39

3.6 Raw 420 nm fluorescence. 40

3.7 Corrected 420 nm fluorescence with normalized 780 nm fluorescence and matched ramp voltages. 41
3.8 The layout of the optical spectrum analyzer and the two-photon, two-color spectroscopy used during the STIRAP and subsequent experiments. Where lines run alongside one another, the reader is to understand that the laser beams overlap. The high-power beams are the zero-order beams from their respective AOMs. 43
3.9 STIRAP efficiency at a counterintuitive delay of -20 ns, as a function of the 780 beam Rabi rate. The 776 Rabi rate is fixed at its highest value, corresponding to $I_3 = 9.3$ W/cm^2. The solid line is a fit described in the text. 45
3.10 STIRAP efficiency at a fixed delay of -20 ns, as a function of the 776 beam Rabi rate. The 780 Rabi rate is fixed at its highest value, corresponding to $I_1 = 7.9$ W/cm^2. The solid line is a fit described in the text. 46
3.11 Excitation efficiency for various 780 nm Rabi rates with the 776 nm Rabi rate held constant at its highest value. (a) Experimental, (b) from simulations. 48
3.12 Excitation efficiency for various 776 nm Rabi rates with the 780 nm Rabi rate held constant at its highest value. (a) Experimental, (b) from simulations. 49
3.13 5D population and photoionization (PI) probability per STIRAP pulse pair, according to simulations. The integrated PI probability is the sum of the product of the PI cross section times the instantaneous total PI flux due to the STIRAP pulses. Bear in mind that the pulses occur at 50 kHz. 50

3.14 STIRAP efficiency (from simulations) as a function of Ω_1 and Ω_3 for three different pulse delays: (a) pulses in the counterintuitive order by 20 ns; (b) coincident pulses; and (c) in the intuitive order by 20 ns. The contours reflect deciles of efficiency, lightest being the most efficient. 52

3.15 5D excitation (from simulations) by pulse delay and intensity, by summing individual m_F levels. $1/\Gamma = 27$ ns. The pulse width is the e^{-2} radius. 55

4.1 Loading curves showing the effect of cw photoionizing light (6.9 W/cm^2 at 788 nm). The data are fit to exponentials. The uppermost curve shows the trap fluorescence in the presence of STIRAP but the absence of PI. The second curve shows the effect of STIRAP and PI. Two curves lie near the ordinate axis. These are zero levels for each loading curve, recording all stray light while the magnetic field is off. 63

4.2 An example of analyzed data of PI by a cw source, in this case the 788 nm diode. The fraction of atoms remaining trapped is plotted against the intensity of the 788 nm beam. The line is a fit to Eqn. 4.5. 64

4.3 The total trap loss rate versus the intensity of the photoionizing 788 nm beam. The total loss rate is from loading curves. The line is a linear fit, yielding Γ_0 and from the slope the PI cross section. 65

4.4 The effect of the Nd:YAG pulse on trap fluorescence. The fit is an exponential. 67

4.5 Normalized trap population remaining as a function of Nd:YAG pulse fluence at 1064 nm. The curve is a fit to the complement of Eqn. 4.8. 68

4.6 The exponential decay of the Rb $5D_{5/2}$ population along with an ionizing pulse of light. The pulse can move in time with respect to the peak population (in the vicinity of the peak intensity of the second STIRAP pulse). As the ionizing pulse moves away from the STIRAP pulses, fewer atoms are left to be ionized, hence fewer atoms are lost from the trap. This change plotted against the ionizing pulse delay maps out the 5D lifetime. 70

4.7 Normalized trap loss as a function of separation between the STIRAP pulses and the 1064 nm Nd:YAG pulse. The fit is an exponential decay, yielding a lifetime of 245(16) ns. 71

4.8 Normalized trap loss as a function of separation between the STIRAP pulses and the 532 nm Nd:YAG pulse. Because the 6P can also be photoionized by 532 nm light, the fit includes contributions from that state as well, as is explained in the text. 72

4.9 ^{85}Rb energy levels with the four ionizing wavelengths used this experiment. The dashed lines indicate the smallest binding energies which can be photoionized by the respective wavelengths. 73

4.10 Some ^{85}Rb states and their branching ratios (which were taken from Ref. [45]). 74

4.11 Population in the 5D and 6P states as a function of time. The maximum 6P population at time $\tau_{6P} = 109$ ns is 12% of the 5D population at that time. 77

4.12 The sum of 5D and 6P populations weighted by their cross sections at 532 nm. The probability of photoionization is directly proportional to these curves. The curve labelled "6P" is used to fit the data in Fig. 4.8. 78

4.13 The cell MOT. The trap and repump beams also come in and out of the page. 80

4.14 The new arrangement of the optical isolator for the high-power 776 nm diode. 83

4.15 The $5D_{5/2}$ PI cross section versus photon energy above threshold. Left to right, the data points represent the measured cross sections at 1064, 788, 647 and 532 nm. The curve is the theoretical prediction as described in the text. 85

4.16 The effect of various combinations of linear polarization (with respect to the 780 nm STIRAP beam) of the 776 nm STIRAP beam and the 788 nm ionizing beam as a function of ionizing light intensity. 87

5.1 Distance R at which an atom is on resonance with a detuned laser beam. 95

5.2 Rb_2 5S + 5D fine structure. 98

5.3 Number density vs. number of atoms in the trap. As a trap loads, it can be in one of two possible regimes: the non-collective and the collective. In the non-collective regime the number density increases proportional to the number. The number density then levels off to a constant, n_0. This is the collective regime. The number increases while the density remains constant, in distinction to the non-collective regime, where both the number and the density are increasing. 101

5.4 Part (a): A schematic of the apparatus used in Melanie Kittle's measurements of trap density. Part (b): The timing relationship between function generators. The first function generator produces a square wave with a period of 16 s. This both switches the anti-Helmholtz coils on and off (and thus too the trap) and gates the second function generator. The latter controls the capturing of trap images taken by a CCD. 102

5.5 Trap number density vs number of atoms. The peak number of atoms is about 5 $\times 10^5$. In the constant density regime the number could be calculated from the volume: $N = n_c \pi^{3/2} w_x w_y w_z$, where w_i are the radii of the trap. In this experiment the number is determined via the trap fluorescence as acquired by the PMT. 104

5.6 Effect on the trap of sweeping (red to blue) the 776 nm laser. The upper trace is of the two-photon spectroscopy. The two peaks are for the F'=4 $\rightarrow$ F"=5 and F"=4 transitions, left to right. The splitting is about 9.5 MHz, and can also be detected in the lower trace, which is of the trap fluorescence. When the excitation beams are on two-photon resonance, the trap loses about 55% of its atoms. In this case most of the loss is due to photoionization. Also note that there is no structure further to the red. 106

5.7 Data from a run of the collision experiment. The top graph presents the number density, the middle graph the number of trapped atoms and the bottom graph the trap loading rate. In each graph the first five data points are for high density traps with no excitation. The second five are for low density traps with no excitation. In the top graph the succeeding points alternate between high and low density traps as the detuning goes from 0 to - 20 MHz in 5 MHz decrements. In the other two graphs groups of five data points alternate between high and low density traps as the detuning is similarly decremented. 107

5.8 Measured and calculated 5D loss rates. Circles represent measured values and squares the calculated. Filled markers represent the high density case and open ones the low density. 108

5.9 Trap loss rate due to photoionization (right axis) and loss rate due to collisions (left axis). The measured values are determined from trap loading rates. The calculated values are from Eqn. 5.47. . . . 109

5.10 Trap loss rate constant for various red detunings of the 776 nm high-power laser. Compare with Fig. 5.1. 111

LIST OF TABLES

3.1 Probability of decaying into the $5S_{1/2}$ F=2 ground state from various $5D_{5/2}$ hyperfine states. 56

4.1 States relevant to the photoionization experiment, their energy below the ionization threshold in cm^{-1} and eV, and the maximum wavelengths required to photoionize. 75

4.2 Measured and calculated $5D_{5/2}$ photoionization cross sections. The starred cross section is the theoretical prediction if all 11 $5D_{5/2}m_F$ levels were populated. 86

5.1 R, σ_{5D} and β from diverse approaches. 96

A.1 Power meter and photomultiplier tube readings. 118

A.2 Photons/second and photomultiplier tube calibration. 119

B.1 Rb 85 dipole moments, 5S, F=3 $\rightarrow$ 5P, F'=4. 125

B.2 Rb 85 dipole moments, 5P, F=4 $\rightarrow$ 5D, F'=3. 126

B.3 Rb 85 dipole moments, 5P, F=4 $\rightarrow$ 5D, F'=4. 127

B.4 Rb 85 dipole moments, 5P, F=4 $\rightarrow$ 5D, F'=5. 128

B.5 Rb 87 dipole moments, 5S, F=2 $\rightarrow$ 5P, F'=3. 129

B.6 Rb 87 dipole moments, 5P, F=3 $\rightarrow$ 5D, F'=2. 130

B.7 Rb 87 dipole moments, 5P, F=3 $\rightarrow$ 5D, F'=3. 131

B.8 Rb 87 dipole moments, 5P, F=3 $\rightarrow$ 5D, F'=4. 132

C.1 Time during ramp and its associated pulse delay. 145

Chapter 1

Introduction

1.1 Prolegomena

The use of lasers to cool and confine atoms now constitutes a major field within the larger area of atomic physics. Research in laser cooling has spawned both practical and fundamental results, including precision atomic clocks, atomic gyroscopes, atom optics and Bose-Einstein condensates. The pace of important research has been such that the Nobel Prize in physics has been awarded twice in recent years (1997 and 2001) to six major participants in the field. In particular to be noted is the development of magneto-optical traps (MOTs), which provide large numbers of ultracold atoms (i.e., T<1 mK). Previously, atomic beams or room-temperature vapor cells were used. Notable improvements by working with ultracold atoms include: there are no appreciable Doppler shifts, the sample size of atoms is fixed, and the loss of population in the trap can be used as an experimental probe.

Laser cooling and trapping techniques have also provided atomic physicists with new tools to work with in studies of collisions and ionization, the subject of the present study. Most previous experiments have involved the first excited atomic state. The research presented here extends this to a higher-lying excited state. We begin with an ultracold sample of rubidium atoms in a MOT, in which the atoms cycle between the 5S ground state and the 5P excited state. These atoms are

then excited to the 5D higher-excited state (see Fig. 1.1). We then characterize this state's photoionization and collision properties. The techniques to excite, to photoionize and to cause collisions, and the results therefrom, are the subjects of individual chapters.

Excitation of atoms is an interesting topic, both intrinsically and as a tool for other investigations in atomic physics. The method used in our research exploits the "strangeness" of quantum mechanics. One would intuitively suppose that the best method to populate the 5D state would be first to drive the atoms into the 5P state and from there go to the 5D, and this method does work (see for instance [1]). However, it turns out that going in the opposite order is more effective. This counter-intuitive order was first used in stimulated Raman adiabatic passage (STIRAP), a technique developed by Bergmann's group [2]. As a term "STIRAP" was first applied only to the transfer of population in a three level lambda system either in molecules [3,4] or atoms [5], but its use here will be in its extended sense to refer to adiabatic passage by counter-intuitive pulse order in any three level system (the states we will be using in rubidium are in a cascade system, also known as a ladder system; refer to Fig. 1.2). The STIRAP technique is able to transfer the ground state population to the excited state with near unit efficiency. It has two additional benefits in that it does not require exceptionally intense laser beams and that it does not populate the intermediate 5P state, a situation which simplifies data acquisition and analysis.

Once the atoms are in the 5D state, we measure the photoionization (PI) cross section. Photoionization plays a significant role in several areas, including state-selective atomic detection and plasmas. The latter include astrophysical and other low-temperature plasmas. Knowledge of the PI cross section is useful in testing theories of nonhydrogenic wave functions. We have an additional interest in PI,

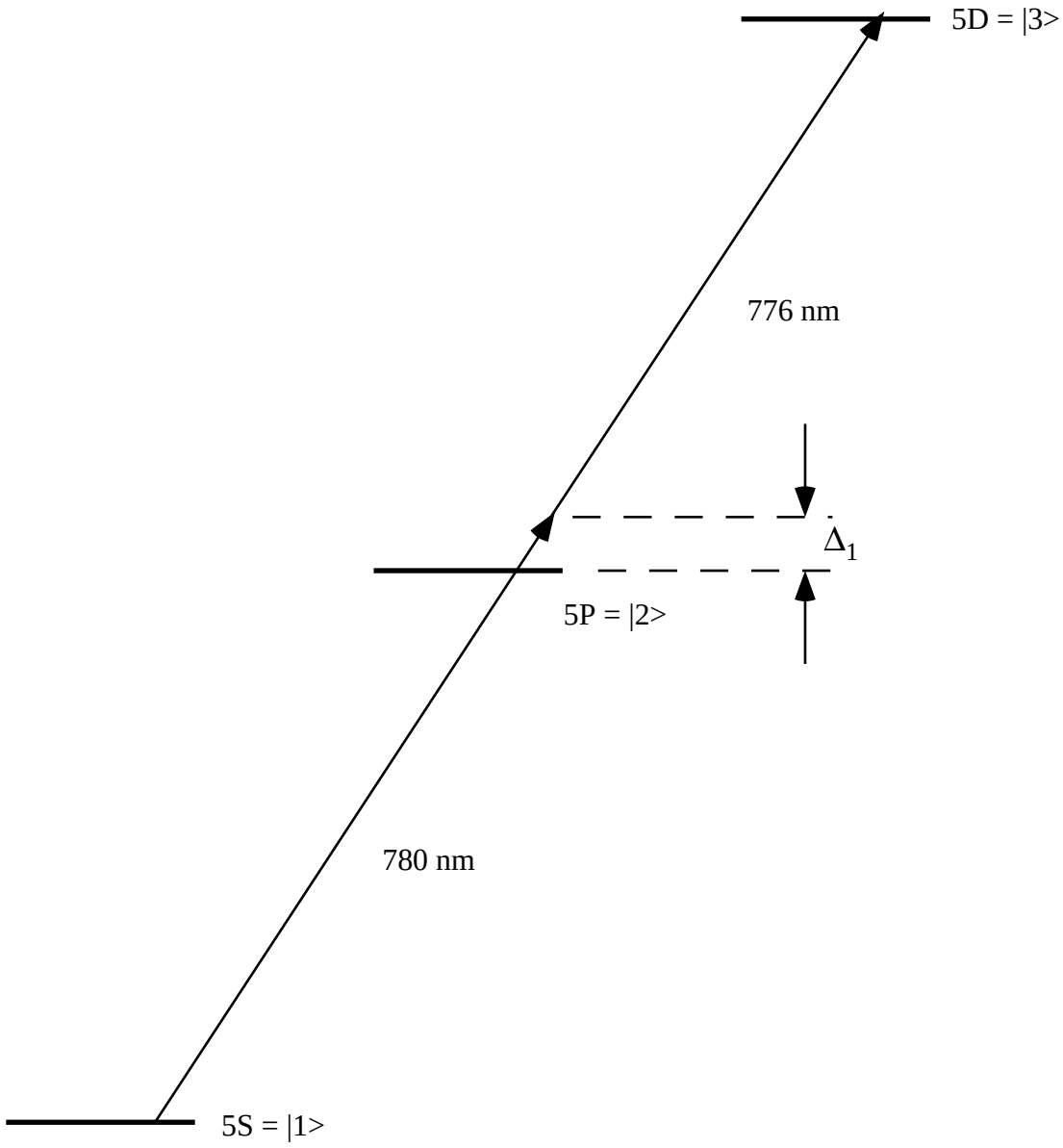

Fig. 1.1: Some energy levels of rubidium. The solid lines indicate the STIRAP laser wavelengths. The detuning is indicated by Δ_1. Not all states or transitions are shown, and the drawing is not to scale.

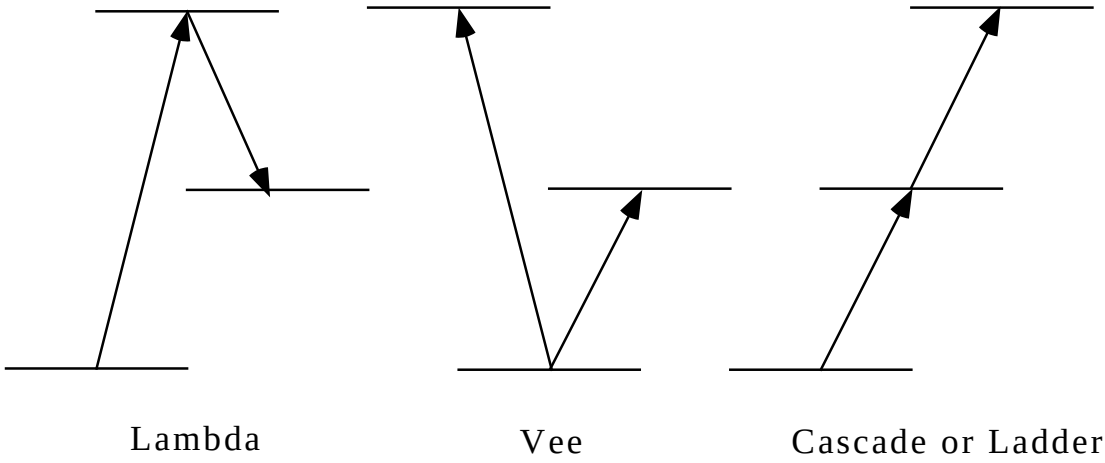

Fig. 1.2: The various three level system configurations. The $5S \rightarrow 5P \rightarrow 5D$ case in rubidium is a cascade system.

because the STIRAP pulses used to populate the 5D state can cause PI and thus cause the MOT to lose atoms. We must account for this loss when we investigate any other loss mechanism, including collisions.

The PI cross section depends on the wavelength of the ionizing radiation, so we use light at four different wavelengths. Measurements are performed with both continuous (cw) and pulsed laser light. Photoionization with cw light causes trap loss; hence, the trap loss rate is directly related to the ionization rate per atom. Once we have determined the ionization rate R_p, we obtain the cross-section from the formula [6]:

$$\sigma = \frac{h\nu}{I_p}\frac{R_p}{f}, \tag{1.1}$$

where σ is the photoionization cross section, h is Planck's constant, I_p is the intensity of the photoionizing beam, ν is its frequency, and f is the time-averaged excited-state (5D) fraction. With pulsed light photoionization causes an instantaneous loss of atoms from the trap. The fractional loss is related to the photoionization cross section, the pulse fluence and the instantaneous 5D population. As

the population in the 5D decays, the ionizing pulse can be varied in time, giving a method for measuring the 5D lifetime. Knowledge of the lifetime is important both for the study of collisions and for analysis of the PI data.

For ionizing light we use the Nd:YAG fundamental (1.06 μm) and its second harmonic (532 nm), a Kr laser at a wavelength of 647 nm and a diode at 788 nm. Although the cross section of the 5P state has been measured [6], to our knowledge no one has done so for the 5D before this work.

There have been several studies of ultracold collisions between atoms in 5S and 5P [7–13]. We investigate those between 5S and 5D, which is of interest because the interaction potential and lifetimes are qualitatively different from 5S-5P. In 5S-5P collisions the potential goes as R^{-3}, where R is the separation between the atoms. An important aspect of 5S-5P collisions is the relatively short lifetime of the 5P, which is about 27 ns. The case is quite different for 5S-5D collisions, where the potential goes as R^{-5}, and the 5D lifetime is considerably longer, 241 ns. The longer lifetime means that there is less chance for the 5D atom to decay during the collision.

1.2 History

One of modern science's first attributions of the mechanical effect of light on matter was Kepler's theory that light pressure caused comet tails to point away from the sun [15]. It wasn't until the early years of the twentieth century that experiments produced evidence for Maxwell's quantitative predictions on radiation pressure published nearly thirty years before. Einstein's work on the nature of the photon, Compton scattering of X-rays by electrons demonstrating the particulate nature of light, and Frisch's 1933 experiment deflecting a sodium beam by means of a sodium lamp were important breakthroughs, but it wasn't until lasers

were invented, in particular narrow-band tunable lasers, that dramatic progress could be made. In 1970 Ashkin proposed using lasers to produce high-intensity monochromatic light to deflect atoms [16] (he notes Frisch's work in passing) and in 1978 to trap atoms [17]. Three years before the latter paper two groups independently proposed the idea of laser cooling, Hänsch and Schawlow [18] to cool neutral atoms and Wineland and Dehmelt [19] to cool ions. In the years that followed, chirp-cooling and Zeeman-cooling techniques were used to slow atomic beams of neutral atoms, eventually achieving temperatures less than 100 mK (refer to [20]).

Around this same time magnetic traps for atoms were being developed, following the success in trapping neutrons and ions. These depended on inhomogeneous magnetic fields with a local minimum in the trapping region. Atoms with a magnetic moment $\boldsymbol{\mu}$ ($\boldsymbol{\mu}$ anti-parallel to the atom's total angular momentum $\mathbf{F}$) experience a force $\nabla(\boldsymbol{\mu} \cdot \mathbf{B})$ which, for states of $\mathbf{F}$ parallel to $\mathbf{B}$, i.e., $\boldsymbol{\mu}$ antiparallel to $\mathbf{B}$ and $m_F > 0$, will be attracted to the minimum location; these are called "weak field seekers." In addition to requiring cold, slow moving atoms (which could be provided by a slowed atomic beam), a stable trap also requires that the atoms' magnetic moments retain the same orientation with respect to the magnetic field. If the magnetic field has a zero minimum, then an atom passing through the zero point will experience an immediate change in direction of the field. The atomic spin will not be able to follow immediately and hence the atom will be lost from the trap. It isn't even necessary for the atom to pass directly through the zero point. In that vicinity the atomic spin can become 'disoriented' with respect to the magnetic field gradient and may undergo a Majorana spin flip, with the atom lost to the trap. The first successful magnetic trapping of neutral atoms was by the Phillips group in 1985 [21], slowing sodium atoms using a tapered solenoid and a cooling laser beam. For the trap itself they used two

coils in the antiHelmholtz configuration (see below in the theory section and refer to Fig. 2.2), an arrangement which has a zero point. There are arrangements of magnets, e.g., the Ioffe-Pritchard trap, which have a non-zero minimum and thus avoid the problem of having a zero point.

A different approach was being pursued at the same time as the magnetic traps, namely, the optical molasses [23] (1985) and the optical dipole trap [22] (1986). The latter depends on the atomic polarizability α_P and a laser field E combining to induce a dipole moment $\alpha_P E$ and a potential energy $-\frac{1}{2}\alpha_P E^2$. For a laser beam tuned below the first atomic resonance α_P is positive, and the atom is attracted toward high intensity. To reduce the heating of the atoms caused by the intense light, the lasers are detuned very far from the resonance. Alternatively, the laser can be detuned above the resonance (blue detuning) if the beam's transverse spatial profile is that of a doughnut, i.e., is dark in the middle. The optical molasses depends on a scattering force (from absorption and emission of photons) rather than on the dipole force. The low-intensity laser beams are arranged in three mutually orthogonal paths retroreflected back on themselves. The lasers are red detuned from resonance, which provides a net force opposing the velocity of the atom (see below in the theory section). Note that the viscous damping force $\mathbf{F} = -\alpha\mathbf{v}$ is velocity dependent. Slow moving atoms collect in the region where the beams intersect, but these atoms are not trapped, as there is no restoring force. Once they diffuse to the edge of the beams, they can escape the molasses.

In 1987 the first magneto-optical trap (MOT) was formed [24]. Its realization depended on previously mentioned techniques: the slowing of an atomic beam and the optical molasses. The zero point of a magnetic field created by antiHelmholtz coils was located near the intersection of three orthogonal laser beams reflected back on themselves, with the appropriate circular polarizations and red detuning

from the 589 nm resonance in sodium. The source of atoms was an atomic beam slowed by a frequency-swept laser. The general features of that apparatus are to be found in many other experimental setups, including that of this author's series of experiments. The two principal differences are that the 1987 experiment was performed with sodium, whereas here it is rubidium, and that the 1987 experiment loaded its trap from a slowed atomic beam, whereas here the atoms are loaded from the room-temperature background vapor in a glass cell [25].

There are several varieties of magneto-optical traps. The techniques described above have been adapted and added to new techniques to produce exciting new physics, chief of which is the creation in the laboratory of Bose-Einstein condensates. In addition to the many papers detailing this work, there have been sizable review articles (e.g., [26]) and recently a book ([20]). Further work is proceeding apace in this stimulating field of research, but enough has already been accomplished that Steven Chu, Claude Cohen-Tannoudji and William Phillips earned the 1997 Nobel Prize in Physics. They graciously acknowledged the efforts of their colleagues and predecessors by accepting the honor on behalf of the entire "laser cooling community."

1.3 Theory

The MOT depends on momentum transfer from light to atoms. The velocity of atoms follows a Maxwell-Boltzmann distribution, with a most probable velocity of hundreds of meters per second at room temperature (for ^{85}Rb at room temperature this thermal velocity is about 290 m/s). Light of an appropriate wavelength excites an atom from its ground state to an excited state. More properly, the probability that the atom will make this transition increases as the light's wavelength approaches the resonance wavelength. The width of the probability curve is called the linewidth, measured in rads/sec. The atom not only gains energy

from the absorbed photon, but it also gets a momentum kick of $\hbar\mathbf{k}$, where $\hbar$ is Planck's constant divided by 2π and $\mathbf{k}$ is the wavevector of the photon, 2π divided by the wavelength λ in the direction the photon was traveling. Before relaxing back to the ground state, the atom remains in the excited state for a characteristic lifetime, which is inversely proportional to the linewidth. When it relaxes, the excited atom spontaneously emits a photon in a random direction. Repeating the excitation/relaxation cycle many times gives the atom many kicks in the direction of the laser beam and many kicks in random directions. Averaging these latter random but symmetrically distributed events yields a momentum change of zero. Thus the net change in momentum is in the direction of the laser beam. This net change in momentum causes for a rubidium atom a change of velocity $\hbar\mathbf{k}/\mathbf{m}$ of about 6 mm/s per photon.

We wish to confine the atoms to a small locale at which their velocities will be small. This locale is the intersection of the six beams the MOT uses. To that end we place mirrors retroreflecting each of three orthogonal laser beams. The reflected beams nearly counterpropagate with the incoming beams, being slightly offset to reduce possible feedback problems with the trap laser. Instead of being on the atomic resonance the laser is now detuned a small amount, typically around a linewidth. In this series of experiments the laser is red detuned, i.e., the wavelength is increased. This is to take advantage of the Doppler effect. Consider the one dimensional case of an atom as it moves in the direction opposite to the incoming laser light. The light is blue shifted; hence, the wavelength approaches resonance and the likelihood that the atom will be excited is increased. As described above, many such excitations will slow the atom down. As it slows, the likelihood of absorbing a photon decreases. If the atom should then proceed in the opposite direction, the light reflected from the mirror will be more likely to drive a transition than the light coming directly from the laser. In this manner

the atom is slowed down and hence cooled. In terms of frequency this Doppler shift is to first order

$$\omega_D = -\mathbf{k} \cdot \mathbf{v}. \tag{1.2}$$

The Doppler shift approaches zero as the velocity approaches zero. Note that when $\mathbf{k}$ is in the direction opposite to $\mathbf{v}$, the minus sign gives a positive ω_D. Again consider the atom moving towards the laser. In frequency the red shifted beam is lower than the atomic resonance. Adding in the now positive ω_D brings the laser frequency nearer resonance. Under these same conditions the light reflected from the mirror has a $\mathbf{k}$ in the same direction as the atom's velocity; therefore, its ω_D is negative. Adding it to the beam's frequency causes the atom to see the light as being further from resonance. The atom is more likely to absorb photons more nearly on resonance than those further from resonance, i.e., it prefers the photons directly from the laser rather than those off the mirror. The magnitude of the force from each beam in this one dimensional Doppler cooling is obtained by multiplying the momentum per photon by the photon scattering rate for that beam. The net force is the sum, taking care to account for the sign:

$$F = \hbar k \frac{\Gamma}{2} \left(\frac{I/I_{sat}}{1 + 2I/I_{sat} + 4(\Delta - kv)^2/\Gamma^2} \right) - \hbar k \frac{\Gamma}{2} \left(\frac{I/I_{sat}}{1 + 2I/I_{sat} + 4(\Delta + kv)^2/\Gamma^2} \right). \tag{1.3}$$

Here Γ is the linewidth, I_{sat} is the saturation intensity (7.56 mW/cm^2 for the ^{85}Rb cycling transition, averaging over all m_F levels) and Δ is the detuning of the laser (negative for red detuning). Expanding this expression with respect to v and evaluating near $v = 0$ one gets

$$F = -\alpha v = 4\hbar k^2 \frac{I}{I_{sat}} \frac{2\Delta/\Gamma}{\left(1 + 2I/I_{sat} + 4\Delta^2/\Gamma^2\right)^2} v, \tag{1.4}$$

where α is the friction coefficient in the description of a particle moving in a viscous medium. This force is obviously both velocity-dependent and intensity-dependent.

To trap atoms, rather than just to cool them, one needs a force that depends on position. One solution is to use an inhomogeneous magnetic field. There are various configurations of electromagnetic coils to create such a field. In our MOT apparatus two coils, symmetrically located on each side of the trapping region, have current flowing in opposite directions, creating a magnetic field gradient. The gradient in a MOT is much smaller in magnitude than the gradient in a magnetic trap. For instance, in the first realization of a MOT the gradient was about 5 G/cm (ref. [24]). Given this geometry one naturally assigns one axis of a 3-D coordinate system to the axis of the coils, usually the $\hat{z}$ axis (refer to Fig. 2.2). The laser beams are of appropriate circular polarizations to drive $\Delta m = \pm 1$ transitions with a preference depending on the Zeeman-shifted energy level of the atom, which in turn depends on its location (see Fig 1.3). As described above the interaction of light with the atom exerts a force on the atom, and in this case it is a position dependent force.

There are forces at work opposing the effects of the cooling and confining operation of the laser light and magnetic field. Among these pernicious factors are those which affect the density of the atomic cloud (the nonuniform absorption of light by atoms within the trap and the absorption of reradiated light by trapped atoms) and those which cause loss of atoms (collisions with untrapped atoms and collisions between trapped atoms). Some of these problems can be solved mechanically (improved vacuum) and optically (dark-spot MOTs). Others are more or less irremedial. The competition between the loading of the trap and the various loss mechanisms is manifested in this expression for the time derivative of the number of atoms N in the trap:

$$\dot{N} = L - \Gamma N - \beta n N, \tag{1.5}$$

where L is the rate at which atoms are loaded into the trap, Γ is the loss rate due to collisions with background atoms, β is the loss rate constant due to collisions

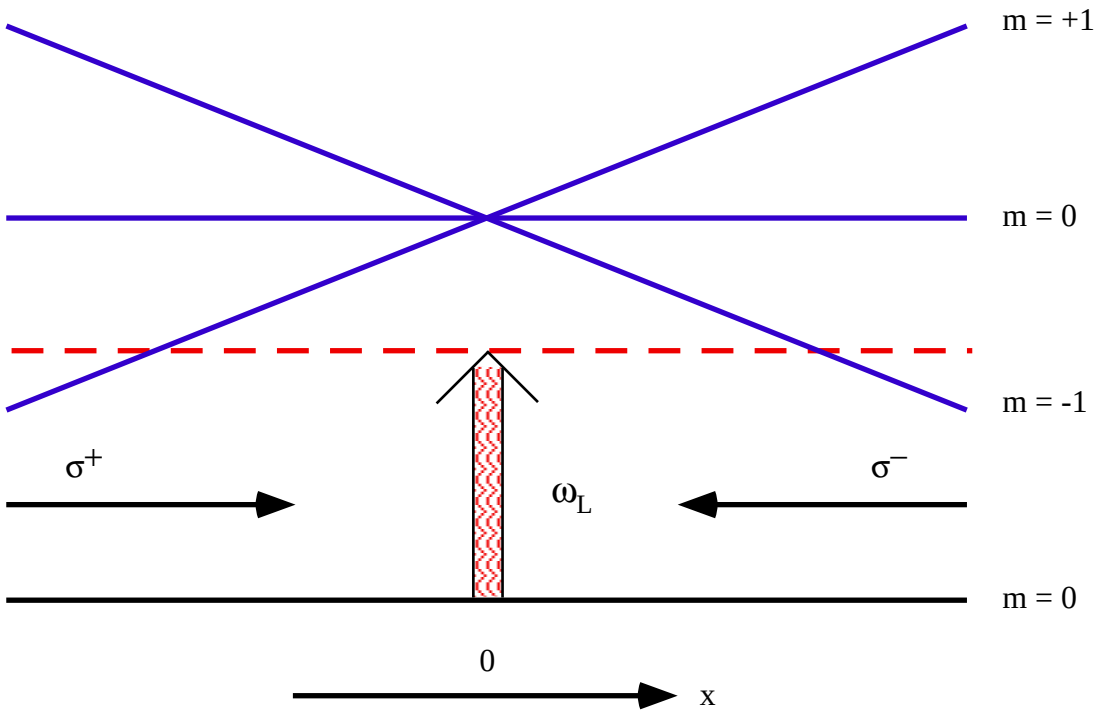

Fig. 1.3: Zeeman-shifted energy levels and $\sigma+/\sigma-$ polarized light. A magnetic field proportional to x is assumed. The laser is detuned to ω_L. An atom going in the $+x$ direction will come into resonance with $\sigma-$ polarized light and will undergo a $\Delta m = -1$ transition. Repeated scattering of such photons will impart momentum to drive the atom back towards $x = 0$.

between trapped atoms, and n is the number density. Under the conditions of the MOT used here the number density is a constant (refer to Chapter 5). In the photoionization and collision experiments additional loss mechanisms will be introduced, so this expression will take on a slightly different cast.

Chapter 2

Apparatus

Most of the apparatus required to perform this research is described in detail by Timothy Grove in [28]. A description of the main features will be given here. In addition changes to the apparatus, some additions of new equipment made since [28] and the very few omissions made by Grove will also be discussed.

This series of experiments was performed in a glass vapor cell MOT made by Alan Brown, the scientific glass-blower at the University of Connecticut (see Fig. 2.1). Its vacuum is maintained by a Perkin-Elmer 2 liter/second ion pump, which is kept at about 30° C to prevent rubidium deposition. The inhomogeneous magnetic field is created by two wire coils about seven centimeters in diameter and separated by about seven centimeters. The current in one coil runs in the direction opposite to that in the other coil, the antiHelmholtz (or "holtzHelm") configuration. These coils produce an axial magnetic field gradient of about 6.8 $\mathrm{G{\cdot}cm^{-1}{\cdot}A^{-1}}$. Most runs of these experiments were performed with a gradient of about 23 $\mathrm{G{\cdot}cm^{-1}}$. The trap laser is detuned about 10 MHz to the red of the D2 line (the $5S_{1/2}F = 3 \rightarrow 5P_{3/2}F' = 4$ transition) at 780 nm (refer to Fig 2.3). The intensity sum of all six beams is about 12 $\mathrm{mW/cm^2}$ with average beam diameters of 5 mm by 4 mm full width at half maximum. The repump beam is tuned near the D1 line ($5S_{1/2}F = 2 \rightarrow 5P_{1/2}F' = 3$) at 795 nm. In order to minimize the effects of the near-resonant trap laser, we switch its beam on and off, performing the experiments in the brief time there is no trap light impinging on the cloud of atoms.

This is accomplished by sending the beam through an IntraAction Corp. model AOM-402N acousto-optic modulator (AOM) driven by an IntraAction Corp model ME 40 MHz signal processor. All of these experiments were conducted with a trapping period of 20 μs. The trap duty cycle for the STIRAP experiment was 95% and for the photoionization and collision experiments 85%. The repump laser was switched only for the photoionization experiment, with the same 85% duty cycle as the trap laser. The repump was chopped for this experiment because of its possible contribution to trap loss by photoionization. The trapped-atom fluorescence is gathered by a 2.5 centimeter lens focussing the trap onto a fiber optic bundle which brings the light to a photomultiplier tube (PMT) with narrow-band (10 nm FWHM) filters. The filter at 780 nm effectively cuts out the repump light for all experiments. The PMT current goes to a SRS model SR570 Low-Noise Current Preamplifier, which replaced a Keithley model 428 current-to-voltage amplifier after the STIRAP experiment was completed. The output of the amplifiers is to either a Tektronix 2232 digtital storage oscilloscope and thence to a Mac II running LabVIEW or directly to LabVIEW. Descriptions of the various LabVIEW programs for each experiment are included as an appendix.

The trap is observed with an Elmo model SE360 charge coupled device (CCD) and a frame grabber (Image software package). The image scales at about 7 μm per pixel. From an image of the trap averaged over several (usually 16) frames one can estimate the trap's volume, assuming that the horizontal radius from the image is the same as the radius in the CCD's line of sight. The PMT was calibrated by measuring its response to a weak 780 nm beam of known power. We determined the number of atoms in the trap from the amplitude of the PMT signal, correcting for the excited state fraction and the geometry of the detector (see Appendix A). The number density of trapped atoms is a few $\times 10^{10}$ cm^{-3}. Other properties vary with the duty cycle: number 10^5 to 10^6, size (1/e radius)

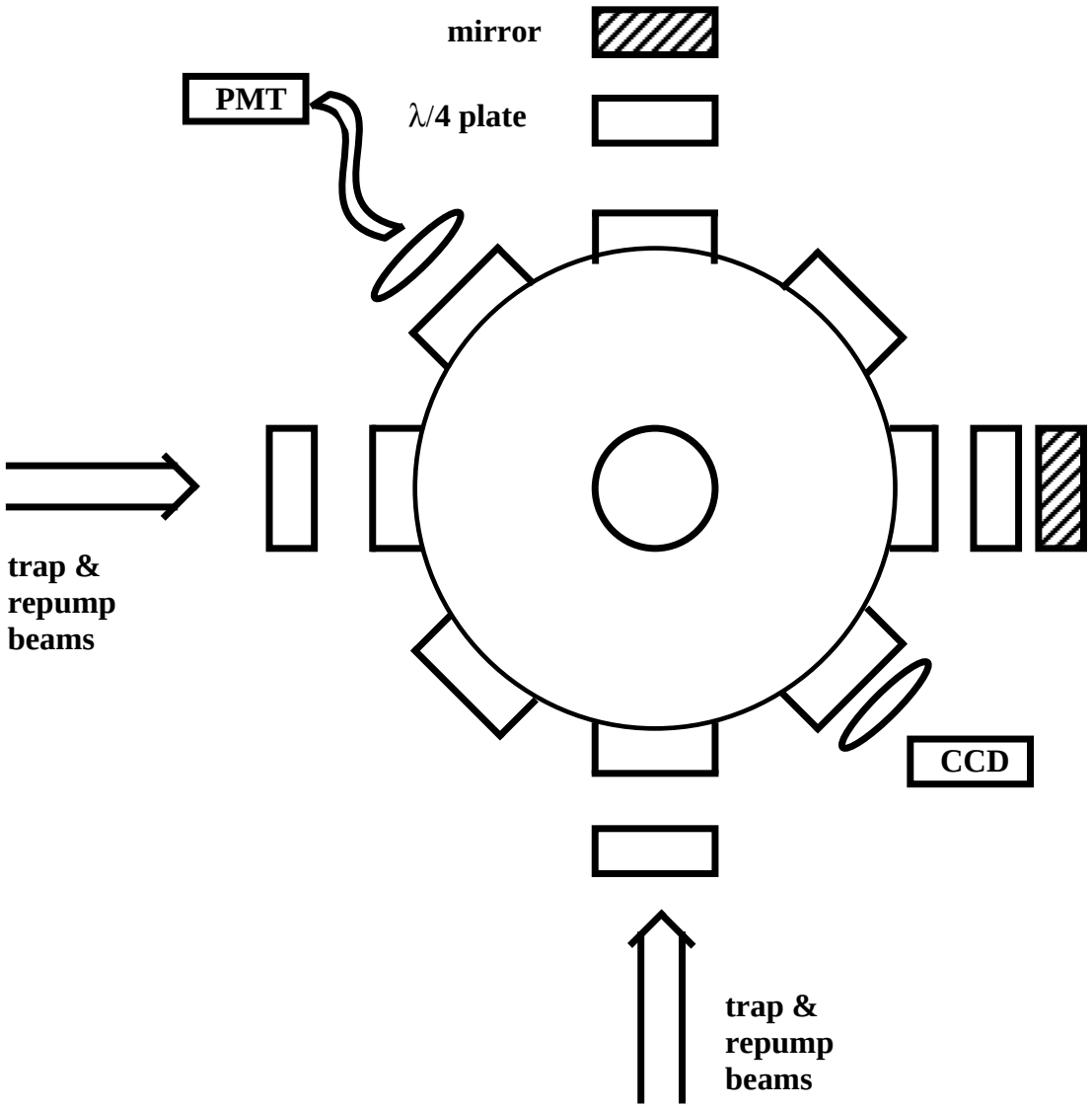

Fig. 2.1: Schematic of trap apparatus. The vertical trap and repump beams are not shown.

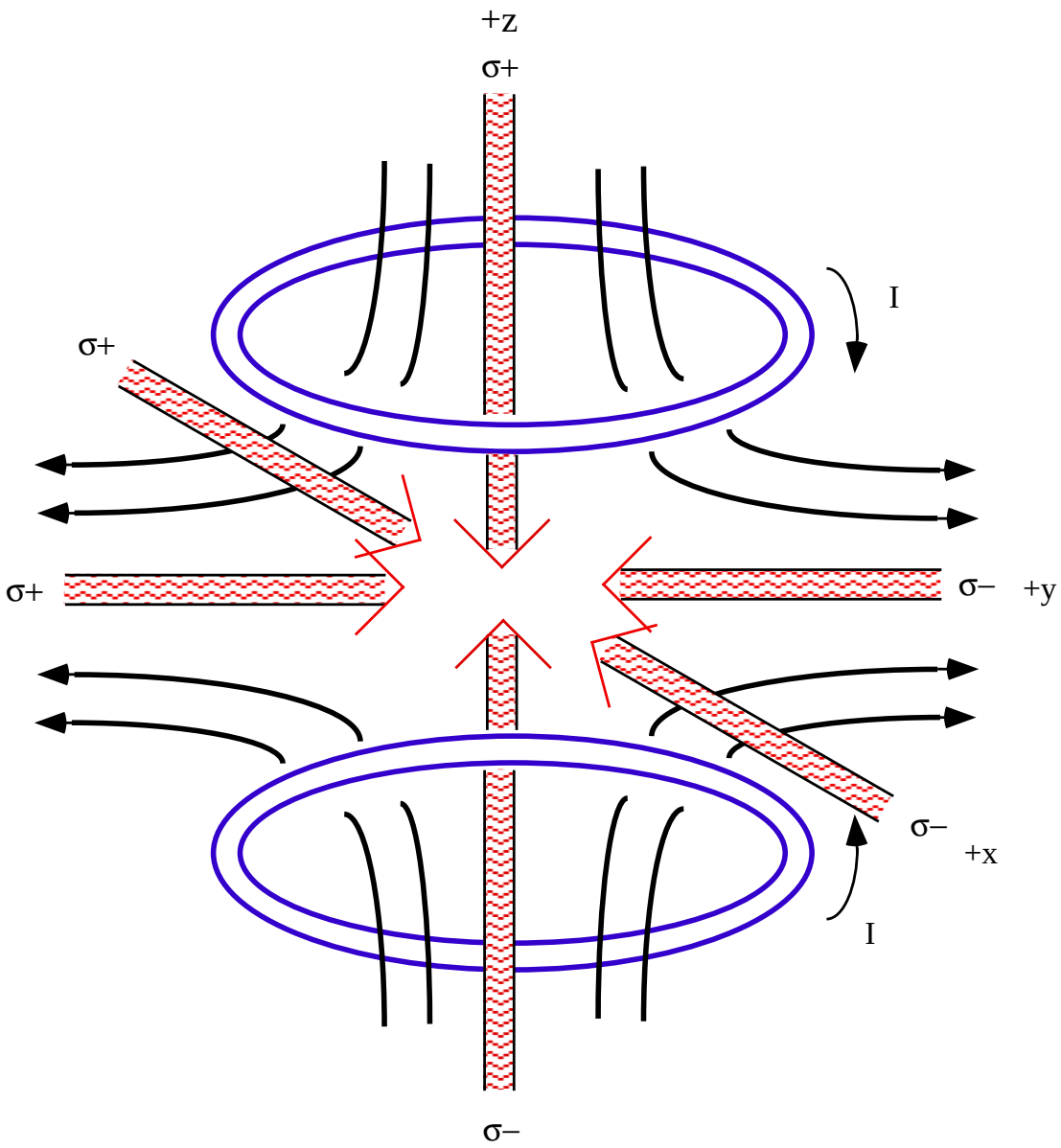

Fig. 2.2: AntiHelmholtz coils with circularly polarized light.

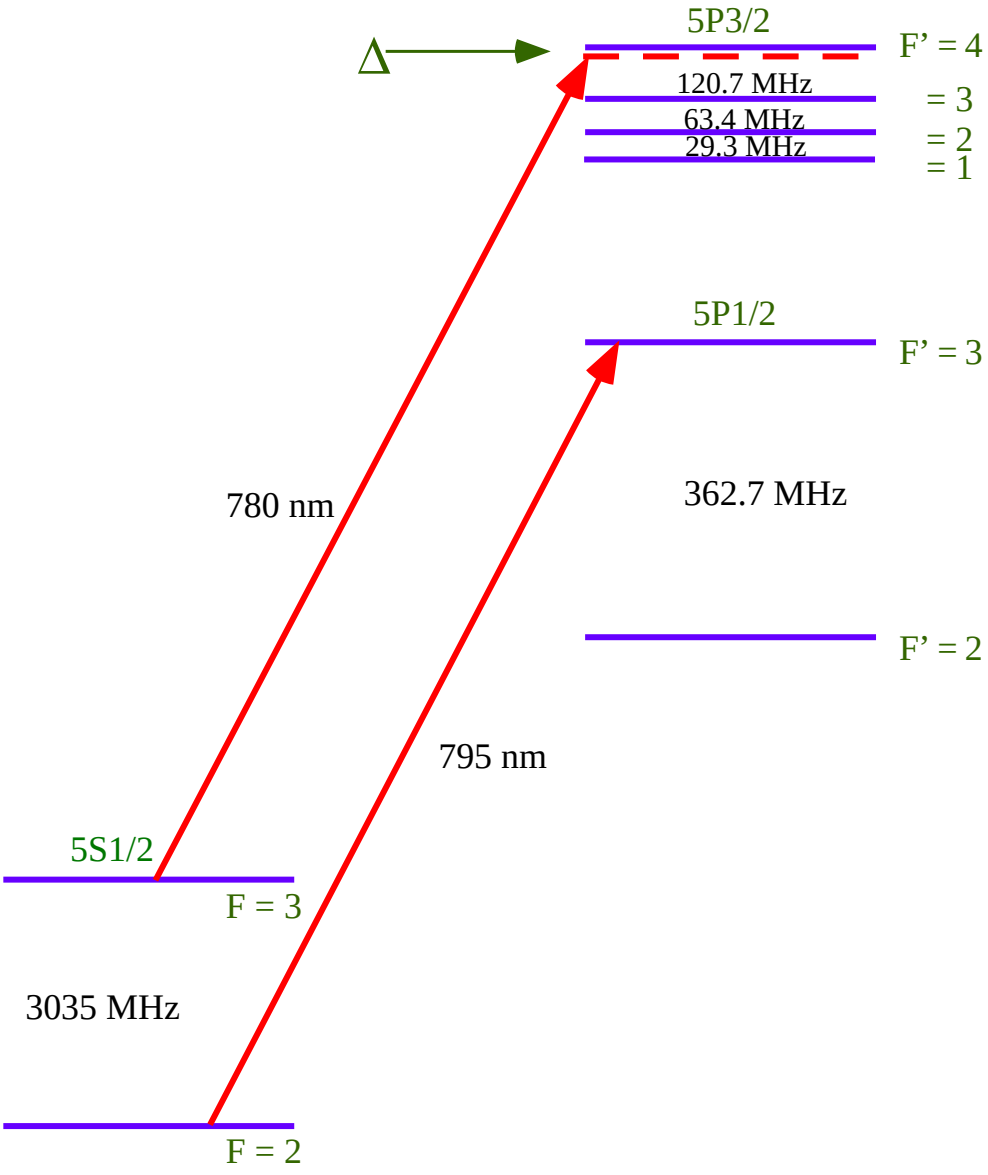

Fig. 2.3: Energy levels for a ^{85}Rb trap. The trap laser light at 780 nm is slightly red-detuned from the cycling transition. Off-resonant excitation into the $5P_{3/2}$ F' = 3 state allows optical pumping of population into the $5S_{1/2}$ F = 2 ground state. The light at 795 nm provides repumping out of that ground state.

100 μm to 220 μm, and loading time 0.5 s to 2.5 s.

Some of the laser diode current drivers and temperature controllers are commercially made. A list of these devices comprises products from Melles-Griot, WaveLength and Environmental Optical Sensors, Inc (EOSI, in the intervening years acquired by Newport). The Melles-Griot 56DLD403 and Wavelength Electronics LFI-3525 (temperature) and LFI-4502 (current) power and cool SDL 100 mW diodes, typically running below the maximum output power. The EOSI model LUC-2010-M is a complete system of driver, controller and extended cavity laser in the Littman-Metcalf configuration (see below). Other laser diodes are powered and their temperatures controlled by devices made in our laboratory, primarily by Grove with some assistance by Vicente Sanchez-Villicana and the present author. One current driver was modified by Wenko Süptitz and the present author (Fig. 2.4) to accomdate the negative polarity Mitsubishi 64110N (laser diode anode common with photodiode cathode) and 64114R (laser diode cathode common with photodiode anode) diodes.

The photodiode circuits used in the saturated absorption spectroscopy setups are in three cases the same as described in [28]. These circuits have the capability of subtracting the Doppler profile without the transition features from a profile with these features, leaving just the transitions sitting, ideally, on a flat line. This feature was not used in these experiments, as the present author finds it more convenient to locate the transitions within the Doppler profiles. The circuits remain unchanged, but the photodiode which gives the featureless profile is either covered with electrician's tape or is aligned so that no laser light enters it.

The circuit for the photodiode for the 776 nm master laser is not given in [28]; it is found in Fig. 2.5. Note that it has only one photodiode. The photodiode captures the light driving the 776 nm transition from $5P_{3/2}F' = 4 \rightarrow 5D_{5/2}F'' = 5$,

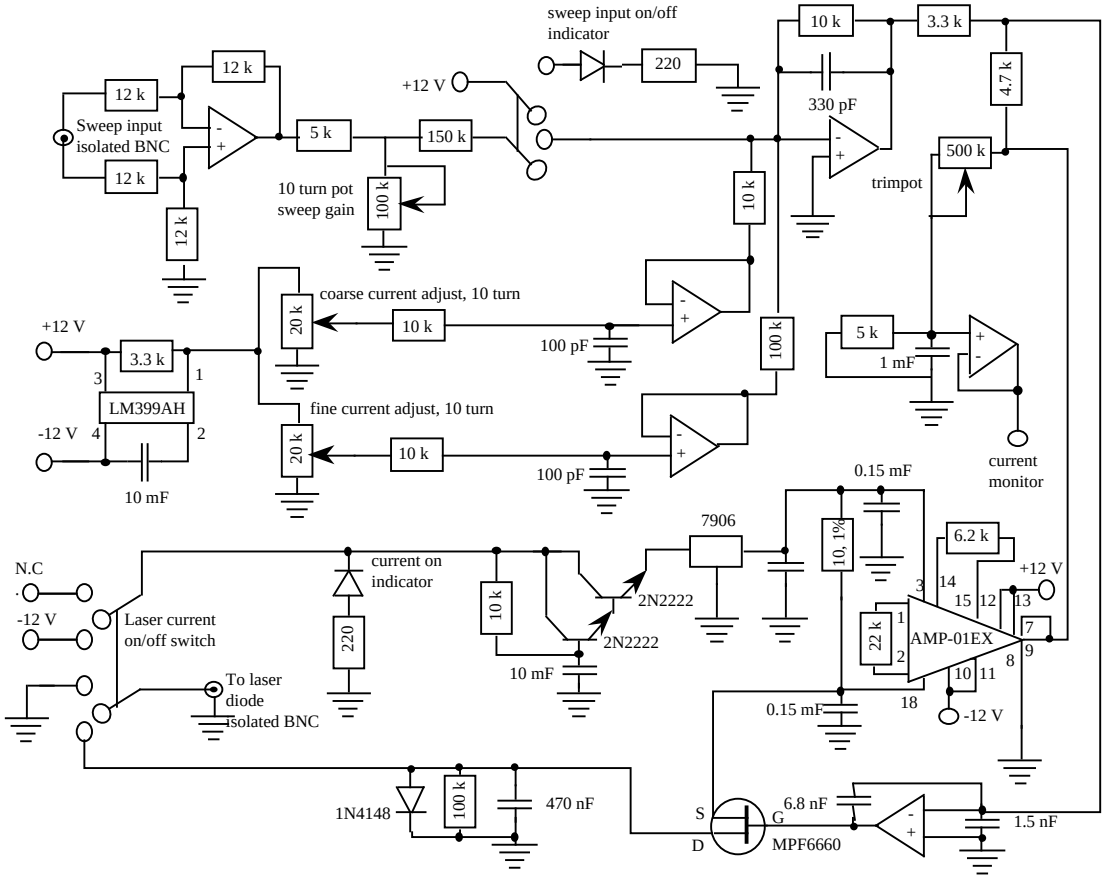

Fig. 2.4: Laser current driver with negative polarity.

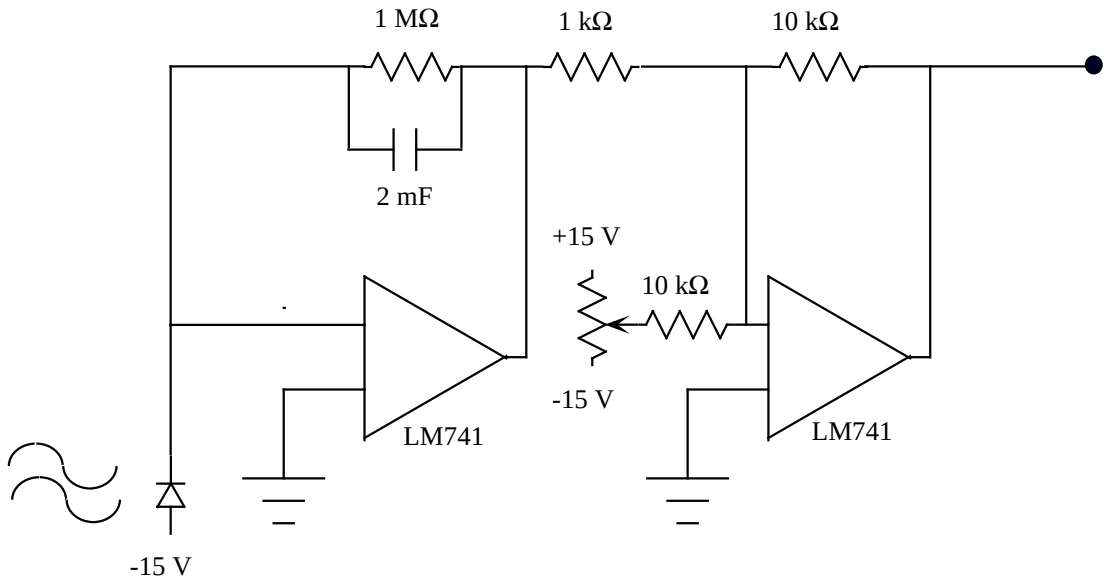

Fig. 2.5: Circuit for the photodiode not employing subtraction, used with the two-photon spectroscopy for the 776 nm laser.

the second step of a two-photon, two-color transition. The first step at 780 nm is $5S_{1/2}F = 3 \rightarrow 5P_{3/2}F' = 4$. The light driving this transition counterpropagates in a room-temperature rubidium cell (shielded by mu-metal shielding) with the 776 nm light driving the former transition. The 780 nm laser is frequency-stabilized by the standard saturated absorption setup described in the preceding paragraph. Light from the 776 nm laser then promotes the 5P atoms to the 5D state. The absorption of light by the atoms is reflected as a dip in the photodiode signal, and it is to this dip that the laser is locked. This arrangement of counterpropagating beams of nearly equal wavelength gives a nearly Doppler-free spectrum [29]; hence, a subtraction of a Doppler profile is impossible. The two-photodiode subtraction circuit could have provided a spectroscopic signal free from power fluctuations.

In addition to the diode lasers described above, the photoionization experiment employed a Coherent Innova 200 Kr-ion laser and a Continuum Minilite II neodimium doped yttrium aluminum garnet (Nd:YAG) laser. More details about these lasers and their role in the experiment will be given in Chapter 4.

Two circuits are new to the apparatus since [30]. The first of these is a driver for an acousto-optical modulator (AOM), found in Fig. 2.6 along with the separate circuit for voltage regulation. Wenko Süptitz brought the design from the laboratory of Theodor Hänsch. (As a matter of historical interest, this was our group's first use of printed circuit boards.) Two such drivers switch the Newport 80 MHz C8217A AOMs for the STIRAP beams. Since this time the design has been modified slightly and is now implemented in other apparatuses by putting each major component in its own aluminum box. These components are the MC1648 voltage controlled oscillator (VCO), the TTL-controlled YSWA switch and the CA2832C amplifier. The PAS 3 variable attenuator is currently not being used in those setups. The schematics for the current arrangement can be found in Stephen Gensemer's dissertation [31]. The AO drivers were triggered by multifarious devices in diverse configurations for the several experiments. Each configuration will be described within the chapter for the pertinent experiment.

During the course of the photoionization experiment the control of the current to the antiHelmholtz coils was given to the computer via a Magnecraft W76EURCPRX-16 relay. The circuit diagram is found in Fig. 2.7. This was done in order to get a zero level of the trap with which to compare the trap levels in the presence and absence of the photoionizing light. By turning off the magnetic field the trap is turned off, but the scattered light of all lasers was still present. The resultant level was averaged over six seconds and subtracted from the trap fluorescence level when the magnetic field was present (which was done

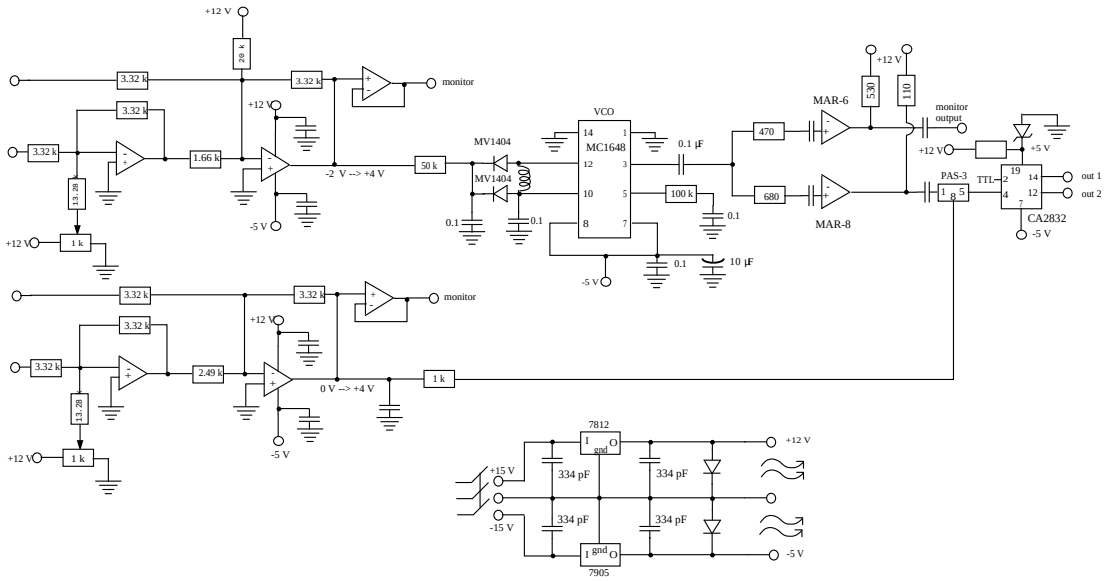

Fig. 2.6: Circuit for the 80 MHz tunable AOM driver. Recent versions of the circuit have the components split into three separate circuits.

in a loading curve, also of six seconds duration). The same practice was used in the collision experiment.

The mounts holding the laser diodes are of three types, two types of extended cavity laser (ECL) and one type essentially just holding the diode. The last named type is for the two high power SDL diodes providing the excitation to the 5D state. These diodes have built in Peltier coolers. The mounts have radiator "wings" as heat sinks to aid the coolers. Appended to each diode mount is a small aluminum piece to which is mounted the collimation lens holder. This holder has x-y controls which move the lens transversely to the direction of the laser beam in addition to the requisite collimation control in the z direction.

One of the two types of ECL is the Littman configuration (also known as the Littman-Metcalf configuration), described in [32,33]. The details for the particular

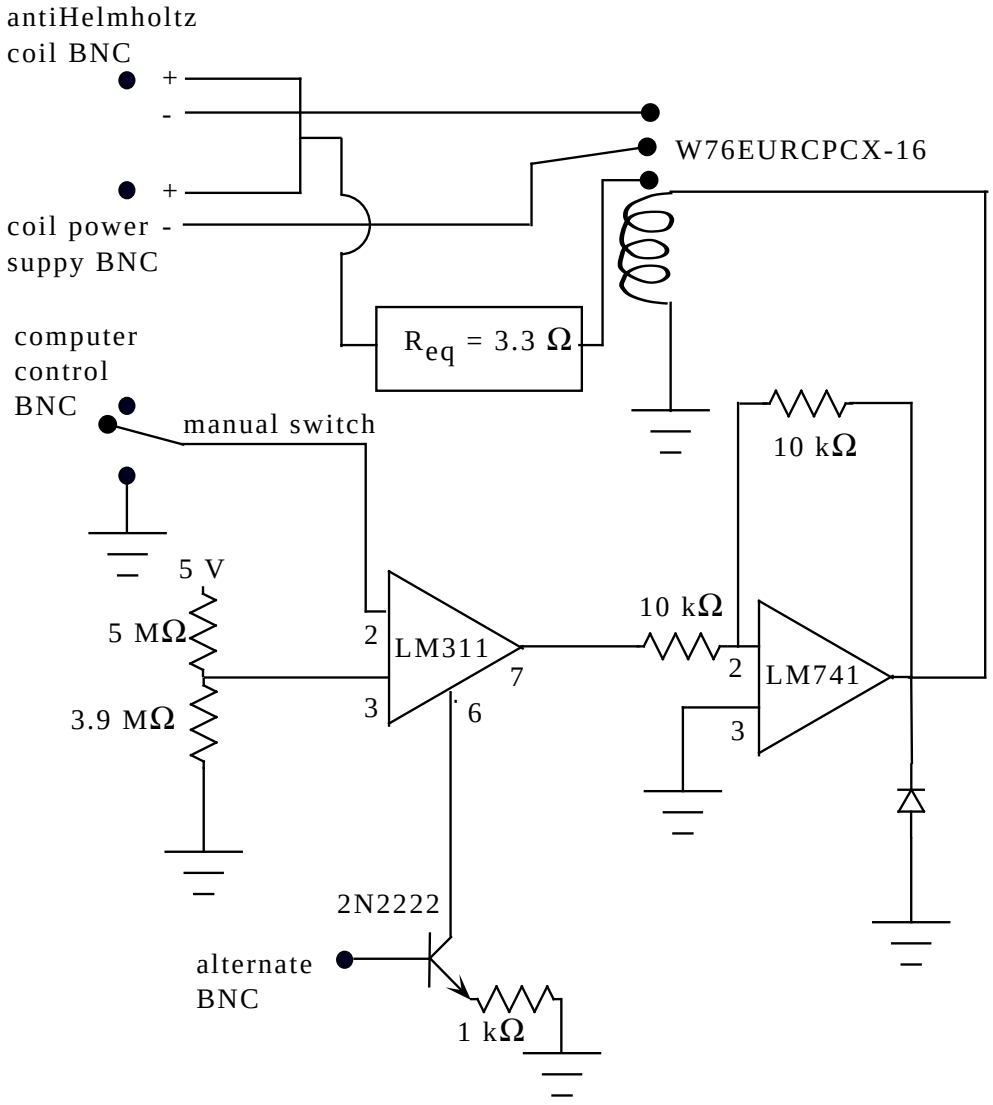

Fig. 2.7: Circuit for controlling the current to the antiHelmholtz coils. The manual switch is single pull, double throw. In the configuration as drawn, the antiHelmholtz coils receive current in two of the three switch settings. Were the power supply to be plugged into the alternate BNC, then the coils would receive current in only one setting.

mounts used in these experiments are given in [28]. In brief: the laser is held in an anodized aluminum tube (Optima CDL 3600 diode mounting kit) which also holds the collimating lens. The tube in turn is held in a small block (about 2 cm on each edge) of either aluminum or copper which is mounted on a Peltier cooler. This is attached to a large aluminum block serving as a heat sink (or source, as the case may be). Light from the diode strikes at grazing incidence a grating several centimeters away, so that most of the light is reflected in zeroth order on to the experiment. First order light from the grating hits a mirror and is reflected (via the grating) back to the diode. The mirror is attached to a piezo-electric transducer (PZT) which is controlled by a servo-loop circuit and a lock-in amplifier. The reflected light is used to force the diode to a particular wavelength and to narrow the diode's linewidth. This configuration is used in the EOSI laser and one other laser. The latter is run at 780 nm and serves two purposes. It provides the first step in the two-photon, two-color spectroscopy used to lock the EOSI laser at 776 nm, and it forces one of the high power diodes mentioned above to run at a particular wavelength by a technique known as injection locking. Hereafter this laser will be referred to as the 780 nm laser, although the trap laser also runs at 780 nm.

The other type of ECL is the Littrow configuration [34]. It is used for the trap laser, the repump laser and for some time for the laser run at 776 nm, which was replaced by the EOSI LUC-2010. The diode is held in a small aluminum block, and its collimating lens is mounted in a much smaller block a few millimeters away. Light from the diode strikes a grating located a few centimeters away. First order light from the grating provides feedback to the diode. The grating is on a horizontally moving flexure. The angle it makes with the diode light is coarsely set by rotating the entire grating mount, more finely set by an 80 pitch screw and more finely still by a PZT. (The servo-loop circuits for the PZTs in these

mounts are connected to a Thorlabs 3-axis piezo controller model MDT690.) This setup controls the horizontal dimension of the feedback light. The grating mount itself is placed on a vertically moving flexure controlled by an 18-32 bolt (more recent versions replace this with another 80 pitch screw). This controls the vertical dimension of the feedback. This flexure is attached to Peltier coolers, which are in turn mounted to the aluminum box enclosing the entire assembly. These mounts are the first in our laboratory employing this design. There have since been several changes in the design, recorded in [31]. The most recent developments in both the diode mount design and the concomitant electronics will be described in the forthcoming doctoral dissertation of Alexander Estrin at this university and the master's thesis of Mary Stone at the State University of New York, Stony Brook.

Light from each diode goes through a Faraday isolator, a device which protects the diode from reflected light. In this apparatus all the isolators were built on site and are of the following geometry. A terbium gallium garnet (TGG) crystal is located within a strong magnetic field created by two pairs of rare earth magnets so arranged that the field is constant near the center of the aluminum cylinder holding them. The crystal is placed in order that a linearly polarized beam is rotated 45°. Polarizing beam-splitting (PBS) cubes are placed on each end of the cylinder. The one nearest the diode is oriented so that most of the laser light passes into the cylinder. The one furthest from the diode is oriented so that most of the light passes out of the cylinder, i.e., at 45° to the first PBS cube. Let us consider the case of reflected light coming back with some arbitrary elliptical polarization. It encounters the second cube first, which linearly polarizes the reflected beam to the same angle at which the diode light left the isolator. The reflected light then traverses the TGG crystal, and its polarization vector is rotated yet another 45°, for a total of 90° since leaving the diode. This is orthogonal to the first PBS cube, and thus in the ideal case no reflected light comes back to the diode. In practice

one hopes to achieve an attenuation of 33 dB.

For the ECL diodes the light leaving the isolators hits a glass plate, picking off a small fraction of the light to be used in spectroscopy. In the case of the EOSI LUC-2010 this is the two-photon, two-color spectroscopy described in [30]. In brief: the light is sent through a rubidium cell with beam-splitting polarizing (PBS) cubes on either end and thence into a photodiode. Coming in orthogonally on the second PBS cube is light from the 780 nm laser. The two beams counter-propagate in the cell. The frequencies are two-photon, two-color resonant with the $5S_{1/2}F = 3 \rightarrow 5D_{5/2}F'' = 5$ transition. In the cases of the trap laser, the repump and the 780 nm laser it is saturated absorption spectroscopy, the particulars of which are given in [28]. The light is split into a weak probe beam and a stronger pump beam which counterpropagate in a cell. The probe beam continues into a photodiode. The probe beam is absorbed by atoms whose motion shifts the light onto resonance, giving what are known as 'Doppler profiles.' The pump beam depopulates groups of populations for which *it* is on resonance, resulting in hole burning. When both probe and pump beams are resonant with the same (v=0) velocity group, the absorption of the probe is saturated by the pump, yielding a Doppler-free absorption feature. The features produced by both the two-photon spectroscopy and the saturated absorption spectroscopy are used to lock the lasers on particular atomic transitions. For the trap and the 780 nm laser the rubidium cell is in a magnetic coil used to shift the $5S_{1/2}F = 3 \rightarrow 5P_{3/2}F' = 4$ transition a known amount [35]. This is usually about 10 MHz red detuning for the trap laser and about 127 MHz blue detuning for the 780 nm laser. During the photoionization experiment the saturated absorption for the repump laser also took place in a magnetic field. This was to counteract the frequency shift caused by the AOM used to turn the repump light on and off.

Chapter 3

Stimulated Raman Adiabatic Passage

3.1 Introduction and Theory

There is great desire on the part of atomic and molecular experimentalists to exercise control over the degrees of freedom of their samples, in particular to begin experiments with a well-defined state of the system. The parameters over which control is sought include velocity, energy and spin. This chapter discusses a technique for producing a sample of cold atoms in an excited state other than the upper level of a magneto-optical trap. This higher-excited ensemble of atoms will be the sample for further experimentation, such as measuring the photoionization cross section (see Chapter 4). In particular, our MOT provides an ensemble of cold rubidium atoms cycling between the 5S ground state and the 5P state. We want to excite a large fraction of these atoms to the 5D state (refer to Fig. 3.1). The problem of exciting atoms to well-defined high-lying levels received some attention during the 1970s and early 1980s. One research path started with Hioe and Eberly's 1981 paper [36] on describing the process in terms of an N-level coherence vector and its rotations. They continued this work with a paper concentrating on a three level system [37], which Hioe later developed [38] as "generalized adiabatic following," a subset of which came to be known later as "stimulated Raman adiabatic passage," or STIRAP. In this and subsequent papers (among which are [39], [40] and [41]) the situation of a three-level system was addressed, including the use of pulsed light to drive the transitions. Interestingly, even though the

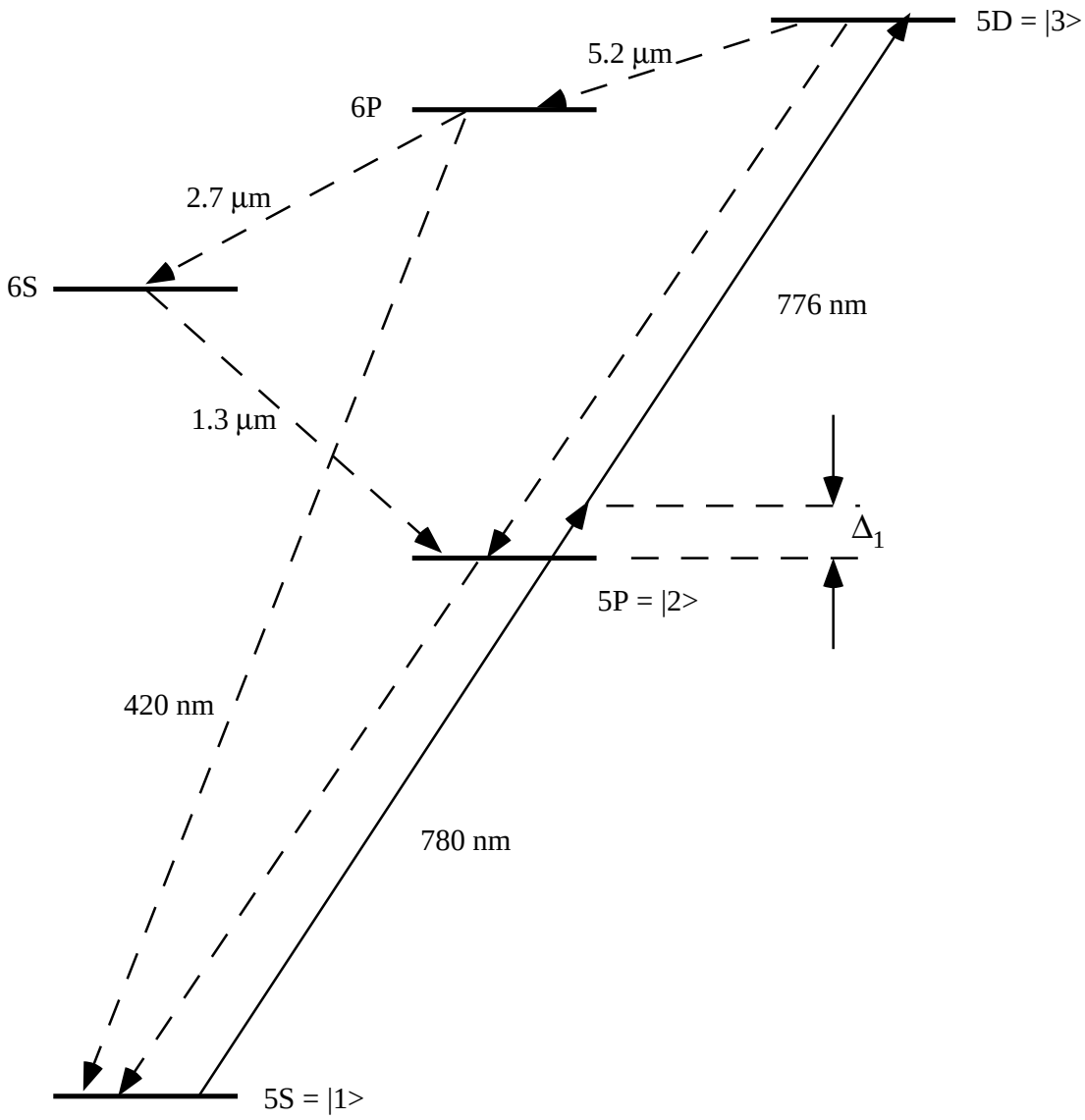

Fig. 3.1: Some energy levels of rubidium. The solid lines indicate the STIRAP laser wavelengths. The dotted lines indicate spontaneous emission from the various states. The detuning is indicated by Δ_1. Not all states or transitions are shown (the 4D is omitted), and the drawing is not to scale.

use of pulses separated by a delay is mentioned, these papers do not specifically address the situation of the pulses arriving in the counter-intuitive order, i.e., the pulse driving the upper transition coming before the pulse driving the lower one, which is the hallmark of the STIRAP process. Among the first experiments to use the counter-intuitive pulse order was the switching of population between molecular vibrational levels by Klass Bergmann and his colleagues in 1988 [42]. It was in 1990 in a subsequent paper by the same group that the acronym STIRAP was coined [4]. STIRAP experiments may be performed on an atomic (or molecular) beam, with "pulses" generated by the atoms passing through spatially separated laser beams perpendicular to the path of the atoms. Alternatively, the sample of atoms can be illuminated by spatially overlapped laser beams from pulsed lasers or from continuous wave (cw) laser beams going through acousto-optical modulators (AOMs). At least one group has used both beams and AOMs, the former on a Lambda-system in Ne* and the latter on Na in a ladder-system [43].

A simple analysis of the STIRAP process for a three level system is given [2]. The three levels have eigenvectors $|1\rangle$, $|2\rangle$ and $|3\rangle$ with a pump laser connecting the first two levels and a Stokes laser connecting the second two. The relevant quantity is the strength of the interaction, given by the Rabi rate:

$$\Omega_i = \frac{\mu_i E_i(t)}{\hbar} = \frac{\mu_i}{\hbar}\sqrt{\frac{2I_i}{\epsilon_0 c}}, \tag{3.1}$$

where μ_i is the dipole matrix element, $E_i(t)$ is the amplitude of the appropriate laser field and I_i its intensity. When using Eqn. 3.1 we calculate μ_i by assuming equal population in the seven m_F levels of the ^{85}Rb $5S_{1/2}(F = 3)$ ground state and calculating an average dipole moment (the square root of the sum of the squares of the individual dipole moments) with linearly-polarized light. We use the Einstein A coefficients from [44] for the $5P_{3/2} \rightarrow 5S_{1/2}$ transition and [45] for the $5D_{5/2} \rightarrow 5P_{3/2}$ transition. The square of the reduced dipole matrix element

is:

$$\mu_{ij}^2 = A_{ij}\frac{3\epsilon_0 hc^3}{2\omega_{ij}^3}. \tag{3.2}$$

Using the Clebsch-Gordan coefficients for the appropriate Δm = 0 transitions (excluding the $5P_{3/2}, F' = 4, m_F = \pm 4 \rightarrow 5D_{5/2}, F'' = 5, m_F = \pm 4$ transitions), we obtain $\mu_1 = 1.94\ ea_0$ and $\mu_3 = 0.540\ ea_0$. Under the rotating-wave approximation the Hamiltonian of the atom-field interaction is:

$$H = -\frac{\hbar}{2}\begin{bmatrix} 0 & \Omega_1(t) & 0 \\ \Omega_1(t) & 2\Delta_1 & \Omega_3(t) \\ 0 & \Omega_3(t) & 2(\Delta_1 \pm \Delta_3) \end{bmatrix}, \tag{3.3}$$

where Δ_i is the detuning of the lasers from the intermediate state. In the 3,3 element the plus sign is taken when the three level system is a ladder (or cascade) configuration; the minus is used in Lambda or Vee configurations. In the case of STIRAP the detunings are such that this term must be zero, that is, when two-photon resonance holds. (The details of obtaining this Hamiltonian are in Appendix B.) Of the three eigenvectors one is of particular interest:

$$|\lambda_0\rangle = \cos\Theta|1\rangle - \sin\Theta|3\rangle, \tag{3.4}$$

where

$$\Theta = \arctan\Omega_1/\Omega_3. \tag{3.5}$$

Note that this eigenvector does not involve the the intermediate state ($|2\rangle$) at all. As Θ starts at zero and goes to $\pi/2$, this eigenvector evolves from $|1\rangle$ to $|3\rangle$, providing efficient population transfer from initial to final states. In the case of Rb, populating this intermediate state ($|2\rangle = 5P_{3/2}$) would be especially deleterious, as its lifetime of 27 ns (which is comparable to the pulse widths) would lead to significant loss in transferring population to the $5D$ state, in addition to possible losses due to $5S - 5P$ collisions.

For the greatest efficiency in adiabatic passage, non-adiabatic coupling must be small. This obtains when the rate of change of Θ is small compared to the separation of the eigenvalues ([2,46]). Here the separation is :

$$\omega_{sep} \approx \left(\Delta_1 - \sqrt{\Delta_1^2 + \Omega_1^2 + \Omega_3^2}\right) \equiv \Omega_{eff}. \tag{3.6}$$

Differentiating Eqn. 3.5 with respect to time yields

$$\dot{\Theta} = \frac{\dot{\Omega}_1\Omega_3 - \dot{\Omega}_3\Omega_1}{\Omega_1^2 + \Omega_3^2}. \tag{3.7}$$

Thus the requirement for adiabaticity can be stated:

$$|\Omega_{eff}| \gg \left|\frac{\dot{\Omega}_1\Omega_3 - \dot{\Omega}_3\Omega_1}{\Omega_1^2 + \Omega_3^2}\right|. \tag{3.8}$$

Following Kuklinski *et al.* [2], we define laser pulses which are Gaussian in time, in units of the pulse duration T:

$$\Omega_i = \Omega_i^0 exp(-[\tau + \delta_i]^2), \tag{3.9}$$

where $\tau = t/T$ is the time and $\delta_i = \pm\Delta t/T$ is the time delay (the plus sign for Ω_3, the minus for Ω_1). One could as easily have defined the pulses using other functions, e.g., $\sin^4(\pi t/T)$, $0 < t < T$ as in [47]. When the delay is about the length of the pulse duration, the adiabaticity requirement can be expressed thus in terms of the duration:

$$|\Omega_{eff}T| \gg 1. \tag{3.10}$$

Since we want to use a finite pulse length, this inequality is met by ensuring Ω_{eff} is big enough. There is a limit, too, to how small the Rabi rates can be. Consider Eqn. 3.6. In the case of the Rabi rates tending to zero, Ω_{eff} can be expanded to be $0.5\times(\Omega_1^2+\Omega_3^2)/\Delta_1$. Using this in Ineq. 3.8, one sees that decreasing the Rabi rates works against adiabaticity on the left side of the inequality. By Eqn. 3.9 we see that the pulse delay δ cannot become large if Ineq. 3.10 is to be met. Furthermore, if the pulses are coincident or are in the intuitive order, Rabi oscillations result

and the system is sensitive to laser parameters. In the counterintuitive order and with Ineq. 3.10 met, the system is relatively insensitive to these parameters. (See Fig. 3.2, which appeared in Ref. [48].)

3.2 Set-up and Techniques

Atoms in the ^{85}Rb $5S_{1/2}F = 3$ ground state are transferred to the $5D_{5/2}F'' = 5$ state via a two-photon, two-color stimulated Raman adiabatic passage (STIRAP) process [4]. The lasers required to perform this are described in Chapter 2. The salient features are briefly recapitulated here. Two high-power continuous wave (cw) lasers at 780 nm and 776 nm drive the $5S \rightarrow 5P$ and $5P \rightarrow 5D$ transitions, respectively, providing up to 10 W/cm^2 in beams of 600 μm diameter (FWHM), more than twice the diameter of a typical MOT cloud. This beam size is used in an attempt to ensure that the atoms in the MOT experience a near-uniform intensity. The 780 nm high-power laser is injection-locked by a low-power, linewidth-narrowed external cavity laser in the Littman-Metcalf configuration locked to a saturation absorption feature in a magnetic field. The low-power laser is locked about 127 MHz to the blue of the $5S_{1/2}F = 3 \rightarrow 5P_{3/2}F' = 4$ transition. In this experiment the 776 nm high-power laser is locked by a low-power laser in the Littrow configuration, itself locked 127 MHz to the red of the $5P_{3/2}F' = 4 \rightarrow 5D_{5/2}F'' = 5$ transition by two-photon spectroscopy [29]. The light from the high-power lasers passes through acousto-optic modulators (AOMs) creating pulses of about 35 ns FWHM as measured by a fast photodiode (rise time $\sim$ 1 ns). The AOMs shift the frequency of the pulses 80 MHz closer to their respective atomic transitions, so that the resultant detuning is about $\Delta_{780} = +47$ MHz and $\Delta_{776} = -47$ MHz, and thus the two photon $5S_{1/2} \rightarrow 5D_{5/2}$ resonance is maintained. This detuning is present in order to minimize the effect on the trap of the approximately 0.2% leakage of light through the 780 nm beam's AOM. In order to align these beams on the trap the typical practice is to block the 776 beam and move the 780 beam

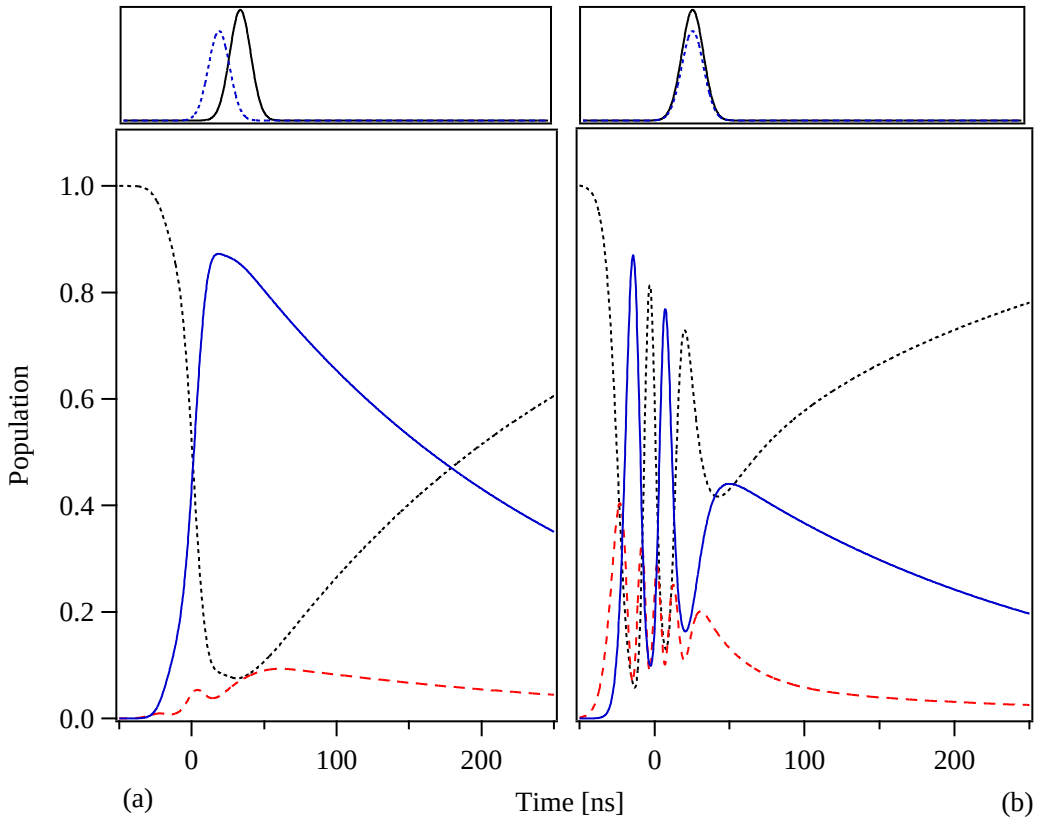

Fig. 3.2: Time evolution of the atomic populations from simulations. The Rabi rates are $\Omega_1 = \Omega_3 = 6\Gamma$. The one-photon detuning is 7.5 Γ. The pulse widths are 33 ns. Inset (a) shows the evolution when the pulses are in the counter-intuitive order by 20 ns. Inset (b) is for coincident pulses. The solid line indicates the 5D state, the dashed the 5P and the dotted the 5S. The upper frames indicate the pulse timings: the solid line is Ω_1, the dotted line is Ω_3.

around until the pushing effect on the trap is greatest. Sometimes this is aided by increasing the pulse duration or by bringing the wavelength closer to resonance. Then the 776 beam is aligned by eye onto the 780 beam.

The experiment is conducted by varying the pulse delay between the 776 nm pulse and the 780 nm pulse for fixed intensities of both beams. The intensity of one pulse is varied while the other remains at its peak value; then the roles are reversed. As is described in some detail below, the delay is controlled by a ramp voltage from a function generator. The intensities are attenuated by neutral density filters or by a combination of halfwave plate and polarizer.

As will be demonstrated below, the efficiency of population transfer into the 5D state is higher when the pulses arrive in the counterintuitive order, i.e., the pulse driving the $5P \rightarrow 5D$ transition (776 nm) starts before the $5S \rightarrow 5P$ (780 nm) pulse. More correctly, the 776 nm light must be on before the 780 nm light turns on; it must turn off before the 780 nm light turns off; and the the two beams must temporally overlap to some degree. For two Gaussian or near-Gaussian pulses of equal duration the temporal separation for best STIRAP efficiency is approximately the half width at half maximum of the pulse duration. These pulses come within the 1 μs window described above in Chapter 2 (also refer to Fig. 3.3). The repump laser (on the D1 line at 795 nm) and the magnetic field are on constantly.

About 11% of the time a 5D atom will decay along the $5D \rightarrow 6P \rightarrow 5S$ path, emitting a photon at 420 nm during the second step. This fluorescence and the 780 nm trap fluorescence are the relevant signals, acquired by a photo-multiplier tube with narrowband (10 nm FWHM) filters appropriate to each fluorescence wavelength. The data are stored in a digital storage oscilloscope. When three scans (with respect to delay) of a particular color have been stored, they are

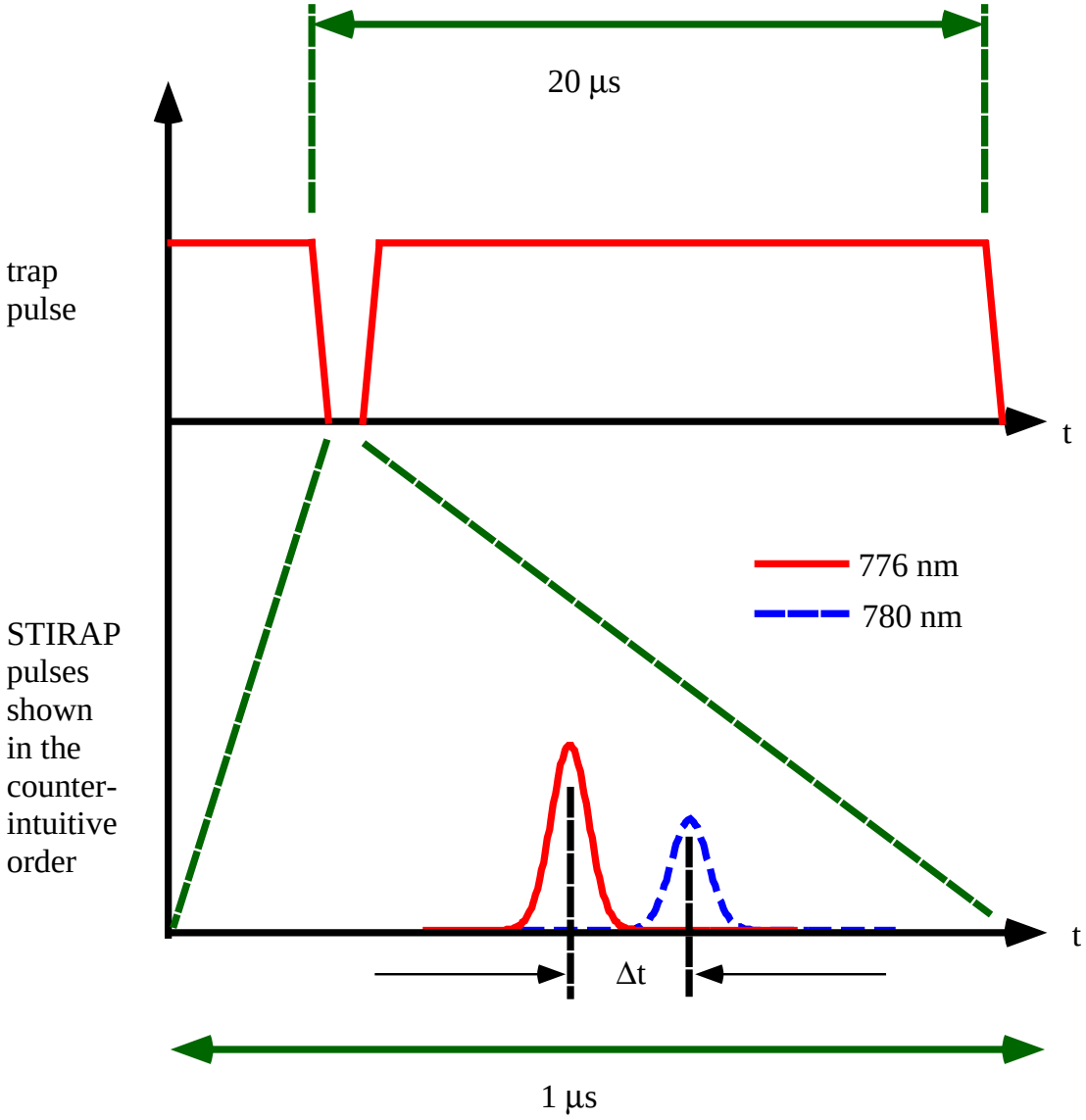

Fig. 3.3: The timing scheme for the STIRAP experiment. The repump beam is on continuously. The downtime for the trap beam is typically 1 μs. The 776 nm STIRAP pulse is usually centered in the trap downtime. Here Δt indicates the delay between the STIRAP pulses.

transferred to the oscilloscope memory. Later, scans of the other color are taken and likewise saved. When all of the oscilloscope's memories are filled, they are downloaded to the computer via a GPIB connection controlled by LabVIEW. Along with the fluorescence signal the ramp voltage controlling the delay between the STIRAP pulses is also stored. The data are later analyzed using Igor. The macros used to analyze the data are tersely described in an appendix (Appendix C).

This analysis is not particularly straightforward. The single PMT cannot capture both the 780 nm and 420 nm signals at the same time, which is what the best of all possible worlds would have provided. Thus some procedure has to be devised to match the two signals as a function of STIRAP pulse delay. This is accomplished by acquiring the two signals separately but under similar conditions (i.e., without letting much time elapse between measurements) and then for the two signals matching the ramp voltages (which control the delay between pulses). The ramp voltage itself presents a problem: pulse delay is not a linear function of the ramp voltage (see Fig. 3.5, for instance). We record the voltages required for particular pulse delays, usually five or six measurements within the range of the ramp. These are then fit to a polynomial function which eventually yields the pulse delay as a function of time. This function is then incorporated into the Igor macros used in analysis. These macros automate the matching of the ramp voltages, adjust the 780 nm and 420 nm signals to the pulse delay, smooth the 780 nm signal, normalize it to its peak value, and correct the 420 nm signal for the changing number of atoms in the trap. Examine the next several figures. In Fig. 3.4 the raw 780 nm fluorescence data and the ramp voltage are displayed. Fig. 3.5 displays the trap fluorescence smoothed and normalized. As the STIRAP pulses overlap in time, there is a loss of atoms from the trap and hence fewer atoms to participate in STIRAP in the next excitation. Were this loss not taken into

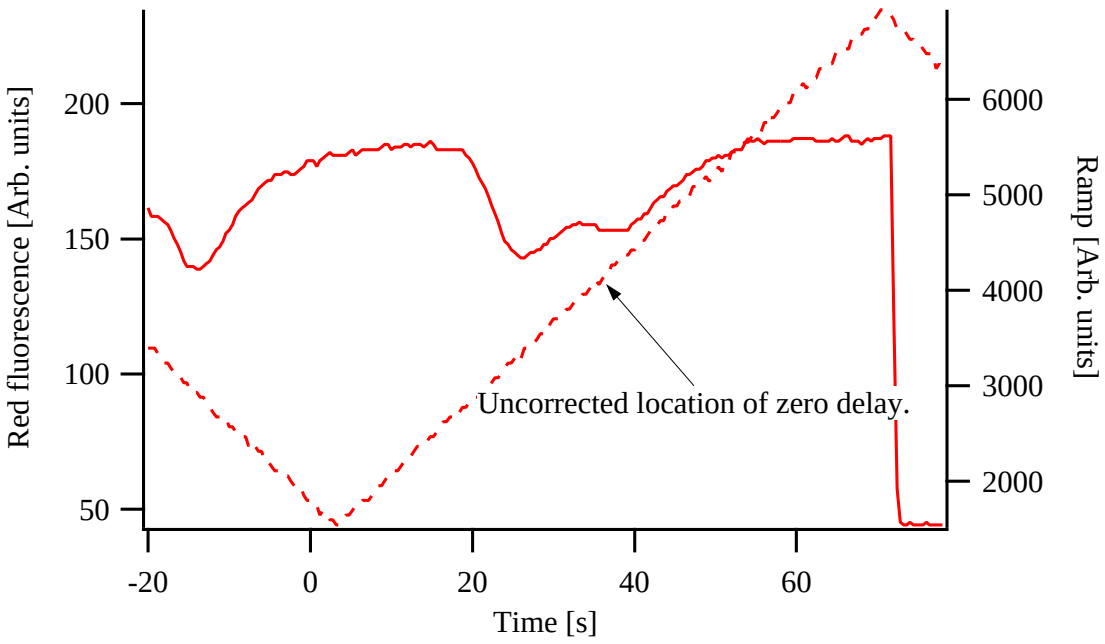

Fig. 3.4: Raw 780 nm fluorescence.

account, this STIRAP process would appear to be less efficient than it really is. Compare Fig. 3.6, which shows the raw 420 nm signal, to Fig. 3.7, which shows the 420 nm signal corrected by dividing the 420 nm signal by the normalized 780 nm signal.

This experiment is performed over nine orders of magnitude in time. The shortest scale is tens of nanoseconds; the longest is tens of seconds. For subsequent experiments (cf. Chapters 4 and 5), the fast pulses are generated by an SRS DG535 which in turn triggers (or at times is triggered by) a Hewlett Packard 8082A pulse generator and a Wavetek Model 801 pulse generator (borrowed from George Gibson or from Winthrop Smith). However, for the present experiment the timing is controlled by a complicated arrangement of several devices. Three pulses are necessary, for the trap, the 780 nm pulse and the 776 nm pulse (the repump laser is on all the time). To relate all the details would be needlessly

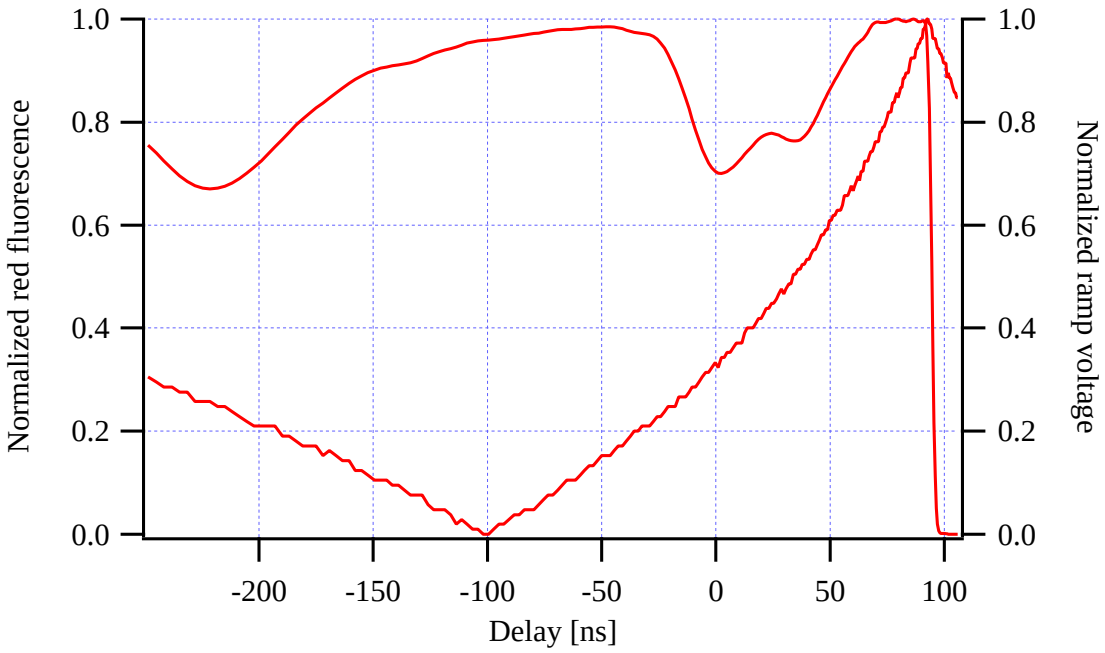

Fig. 3.5: Averaged and normalized 780 nm fluorescence. Also note the non-linear character of the ramp voltage.

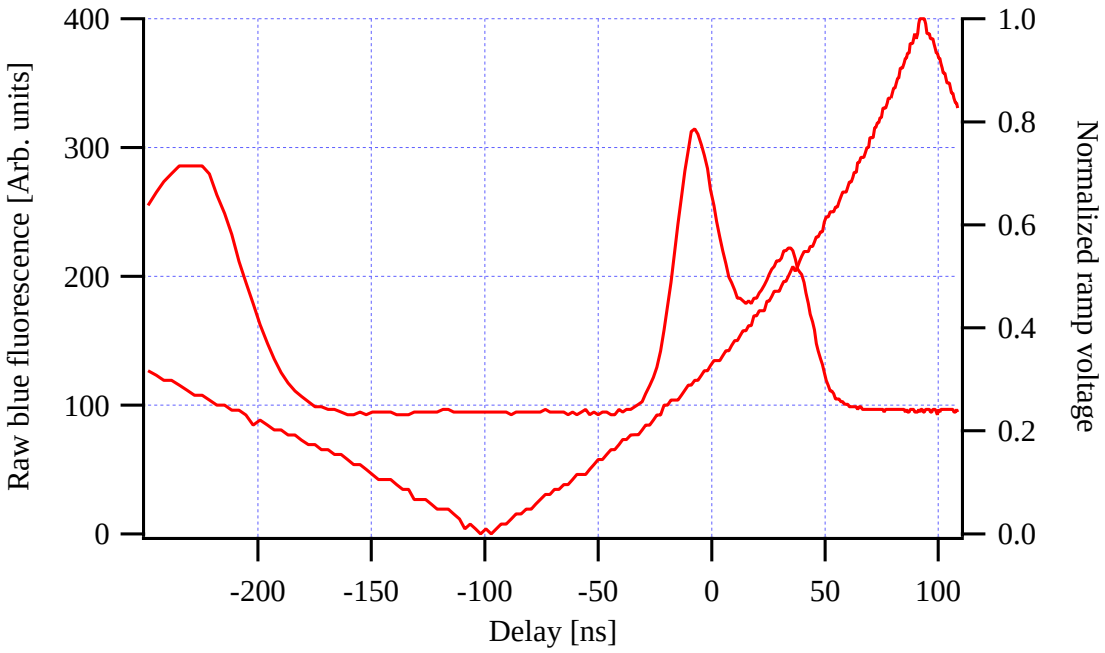

Fig. 3.6: Raw 420 nm fluorescence.

stultifying, so only a gross description will be given. A BNC connector is wired to the delay control of the HP 8082A Pulse Generator which controls the 780 nm pulse. A Leader LFG 1300S Function Generator is connected to this BNC, adding a ramp voltage to the delay set manually on the 8082A. This ramp sweeps the 780 pulse from 100 ns or so before the 776 pulse to an equal interval after it. The 8082A triggers a Tektronix PG508 pulse generator, which controls the 776 pulse. This pulse is stationary in time with respect to the trap pulse. The PG508 triggers a Tektronix FG501A function generator which in turn triggers a Tektronix PG501 pulse generator. The latter controls the trap laser AOM; the former controls where the downtime of the AOM comes with respect to the 776 pulse. In order to set the range of the delay of the 780 pulse so that it symmetrically encompasses the 776 pulse with the same amount of delay on either side, the 780 is swept fast enough (up to 100 Hz) so that the range can be easily seen on an oscilloscope.

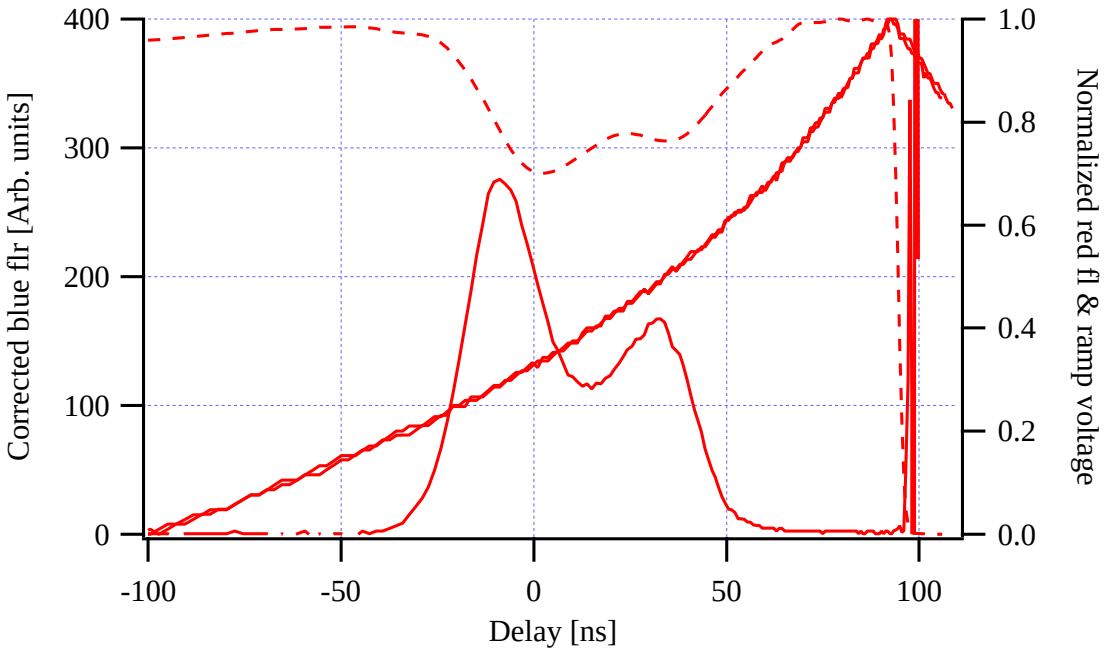

Fig. 3.7: Corrected 420 nm fluorescence with normalized 780 nm fluorescence and matched ramp voltages.

The center and size of the range are set by the manual delay on the 8082A and the amplitude on the function generator. Once set, the sweep is slowed down so that it takes from 30 to 50 seconds for the 780 pulse to cover the range (i.e., for the ramp waveform a period of about 60 to 100 seconds). This is necessary to ensure that changes to the MOT are slow compared to its typical loading time of $\sim$1 second.

It is essential that the STIRAP pulses maintain two-photon resonance and that the lasers producing the beams be single-mode. We monitor these conditions by sending the zeroth order AOM beams of the high-power lasers copropagating through a rubidium cell and into an optical spectrum analyzer (Burleigh RC46). These beams are so intense that in a dimly-lit laboratory one can see the 420 nm fluorescence in the cell. This provides the experimenter with a quick qualitative check that the lasers are on the two-photon $5S \rightarrow 5D$ resonance. The spectrum analyzer serves two purposes. The first is to test whether the high-power laser is injection-locked. The usual method is to sweep each low-power master laser and determine that it is single mode over at least 500 MHz. (The layout of the beams and the position of the spectrum analyzer allow it to test each master independently and then both slaves together, simply by rotating the analyzer's detector head. Refer to Fig. 3.8.) One then analyzes the slaves, ensuring that each follows its master and is likewise single mode over at least 500 MHz. Alternatively, one could sweep the high-power lasers by applying a sinusoidal voltage to vary the diode current and hence its wavelength. One then injects this laser with light from a low-power laser locked to a spectroscopic feature. If the high-power diode is locked, the master will prevent it from sweeping. While it does not require a lot of optical power to lock a laser, there are some critical restrictions: a slave will lock more easily if its free-running wavelength is within a few nm of the desired wavelength (this can be helped by the proper combination of diode current and

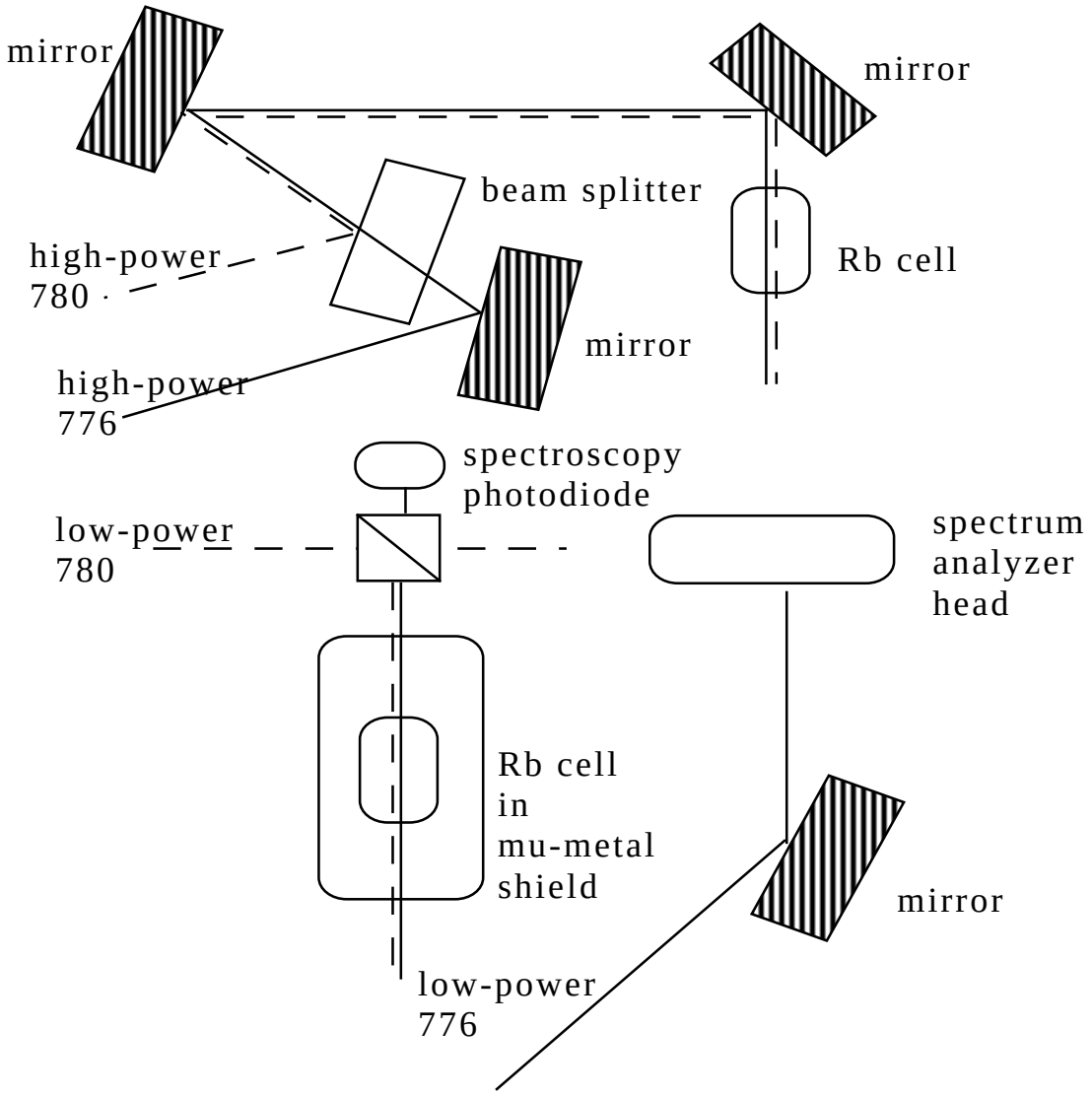

Fig. 3.8: The layout of the optical spectrum analyzer and the two-photon, two-color spectroscopy used during the STIRAP and subsequent experiments. Where lines run alongside one another, the reader is to understand that the laser beams overlap. The high-power beams are the zero-order beams from their respective AOMs.

temperature); the polarization of the two beams must be close (certainly within 30°; the closer, the better); and most important is the overlap: the master beam must illuminate the emitter of the high-power diode. In this setup additional optical isolators are required to protect the low-power diodes from the high-power ones. The 780 nm injection path had one additional 30 dB isolator, the 776 path two. The high-power diodes had no isolators of their own. During this experiment this did not create a problem, but in subsequent experiments the peculiarities of beam alignment caused some feedback for the 776 diode. This will be discussed in short at the end of this chapter.

The second principal purpose for the spectrum analyzer is to provide a continual check on the single mode character of the high-power diodes. (Note that by itself the analyzer does not indicate if the lasers are on the correct wavelength.) Multimode behavior is usually evidenced by the appearance of sidebands in the spectrum but also by the sudden increase in linewidth of the high-power lasers. It is usually the case that, after initially locking the high-power lasers, any departure from single mode behavior is due to the low-power lasers. Thus when it appears that a slave is no longer single mode, one should examine the condition of the corresponding master before considering the high-power lasers.

3.3 Results

The experiment was run as described above. In addition to changing the delay between the STIRAP pulses by a ramp voltage, we also changed the Rabi rates by attenuating the intensity of the STIRAP beams. Initially this was accomplished with neutral density filters in the paths of the high power beams. It was superceded by a method which sends the already linearly-polarized beams of the high power lasers through half-wave plates and a polarizing, beam-splitting cube (PBS). The wave plate rotates the polarization vector of the beam, and the PBS

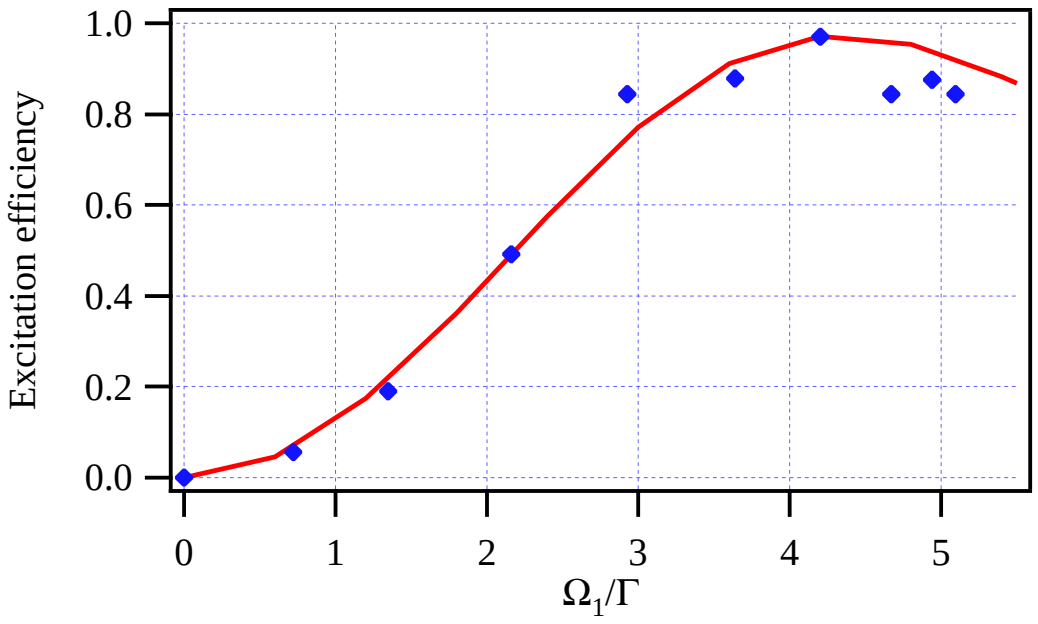

Fig. 3.9: STIRAP efficiency at a counterintuitive delay of -20 ns, as a function of the 780 beam Rabi rate. The 776 Rabi rate is fixed at its highest value, corresponding to $I_3 = 9.3$ W/cm^2. The solid line is a fit described in the text.

cube allows only that portion to pass which is correctly aligned. Thus the orientation of the wave plate gives a continuously variable control on laser intensity (with minimal deviation of the beam). The intensity of one beam is held at its highest level while the intensity of the other beam is varied. Then the roles are reversed. Typical raw and processed data are presented in Figs. 3.4, 3.5, 3.6 and 3.7. The estimated STIRAP efficiency while varying each intensity at a fixed delay is shown in Figs. 3.9 and 3.10. Results for varying Rabi rates while changing the pulse delay are given in Figs. 3.11 and 3.12. These figures include simulations using a "software atom" program written by Juha Javanainen [53,54], which employs the semi-classical theory of atom-field interactions. Semi-classical here means that the light field is treated classically, while the atoms are treated quantum mechanically.

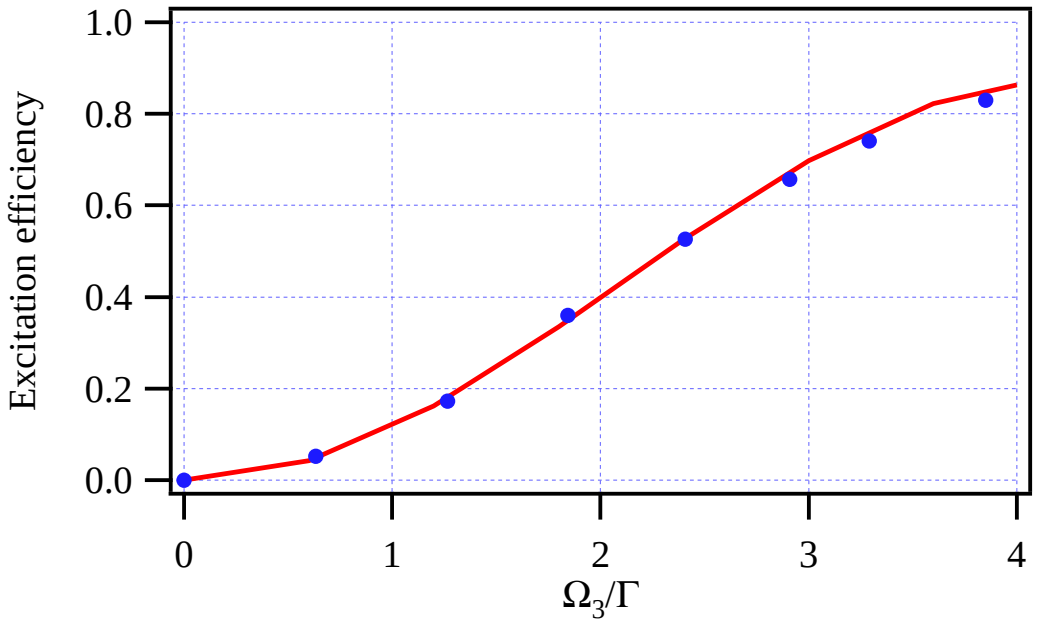

Fig. 3.10: STIRAP efficiency at a fixed delay of -20 ns, as a function of the 776 beam Rabi rate. The 780 Rabi rate is fixed at its highest value, corresponding to $I_1 = 7.9$ W/cm^2. The solid line is a fit described in the text.

The simulations usually treat the STIRAP process as a three-level system (5S, 5P and 5D). An example of the driver program (which is modified by the end user) is given in Appendix B.4. The experiment was conducted usually with lin$\|$lin polarization for the STIRAP beams. Other polarization combinations were used, without noticeably different results.

Figs. 3.7, 3.11 and 3.12 clearly indicate that the 420 nm fluorescence is greatest when the pulses arrive in the counter-intuitive order. This light comes from the $6P \rightarrow 5S$ transition, and in this experiment the 6P state can be populated only by decay from the 5D. Hence, the 420 nm fluorescence is a signal that the 5D state is being populated. Also note the trap loss, as recorded by the normalized 780 nm fluorescence. At the time of the experiment we did not know the cause of this, considering photoionization or collisions as possible causes. Since Ref. [48] we have measured (Ref. [55]) the 5D photoionization cross-section at 788 nm (10.9 Mb), only 9% larger than the value used to approximate the cross-sections at 780 and 776 nm in the simulations cited in Ref. [48]. According to the reruns of the simulations, most of the trap loss is not due to photoionization by the STIRAP pulses. Taking typical pulse widths and delays and using high Rabi rates ($\Omega_1 = 30\Gamma$ and $\Omega_3 = 13\Gamma$) corresponding approximately to the maximum intensities used, we obtain a photoionization probability per pulse pair of about 2×10^{-6}. Refer to Fig. 3.13. Since the STIRAP excitation is repeated at 50 kHz, this yields a time-averaged loss rate of $\sim 0.1\ \mathrm{s}^{-1}$. This is about 12% of the inferred loss rate due to the STIRAP excitation. As will be seen in the final chapter, it is difficult to assign the loss to collisions, as well.

Figs. 3.11 and 3.12 show results for various Rabi rates from experiment and simulation. In these and in Figs. 3.9, 3.10 and 3.14 the pulse width is ~ 33 ns and the detuning is 7.5 Γ. The highest intensities in these graphs are $I_1 = 7.9\ \mathrm{W/cm^2}$

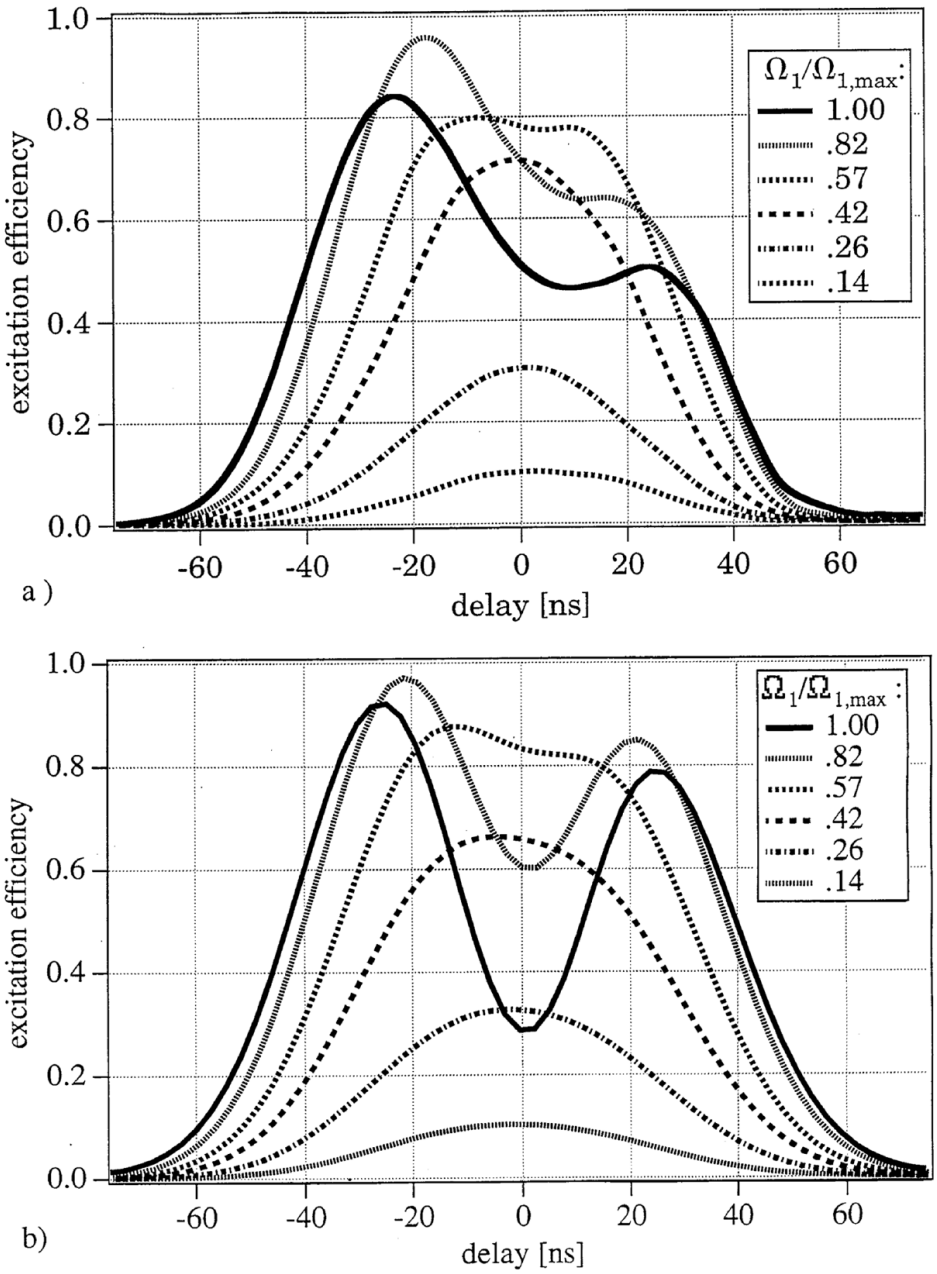

Fig. 3.11: Excitation efficiency for various 780 nm Rabi rates with the 776 nm Rabi rate held constant at its highest value. (a) Experimental, (b) from simulations.

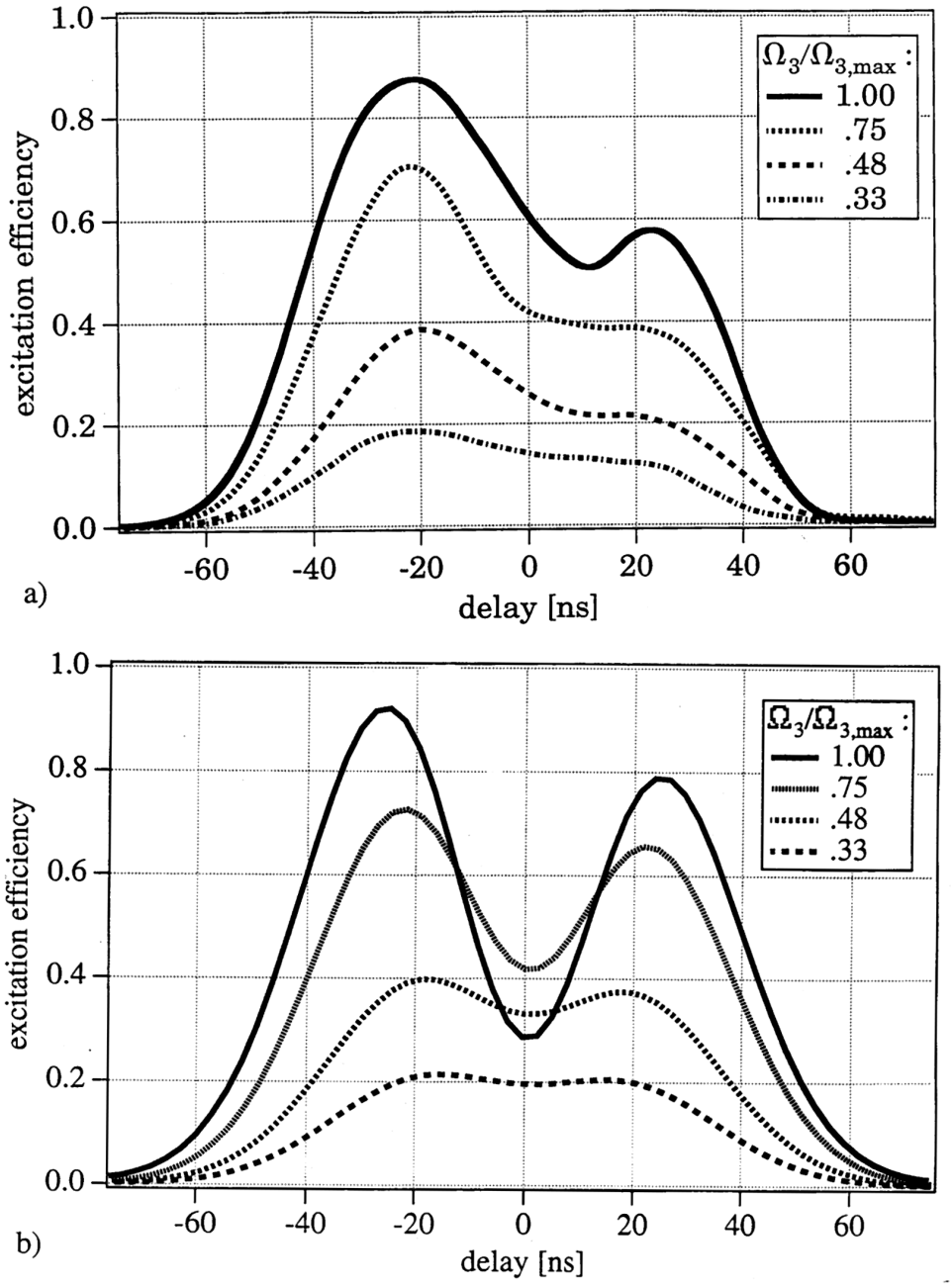

Fig. 3.12: Excitation efficiency for various 776 nm Rabi rates with the 780 nm Rabi rate held constant at its highest value. (a) Experimental, (b) from simulations.

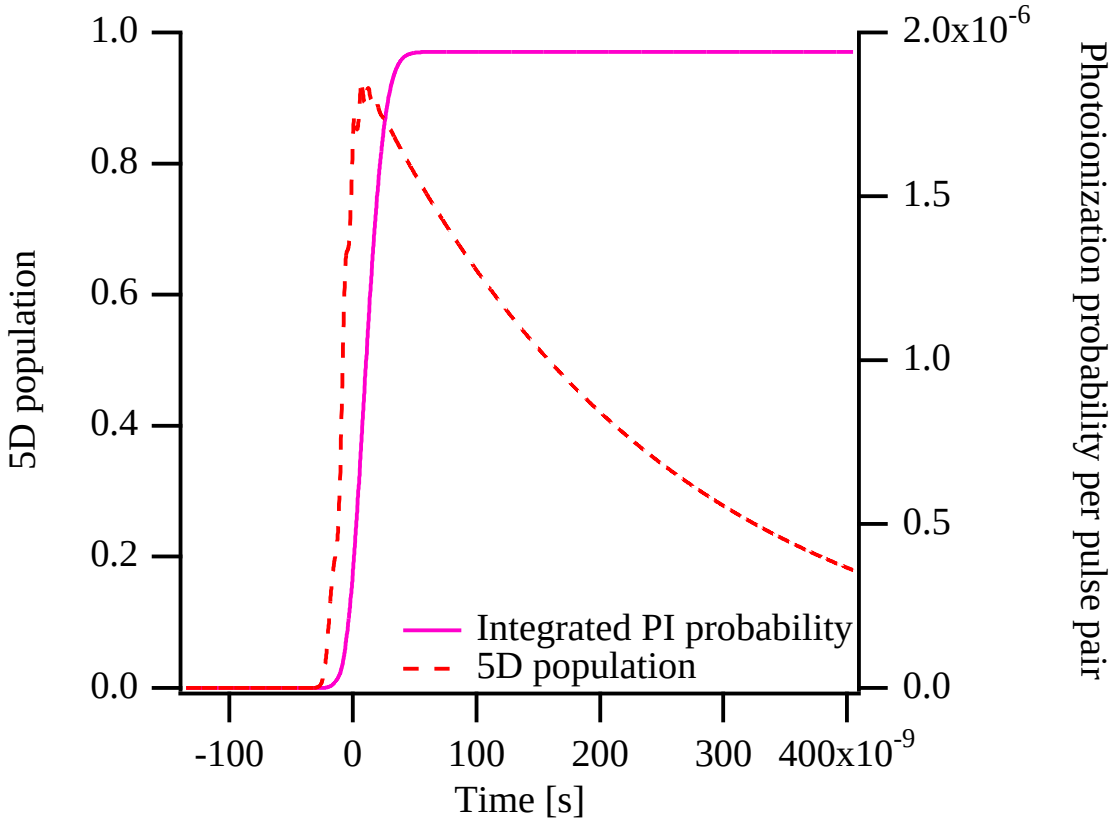

Fig. 3.13: 5D population and photoionization (PI) probability per STIRAP pulse pair, according to simulations. The integrated PI probability is the sum of the product of the PI cross section times the instantaneous total PI flux due to the STIRAP pulses. Bear in mind that the pulses occur at 50 kHz.

and $I_3 = 9.3$ W/cm^2. In Figs. 3.9, 3.10 and 3.14 the Rabi rates are given in terms of Γ, defined as

$$\Gamma \equiv \Gamma_1 = 2\pi\,(5.89\text{ MHz})\,. \tag{3.11}$$

We determine the Rabi rates by measuring the beam profiles and powers, using Eqn. 3.1 and converting thus:

$$\frac{\Omega_i}{\Gamma} = \left[\frac{I_i}{I_{i,sat}}\right]^{1/2} \tag{3.12}$$

$$\frac{\Omega_1}{\Gamma} = 0.360\left[I_1\left(\frac{\text{mW}}{\text{cm}^2}\right)\right]^{1/2} \tag{3.13}$$

$$\frac{\Omega_3}{\Gamma} = 0.101\left[I_3\left(\frac{\text{mW}}{\text{cm}^2}\right)\right]^{1/2}, \tag{3.14}$$

where $I_{i,sat}$ is the m_F-averaged saturation intensity for the ith transition. Not surprisingly, the efficiency is reduced as the Rabi rates are reduced, since Ineq. 3.10 is no longer strongly being met. The general shape of a primary peak for counterintuitive ordering, a minimum for coincident ordering and a secondary peak for intuitive ordering is shown. The simulations give a deeper minimum and a relatively larger secondary peak than the experimental results. As these characteristics do not depend on STIRAP, it is not expected that they should be as robust as the primary peak. In both experiment and simulation for varying the 780 beam Rabi rate there are two different and somewhat surprising behaviors. As the 780 intensity is reduced, the two peaks merge, and the efficiency increases for some lower Rabi rates before eventually decreasing. Evidentally, even at the highest Rabi rates, the system is not completely in the adiabatic regime. We attribute this to the relatively weak matrix element for the upper transition and to the detuning from the intermediate state (please recall that the detuning is present to reduce the effect on the trap of the leakage of 780 nm light through its AOM).

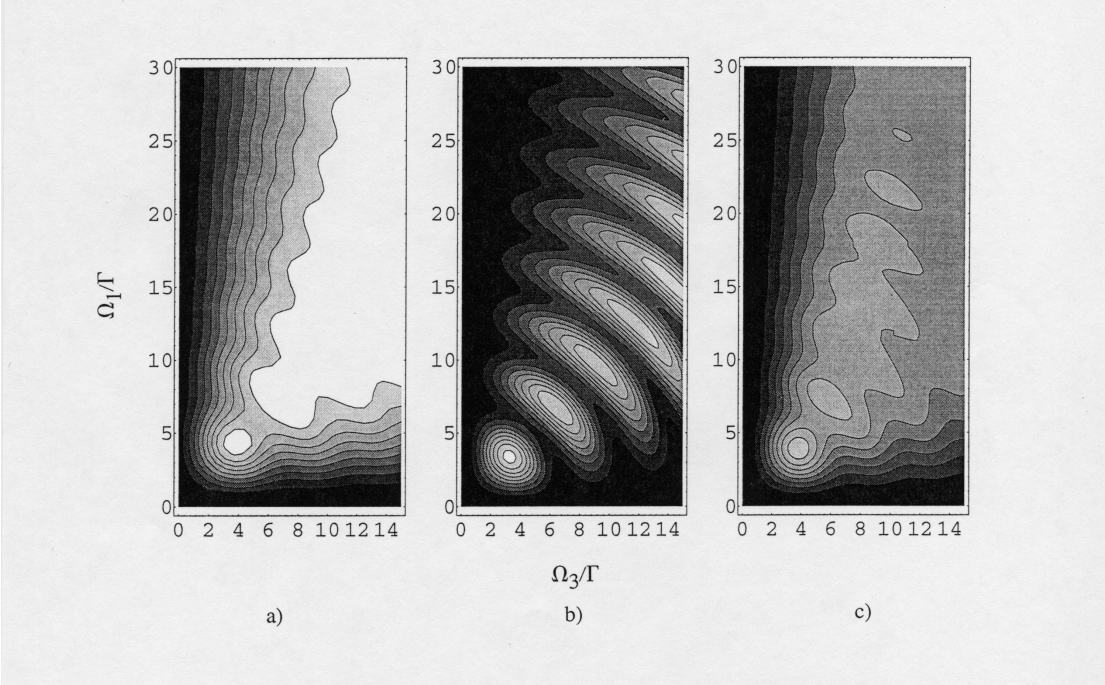

Fig. 3.14: STIRAP efficiency (from simulations) as a function of Ω_1 and Ω_3 for three different pulse delays: (a) pulses in the counterintuitive order by 20 ns; (b) coincident pulses; and (c) in the intuitive order by 20 ns. The contours reflect deciles of efficiency, lightest being the most efficient.

Let us consider Fig. 3.14 in some detail. It gives from simulations contour plots of the efficiency for different combinations of the Rabi rates Ω_1 and Ω_3 for three different pulse timings: (a) counterintuitive by 20 ns, (b) coincident, and (c) intuitive by 20 ns. Clearly the counterintuitive pulse sequence is the most efficient. In particular to be noticed is the broad swath of 90-100% efficiency at high Rabi rates for both beams. This region easily meets the criterion of Ineq. 3.10. The insensitivity of the system to the Rabi rates is a clear sign of the adiabatic regime. Note that neither the coincident or intuitive conditions have this level of efficiency, and that the coincident ordering does not have any region where a modest change in intensities does not result in a change in transfer efficiency.

The excitation efficiencies used as the ordinate in Figs. 3.11 and 3.12 are determined from Fig. 3.14(a) in the following manner. The level of 420 nm fluorescence is observed at the fixed counterintuitive delay of -20 ns. The relative change in fluorescence with regard to change in Rabi rate is then matched to a horizontal (or vertical) line in Fig. 3.14(a) for Ω_1 (or Ω_3) at the highest Rabi rate for the other STIRAP beam. Figs. 3.9 and 3.10 show the comparison of experimental data points and the calculations for Ω_1 and Ω_3, respectively. The best fit of horizontal and vertical lines is given by $\Omega_1 = 5.25\Gamma$ and $\Omega_3 = 4.0\Gamma$. This presents a significant discrepancy with our measured intensities, namely, $I_1 = 7.9$ W/cm^2 $\rightarrow \Omega_1 = 32\ \Gamma$ and $I_3 = 9.3$ W/cm^2 $\rightarrow \Omega_3 = 9.77\ \Gamma$, differing by factors of 6.1 and 2.4, respectively. We give more credence to the match with the simulation; hence, even at our highest intensities we are not in the adiabatic regime. This said, we are still in excess of 80% efficiency. At the time of this experiment there was no method to measure the efficiency directly. We were able to do this in the context of the photoionization experiment, reported in the next chapter.

We are at a loss to account for this discrepancy. We claim to know the intensities to within a factor of two, which translates into a factor of 1.4 for the Rabi rates. The average electric dipole moment described above did not yield substantially different results from simulations run summing the results from the individual seven m_F sublevels using the matrix element appropriate to each sublevel, assuming equal population distribution over the sublevels (see Fig. 3.15). Other hyperfine levels are ignored in the calculations. Our justification for doing this with regard to the lower transition is in the detuning of the first step 7.5Γ above the $F' = 4$ state, putting it 28Γ above the $F' = 3$ level. Potential off-resonant excitation into the latter level is thus insignificant. The hyperfine splittings in the $5D_{5/2}$ are rather close [29], e.g., less than 10 MHz separating the $F'' = 5$ and $F'' = 4$ states, but only the former is two-photon resonant with the ground state, so no population should be in the latter. Although the system is sensitive to laser frequency fluctuations, we rule these out as a cause of the discrepancy because: (1) primarily caused by vibrations in the laser cavities, they are much slower than the pulses, and (2) the transform-limited bandwidth of the pulses is of the order of 10^7 Hz, somewhat greater than the $\leq 2 \times 10^6$ Hz linewidth of the lasers. Radiation trapping of the 420 nm fluorescence is of negligible contribution to the discrepancy, largely due to the weak $6P \rightarrow 5S$ transition. Superfluorescence out of the 5D state was ruled out, as time-resolved measurements of the 420 nm light exhibited the expected time-dependence of the $5D \rightarrow 6P \rightarrow 5S$ decay.

In an attempt to determine the STIRAP efficiency by more direct means, we tried a quasi-cw optical-pumping experiment to depopulate the F=3 ground state, a variation on a method described in Ref. [57]. The idea is that the average number of excitation cycles (and therefore 420 nm photons) before an atom is optically pumped depends only on the relevant branching ratios. By scanning the 776 nm laser, atoms would be excited in turn to the $5D_{5/2}, F'' = 5, 4, 3$ states. Including

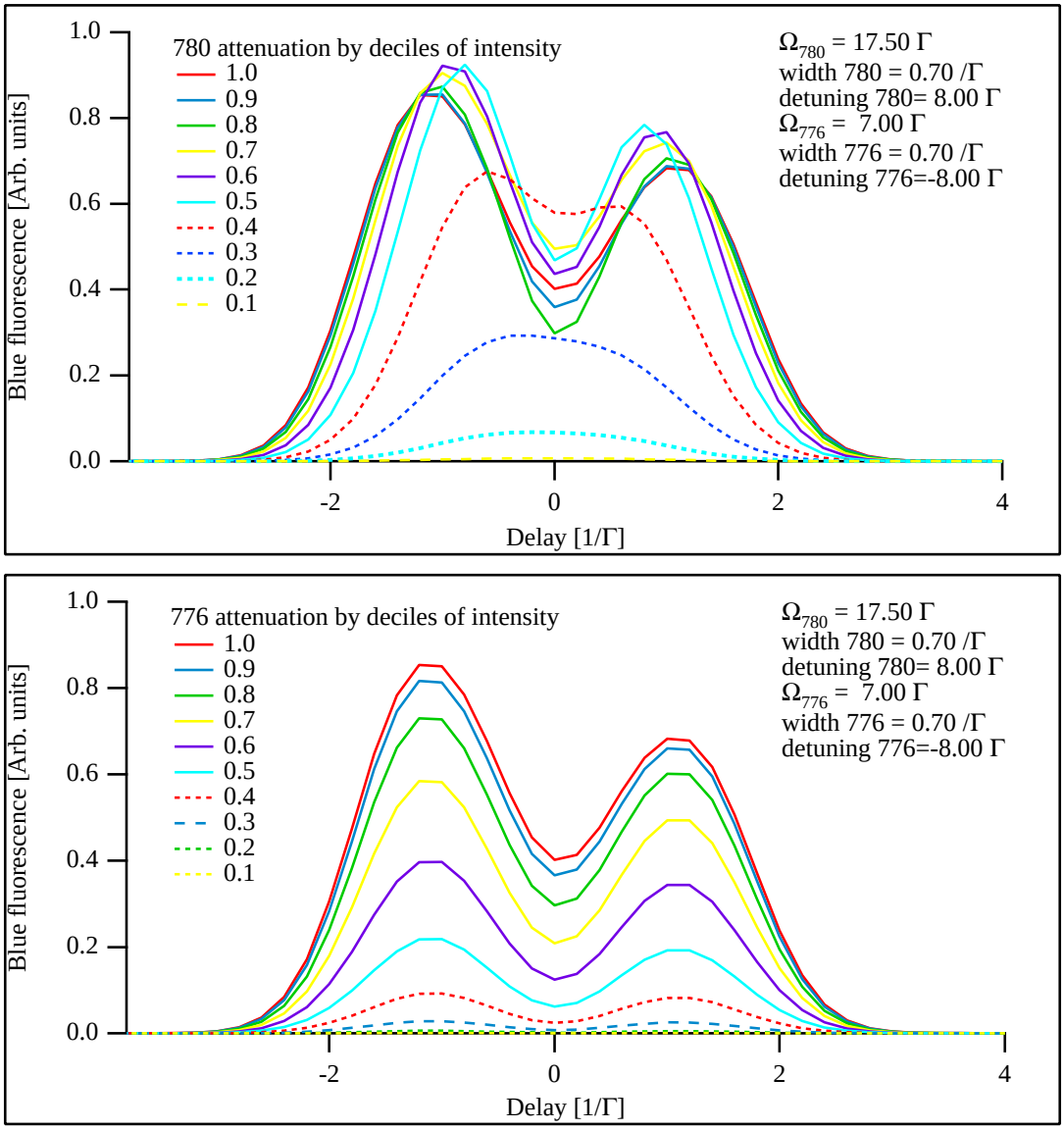

Fig. 3.15: 5D excitation (from simulations) by pulse delay and intensity, by summing individual m_F levels. $1/\Gamma = 27$ ns. The pulse width is the e^{-2} radius.

Table 3.1: Probability of decaying into the $5S_{1/2}$ F=2 ground state from various $5D_{5/2}$ hyperfine states.

initial state $[5D_{5/2}]$	Probability of decaying to F=2
F"=5	0.046
F"=4	0.34
F"=3	0.58

all possible cascades, the probability for these initial excited states to decay to the lower hyperfine ground state ($5S_{1/2}, F = 2$) as given by Ref. [28] are found in Table 3.1. (There is a typographical error in [28], where the probability for F"=4 decaying to F=2 is given as 0.034.) Consider a toy three level model with two ground states (representing $5S_{1/2}$ F = 3 and F = 2) and an excited state (representing $5D_{5/2}$). Pumping from the F = 3 ground state to the excited state occurs at a rate $R_{F'}$. There is no pumping out of the F = 2 state. Decay from the excited state into the F = 3 ground state has a probability (f) and into the F = 2 ground state (1-f). In a time t there are $t \times R_{F'} = n$ cycles. The probability over n repeated excitations is given by this sum:

$$\sum_{j=0}^{n} f^j = \frac{1}{1-f}. \tag{3.15}$$

This sum gives the average number of cycles required before the excited state decays into the F = 2 ground state. Thus the number of photons required to optically pump an atom to the F=2 ground state is given by the reciprocal of the probabilities given in Table 3.1, namely, 21.7, 2.94 and 1.72 photons, respectively. After many cycles, the time-integrated 420 nm fluorescence should occur in the ratios 21.7 : 2.94 : 1.72 for the populating of the F"=5, 4 and 3 states. Over only a few cycles we expect the ratios to be $\frac{1}{5} : \frac{1}{20} : \frac{1}{140}$, corresponding to the relative transition strengths for F" = 5, 4 and 3, respectively. This fluorescence signal is

proportional to the number of atoms in the 5D. The two-photon excitation beams are greatly attenuated, each typically measured to be $\leq 4\Gamma$ (this Rabi rate is not corrected by the factors of 6.1 and 2.4). The repetition rate varied from 50 kHz to 10 kHz, periods of 20 to 100 μs. The duty cycle varied from 80% to 90%. The two-photon pulse durations varied from to 2 to almost 40 μs. This fluorescence can be compared to the 420 nm fluorescence from a STIRAP experiment, accounting for the difference in repetition rates and pulse duration. Since the optical pumping yields a well-defined number of 420 nm photons per atom, it can, in principle, serve as a means of calibrating the STIRAP efficiency.

Unfortunately, the results of this experiment were very disappointing. The ratios were not reproducible on a regular basis. Often the change in ratio with regard to pulse duration was not a monotonic function. Sometimes there was no significant change in ratio. For instance, for one run the ratio of F"=5 to F"=4 remained about 9:1 as the length of the pulses changed from 5 to 20 μs. Given this situation no attempt was made to determine the excitation efficiency. Considerable effort was expended in attempting to make this experiment work. In retrospect it seems that there were several sources of problems. The prime source was optical feedback from the 776 nm high-power laser into its low-power master. Because of the relatively narrow separation between the 5D hyperfine states (about 9.5 MHz between each of 5 to 4 and 4 to 3), there are additional questions about power broadening in the two-photon spectroscopy and about the linewidth of the low-power laser (which lead to questions about the linewidth of the injection-locked high-power laser). There was also some feedback from the face of the 776 beam's AOM, which was identified and corrected by a change in alignment. In the next chapter a technique employing photoionization will be discussed. This technique gives a rather precise number for STIRAP efficiency. Furthermore, the rearrangement of optical isolators which reduces the feedback

from high-power to low-power lasers will be described.

Chapter 4

Photoionization

4.1 Introduction and Theory

One advantage of using a cell magneto-optical trap (MOT) to trap atoms is that it has a fixed steady-state number of neutral atoms. When atoms are ejected from the trap by whatever manner, the trap loss rate is changed and the trap fluorescence goes down accordingly. Measuring the change in trap loss rate gives a means to examine the process effecting that loss. In this chapter photoionization (PI) is the process examined. The loss rate due to the photoionizing radiation is measured, as is the intensity of the radiation. These data along with the fraction of time the atom spends in the desired atomic state yield the absolute photoionization cross section (see Ref. [6] where the technique was applied to Rb $5P_{3/2}$). Among the benefits of this method is that one need not know the trap density or the absolute number of atoms, nor is there any need to calibrate ion detection equipment. In addition to Ref. [6] it has been used in other experiments involving Rb [58], Cs [59,60], and Mg [61], and a variation has been used to determine the cross section for electron collisions [62,63].

In this experiment the trap-loss technique is applied for the first time to a higher-lying excited state (i.e., not the first excited state involved in the cycling transition), the Rb $5D_{5/2}$ [55]. Photoionization from such higher states is useful in research on plasmas and in sensitive detection of selected atomic states. From

PI research one can learn about radiative recombination, an important aspect of astrophysical and other low-temperature plasmas. Absolute PI cross sections and their energy dependence provide tests of theories of nonhydrogenic wavefunctions. Thus there are several applications of PI research, especially concerning higher-lying atomic levels. We are particularly interested in studying PI out of the Rb $5D_{5/2}$ because the excitation pulses themselves are capable of ionizing this state, and we want to be able to account for this loss mechanism when we investigate 5D-5S collisions. Working in the MOT described in Chapters 1 and 2 and employing the STIRAP process described in Chapter 3, there is now available a large number of atoms in the $5D_{5/2}, F'' = 5$ state. These atoms are ionized by laser light of diverse wavelengths, two of them produced by continuous wave (cw) lasers and two produced by a pulsed laser.

The basic idea of the cw ionization is to measure the time-averaged effect of many rapidly repeated (here 50 kHz), but inefficient (e.g., 10^{-5} probability), photoionization events. In this case the PI light is always present, but the $5D_{5/2}$ population is pulsed. The pulsed-laser PI, on the other hand, is a single-shot experiment. Due to the high pulsed-laser intensity, very efficient PI of atoms in $5D_{5/2}$ can be achieved in one pulse. These two cases will be discussed separately.

Consider the cw case first. Trapped atoms are repeatedly excited at a rate R_{rep} (= 50 kHz) by STIRAP pulses to the $5D_{5/2}$ state with an efficiency η. They exponentially decay from that state with a characteristic lifetime of $\tau_{5D} = 241$ ns. The excited-state fraction f_{5D} resulting from this process is:

$$f_{5D} = R_{rep}\eta\tau_{5D}. \tag{4.1}$$

This time-averaged excited-state fraction is usually less than 1%. While the atoms are in the 5D level, the PI rate is given by the product of the photon flux Φ and the PI cross section σ. Thus the time-averaged PI rate out of the $5D_{5/2}$ state is

given by:

$$\langle \Gamma_{PI} \rangle = \Phi \sigma R_{rep} \eta \tau_{5D}. \tag{4.2}$$

The photon flux Φ is given by:

$$\Phi = \frac{I}{h\nu} = \frac{I\lambda}{hc}, \tag{4.3}$$

where I is the intensity of the PI light, λ is its wavelength (related to its frequency ν through the speed of light c), and h is Planck's constant. As an example take 647 nm light of 10 W/cm^2 intensity. This typically yields a PI probability (per $5D_{5/2}$ excitation) of 2.7 $\times 10^{-5}$ or at a 50 kHz repetition rate a time-averaged PI rate of about 1.3/s.

Consider the number of atoms in the MOT. The atoms load at a rate L from the background vapor and leave the trap at a rate $\Gamma_{tot} N$ which accounts for all loss mechanisms. Separating PI from other such mechanisms (collisions with hot background atoms, ultracold collisions between trapped atoms, loss induced by the STIRAP process), one may write:

$$\dot{N} = L - \Gamma_0 N - \langle \Gamma_{PI} \rangle N. \tag{4.4}$$

As her project in the Research Experience for Undergraduates program, Melanie Kittle determined that this MOT is in the constant density regime (that is, trap density is limited by radiation trapping [56]). Refer to the following chapter for details. In the constant density regime the loss rate due to ultracold collisions is constant [8]. With N_0 as the steady-state number of trapped atoms the solution to Eqn. 4.4 is

$$N_0 = \frac{L}{\Gamma_0 + \langle \Gamma_{PI} \rangle}, \tag{4.5}$$

a 1/(1+x) dependence, where x is a normalized PI intensity. The trap loads exponentially with a time constant the inverse of which is the total loss rate $\Gamma_{tot} = \Gamma_0 + \langle \Gamma_{PI} \rangle$. For measurements involving cw photoionizing radiation the

trap fluorescence was recorded in four situations: (1) a zero level was taken, in which the magnetic field coils were turned off but all laser fields were present, including the photoionizing beam; (2) the trap was allowed to load in the presence of PI; (3) a zero level was taken in the absence of PI; and (4) the trap is loaded without PI. An example of this is given in Fig. 4.1. During all measurements the trap, repump and STIRAP beams are pulsed (50 kHz, 85% duty cycle for the trap and repump), and the cw ionizing beams are on continually. The cw beams had no noticeable effect on the trap in the absence of STIRAP. The loading curve in the absence of PI yields Γ_0.

The experiment is run by repeating this set of loading curves for different ionizing intensities. An example of plotting the ratios of the steady-state fluorescence level while photoionizing to the level when not photoionizing is shown in Fig. 4.2. The data are fit to Eqn. 4.5, shown as the dashed line. From this and from Eqn. 4.2 one can determine the cross section. Note that the STIRAP efficiency η is required for this determination. It is obtained from the pulsed measurements discussed below.

An alternative method of determining the PI cross section is by graphing the total loss rate Γ_{tot} (determined from the loading curve) versus the photoionizing intensity, an example of which is shown in Fig. 4.3. The intercept of the linear fit gives Γ_0, and from the slope one can determine the cross section. This method yields cross section values which are consistent with those determined from Eqn. 4.5, but they are less accurate and hence are not used in the ultimate results.

Some factors which could adversely affect the 1/(1+x) analysis of the cw data were considered and dismissed. Recombination of photoelectrons and ions would be strongly favored at low photoelectron energies, but no such behavior was detected. Furthermore, a crude measurement involving the sudden introduction of

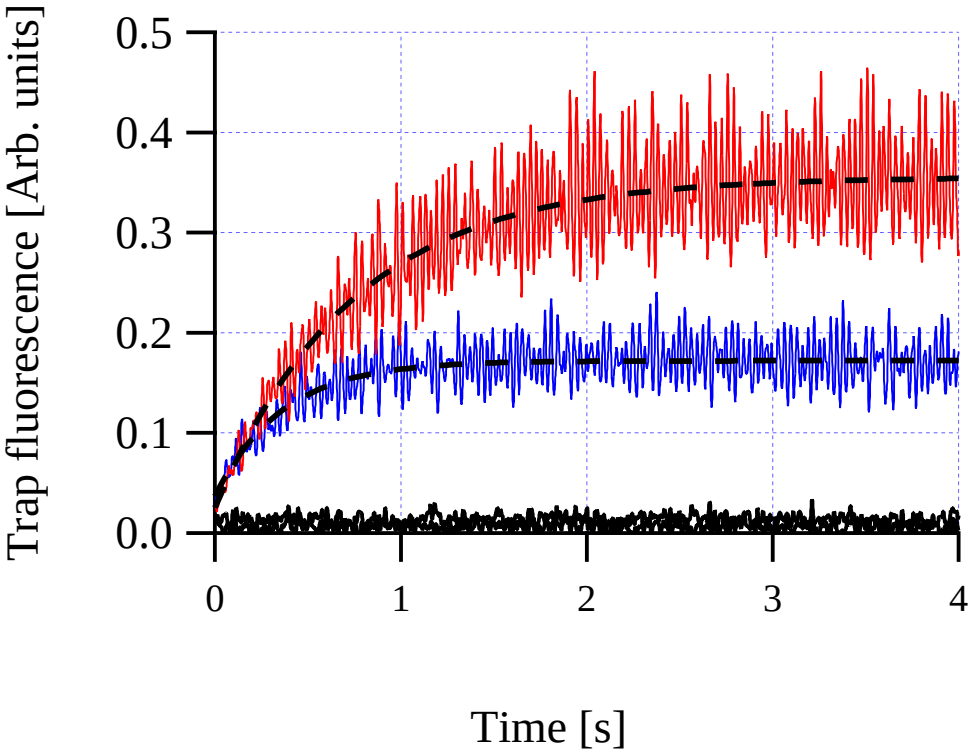

Fig. 4.1: Loading curves showing the effect of cw photoionizing light (6.9 W/cm^2 at 788 nm). The data are fit to exponentials. The uppermost curve shows the trap fluorescence in the presence of STIRAP but the absence of PI. The second curve shows the effect of STIRAP and PI. Two curves lie near the ordinate axis. These are zero levels for each loading curve, recording all stray light while the magnetic field is off.

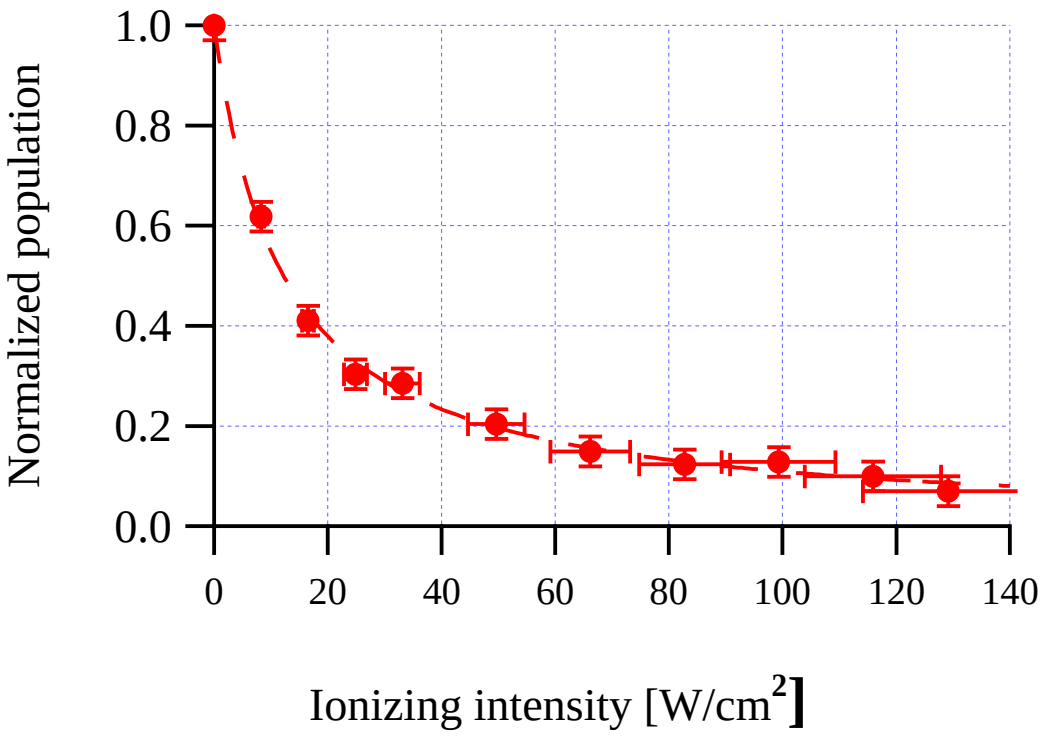

Fig. 4.2: An example of analyzed data of PI by a cw source, in this case the 788 nm diode. The fraction of atoms remaining trapped is plotted against the intensity of the 788 nm beam. The line is a fit to Eqn. 4.5.

an electric field (using metallic plates outside the glass vacuum cell) to separate the photoelectrons and the ions likewise revealed no observable effect. Another factor is possible saturation of photoionization during the 5D lifetime, but our highest intensities are too dim for this. Furthermore, had this behavior been evinced, the analysis could simply have covered the subset of data before the onset of saturation. A third possible problem is that at high PI intensities, the trap number N_0 may be reduced below the radiation-trapping limit and hence the loss rate due to ultracold collisions will fall off. At these high PI intensities, however,

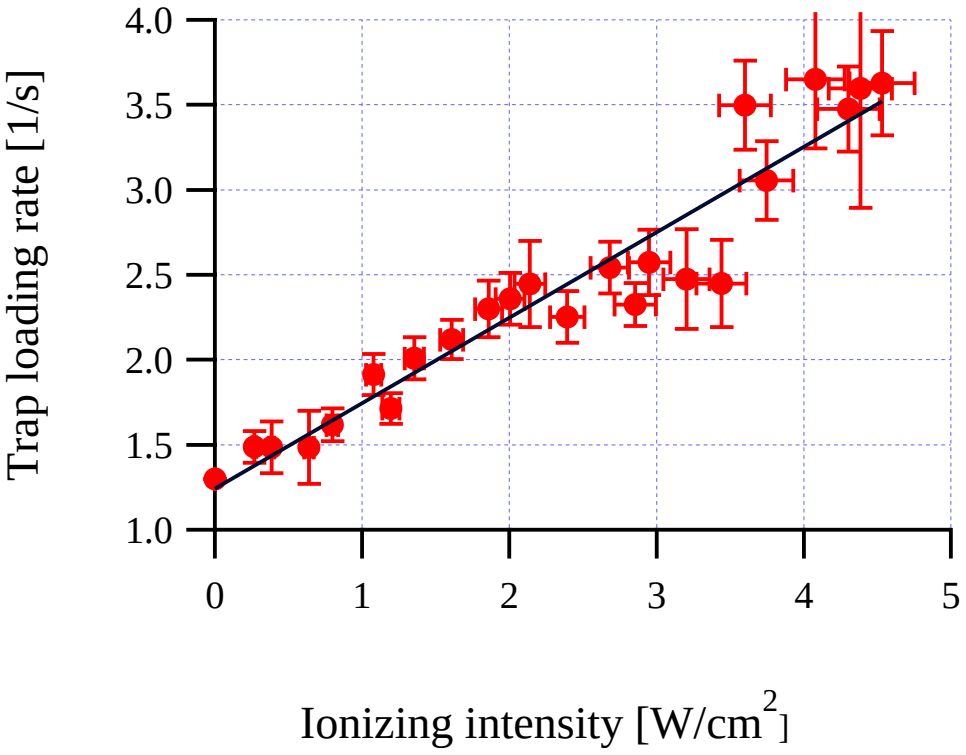

Fig. 4.3: The total trap loss rate versus the intensity of the photoionizing 788 nm beam. The total loss rate is from loading curves. The line is a linear fit, yielding Γ_0 and from the slope the PI cross section.

the PI loss rate dwarfs the collision loss rate. Finally, at high PI intensity the trap loading rate L can be reduced by photoionization of atoms as they enter the trap [58,59]. This potential effect is reduced in this case because the STIRAP beams intersect a small fraction of the MOT capture volume.

A different analysis is required for photoionization by short pulses. The pulses are of 5 to 7 ns in duration (FWHM), short compared to the 5D lifetime of 241 ns [45]; hence, the relevant time factor becomes the pulse duration. The repetition rate of the experiment is slowed from 50 kHz to 1 Hz. For the measurement of the PI cross section at the pulsed light wavelengths the ionizing pulse is coincident (to within 5 ns) with the second STIRAP pulse. Thus the 5D atoms have little chance to decay before being exposed to the PI pulse. The number of atoms in the 5D as a function of time is (the instantaneous rate of PI in time t is R_{PI}):

$$\dot{N_{5D}} = -R_{PI} N_{5D} \tag{4.6}$$

$$N_{5D}(t) = N_0 e^{-\int_{-\infty}^{t} R_{PI}\, dt'}. \tag{4.7}$$

Accounting for the STIRAP efficiency, we get a probability of the photoionization of an atom by a single pulse of:

$$P_{PI} = \eta \left(1 - e^{-\frac{\sigma F \lambda}{hc}}\right). \tag{4.8}$$

The fluence $F = \int_{-\infty}^{\infty} I dt$ of a single PI pulse can be such as to photoionize most of the 5D population. Consider a 1064 nm, 5 ns pulse with F = 0.025 J/cm^2 repeating at 1 Hz. The energy per photon is 1.867 $\times 10^{-19}$ J, thus there are about 1.34 $\times 10^{17}$ photons/cm^2 in each of these pulses. The 5D PI cross section at this wavelength is 17.7 $\times 10^{-18}$ cm^2, yielding 2.37 as the coefficient of the exponential in Eqn. 4.8.

At the 1 Hz repetition rate the trap begins to reload, whereupon it experiences another sequence of STIRAP and PI pulses, as is shown in Fig. 4.4. The sev-

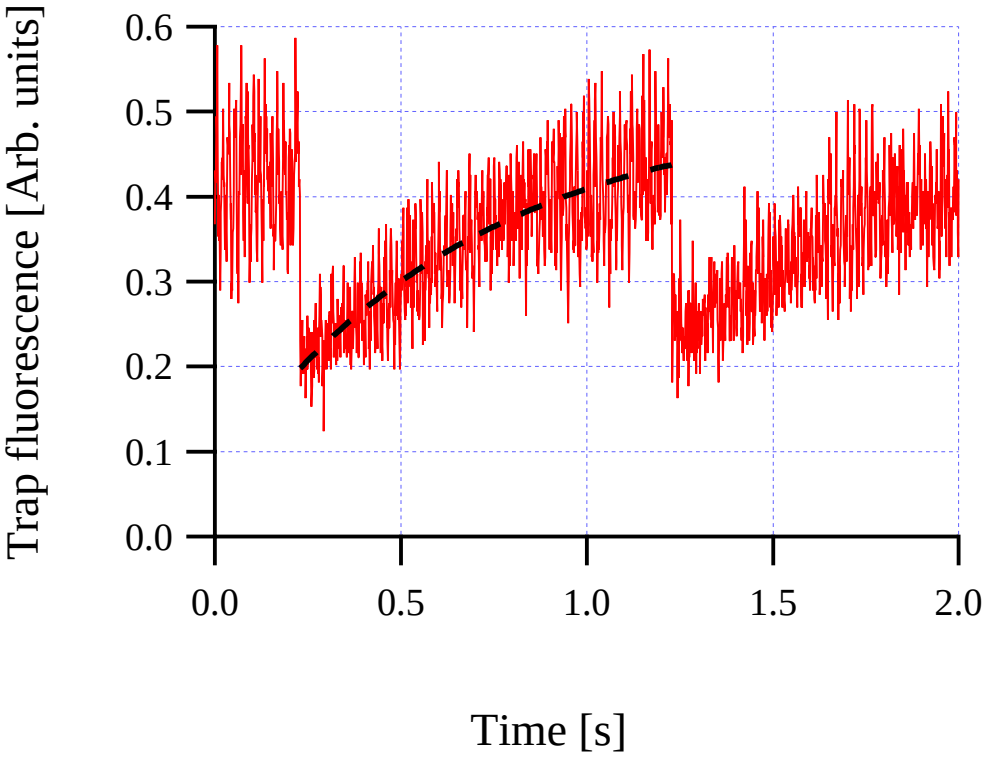

Fig. 4.4: The effect of the Nd:YAG pulse on trap fluorescence. The fit is an exponential.

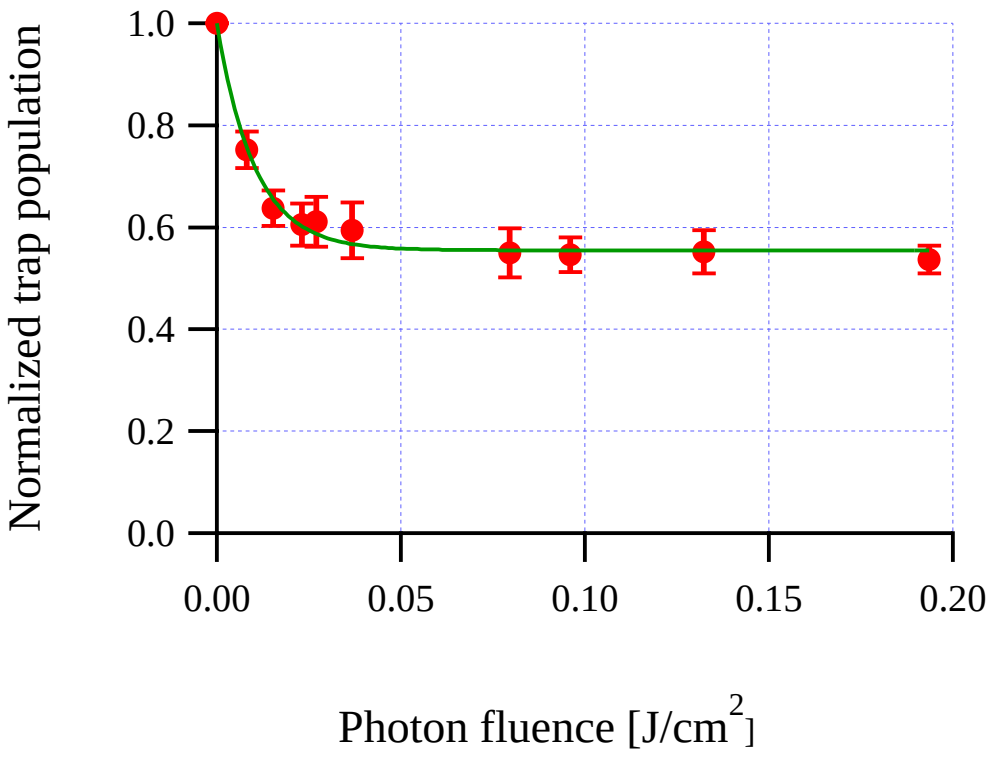

Fig. 4.5: Normalized trap population remaining as a function of Nd:YAG pulse fluence at 1064 nm. The curve is a fit to the complement of Eqn. 4.8.

eral sequences are fit to exponentials, so that the fraction of loss is the beginning value of one exponential compared to the ending value of the preceding exponential. Several sequences at the same pulse fluence are averaged, and the process is repeated at several different fluences. An example of this is shown in Fig. 4.5. Consider the level part of the fit, i.e., when PI is saturated. As seen in the $F \to \infty$ limit of Eqn. 4.8, this region gives a direct value for the STIRAP efficiency, in this particular case 45%, a rather low value for the photoionization experiment. In Chapter 3 we claimed an efficiency in excess of 80%; the lower efficiencies in the PI experiment are due to lower STIRAP intensities due to the increased area

of the beams (used to ensure more uniform illumination of the cloud of atoms). The difficulty in calculating the efficiency which was present in Chapter 3 is now alleviated. The values for STIRAP efficiency measured in this manner are used to determine the cw cross sections. Pulsed and cw data (for the Kr laser at 647 nm) are taken in the same run as to ensure a constant value of η. The Kr laser is used to determine STIRAP efficiency for the 788 nm runs.

The ability of the pulsed radiation to saturate the PI is an aid in reckoning the 5D lifetime, a quantity needed for the cw calculations. In particular cooperative effects need to be ruled out, such as superradiance out of the 5D. An intense Nd:YAG pulse at 1064 nm was moved in time from slightly before the STIRAP excitation to ~200 ns afterward. As the 5D population decays, proportionally fewer atoms are available for PI. The PI probability as a function of delay therefore maps out the exponential decay of the 5D level, as is shown in Figs. 4.6 and 4.7. Light at 1064 nm cannot photoionize states lower than the 5D, but light at 532 nm can. This introduces a complication when the PI pulse is at significant delay from the STIRAP excitation, because lower states may then have appreciable population via cascades from the 5D. This is also true and more worthy of notice for the cw measurements. Let us take some time to consider the issue.

4.2 Contribution of the 6P State to the Measured PI Cross Section

For those wavelengths which can do it (788 nm, 647 nm and 532 nm), there can be photoionization out of states other than the 5D. This contribution has to be accounted for in measuring the 5D cross section. Table 4.1 lists the energies (and the equivalent wavelengths) required to photoionize (determined from Ref. [64]; also refer to Fig. 4.9). The percentage of time an atom spends in these states compared to time spent in the 5D is the ratio of lifetimes times the appropriate branching ratios [45] (see Fig. 4.10), as calculated in Eqns. 4.9, 4.10 and 4.11.

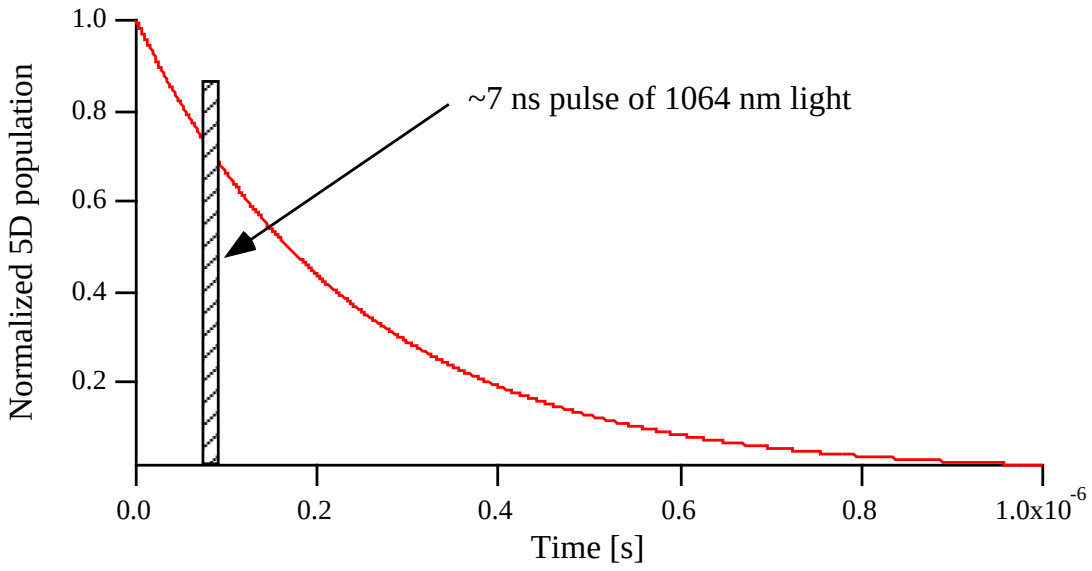

Fig. 4.6: The exponential decay of the Rb $5D_{5/2}$ population along with an ionizing pulse of light. The pulse can move in time with respect to the peak population (in the vicinity of the peak intensity of the second STIRAP pulse). As the ionizing pulse moves away from the STIRAP pulses, fewer atoms are left to be ionized, hence fewer atoms are lost from the trap. This change plotted against the ionizing pulse delay maps out the 5D lifetime.

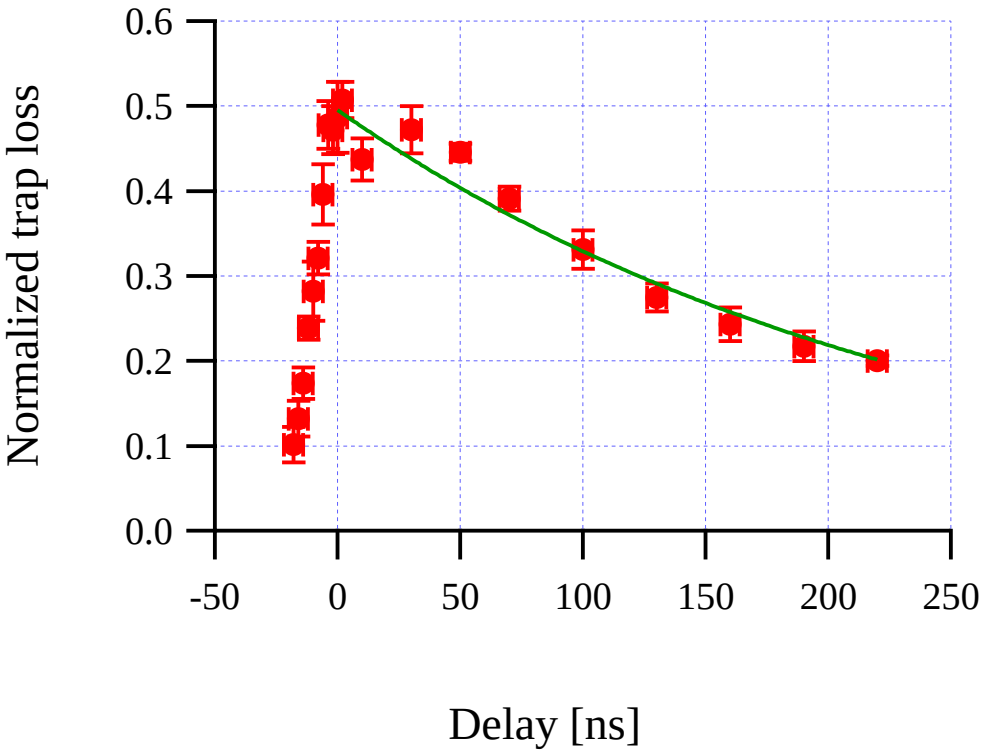

Fig. 4.7: Normalized trap loss as a function of separation between the STIRAP pulses and the 1064 nm Nd:YAG pulse. The fit is an exponential decay, yielding a lifetime of 245(16) ns.

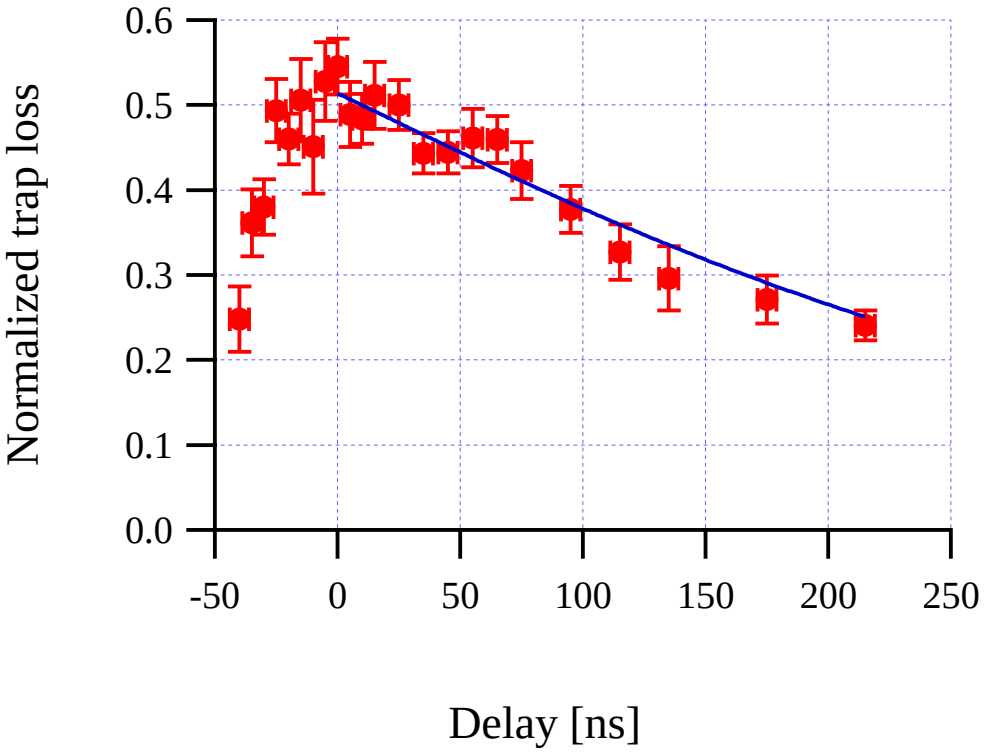

Fig. 4.8: Normalized trap loss as a function of separation between the STIRAP pulses and the 532 nm Nd:YAG pulse. Because the 6P can also be photoionized by 532 nm light, the fit includes contributions from that state as well, as is explained in the text.

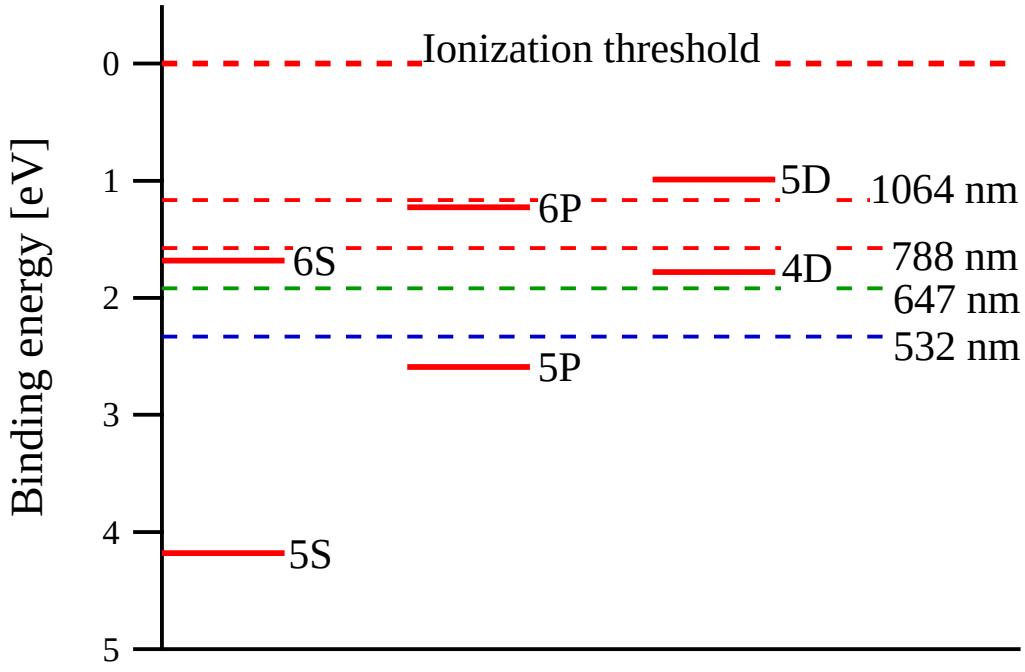

Fig. 4.9: ^{85}Rb energy levels with the four ionizing wavelengths used this experiment. The dashed lines indicate the smallest binding energies which can be photoionized by the respective wavelengths.

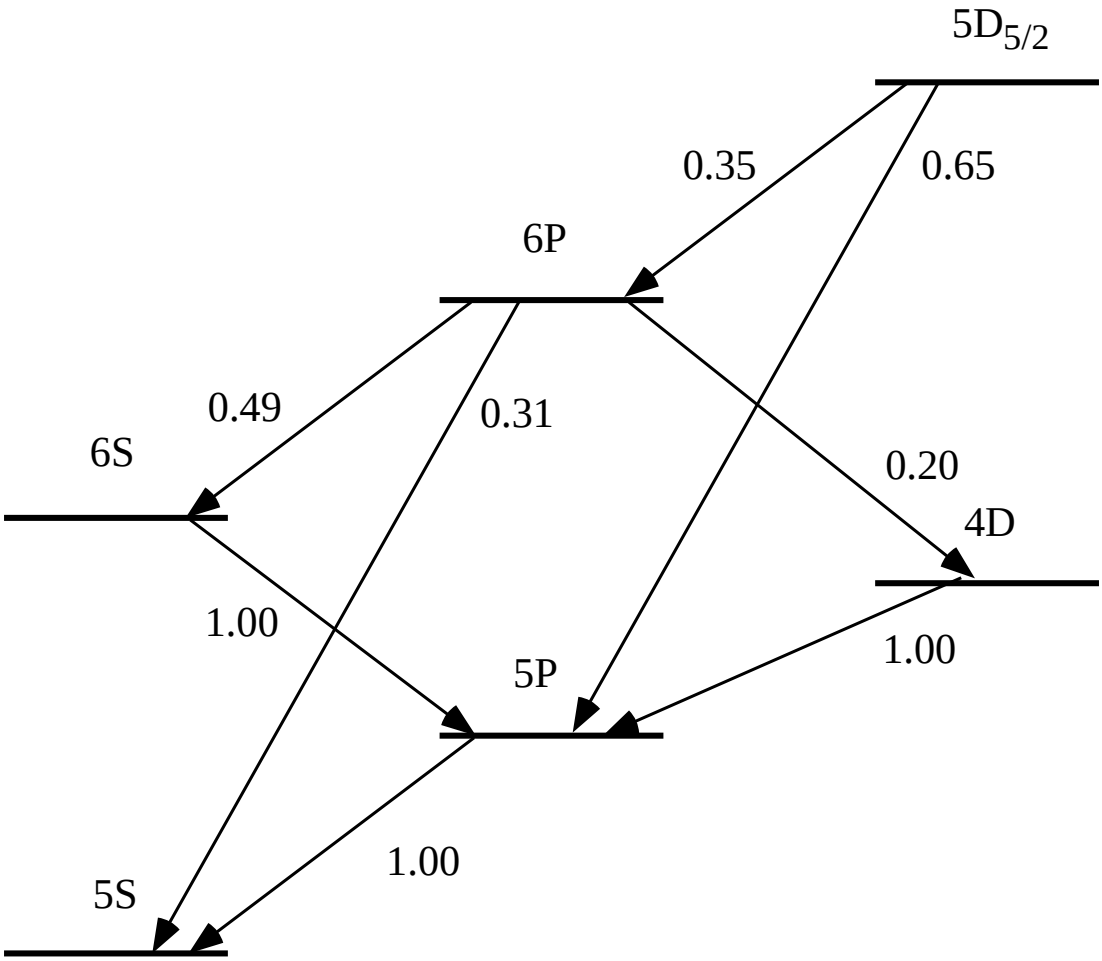

Fig. 4.10: Some ^{85}Rb states and their branching ratios (which were taken from Ref. [45]).

Table 4.1: States relevant to the photoionization experiment, their energy below the ionization threshold in cm^{-1} and eV, and the maximum wavelengths required to photoionize.

state	binding energy [10^4 cm^{-1}]	binding energy [eV]	wavelength [nm]
5S	3.37	4.18	297
5P	2.09	2.59	479
4D	1.434	1.78	698
6S	1.356	1.68	738
6P	0.9898	1.227	1010
5D	0.7991	0.991	1252

$$6P: \quad \tfrac{109}{241} \times 0.35 \quad = 15.8\% \tag{4.9}$$

$$6S: \quad \tfrac{51.3}{241} \times 0.35 \times 0.49 \quad = 3.7\% \tag{4.10}$$

$$4D: \quad \tfrac{84}{241} \times 0.35 \times 0.20 \quad = 2.4\%. \tag{4.11}$$

Excepting the 6P contribution, we feel justified in ignoring PI out of these other states in light of our overall uncertainties. In the instance of the 532 nm Nd:YAG pulse there is no PI out of any state until the pulse occurs. In this case the ionizing pulse is increasingly delayed with respect to the STIRAP pulses, freely allowing the population to decay to the 6P. The PI pulse therefore samples a snapshot of the populations. Thus it would be beneficial to know how the populations are distributed between the 5D and the 6P.

Jared Bartholomew, another participant in the Research Experience for Undergraduates (REU) program, analyzed this as part of his project. A simple rate equation model is used to describe the relative populations of the 5D and 6P states over time. The entire relevant population is assumed to be in the 5D (=1) and none in the 6P (=0) at time t=0, and both states are assumed to be unpopulated

at time t=∞ as all atoms ineluctably decay to the ground state. Photoionization is not taken into account. The 5D state decays exponentially, feeding the 6P according to the branching ratio $B_{5D\rightarrow 6P} = 0.35$. The decay rates ($\Gamma = 1/\tau$) are indicated by Γ_{5D} and Γ_{6P}.

$$\dot{N_{5D}} = -\Gamma_{5D} N_{5D}(t) \tag{4.12}$$

$$\dot{N_{6P}} = B_{5D\rightarrow 6P}\Gamma_{5D} N_{5D}(t) - \Gamma_{6P} N_{6P}(t) \tag{4.13}$$

These equations have the following solutions, taking N_0 to be the number of atoms initially in the 5D and setting $N_i \equiv N_i(t)$:

$$N_{5D} = N_0 e^{-\Gamma_{5D} t} \tag{4.14}$$

$$\dot{N_{6P}} + \Gamma_{6P} N_{6P} = 0.35\Gamma_{5D} N_0 e^{-\Gamma_{5D} t} \tag{4.15}$$

$$\frac{d}{dt}\left(e^{\Gamma_{6P} t} N_{6P}\right) = 0.35\Gamma_{5D} N_0 e^{-\Gamma_{5D} t} e^{\Gamma_{6P} t} \tag{4.16}$$

$$\int d\left(e^{\Gamma_{6P} t} N_{6P}\right) = 0.35\Gamma_{5D} N_0 \int e^{(\Gamma_{6P}-\Gamma_{5D})t} dt \tag{4.17}$$

$$e^{\Gamma_{6P} t} N_{6P} = \frac{0.35\Gamma_{5D} N_0}{\Gamma_{6P} - \Gamma_{5D}} e^{(\Gamma_{6P}-\Gamma_{5D})t} + C \tag{4.18}$$

$$N_{6P} = \frac{0.35\Gamma_{5D} N_0}{\Gamma_{6P} - \Gamma_{5D}} e^{-\Gamma_{5D} t} + C e^{-\Gamma_{6P} t} \tag{4.19}$$

$$N_{6P} = \frac{0.35\Gamma_{5D} N_0}{\Gamma_{6P} - \Gamma_{5D}} \left(e^{-\Gamma_{5D} t} - e^{-\Gamma_{6P} t}\right), \tag{4.20}$$

employing the boundary conditions on the population in 6P at t=0 and t=∞. Taking Γ_{5D} and Γ_{6P} to be the inverse of the lifetimes of their respective states (241 and 109 ns [45]) leads to evolution of population as shown in Fig. 4.11. The 6P cross section could have had a pronounced effect on the PI results, if the cross section were large enough. Examine Fig. 4.12. The 6P and 5D populations in Fig. 4.11 are weighted by the theoretical values of their cross sections and then summed. The likelihood of PI is proportional to these sums. Curves are presented for the predicted value of the 6P cross section and for this value times 3, times 10, and divided by 3. The experiment (Fig. 4.8) did not reveal any behavior approaching the curve for the largest cross section; however, given the

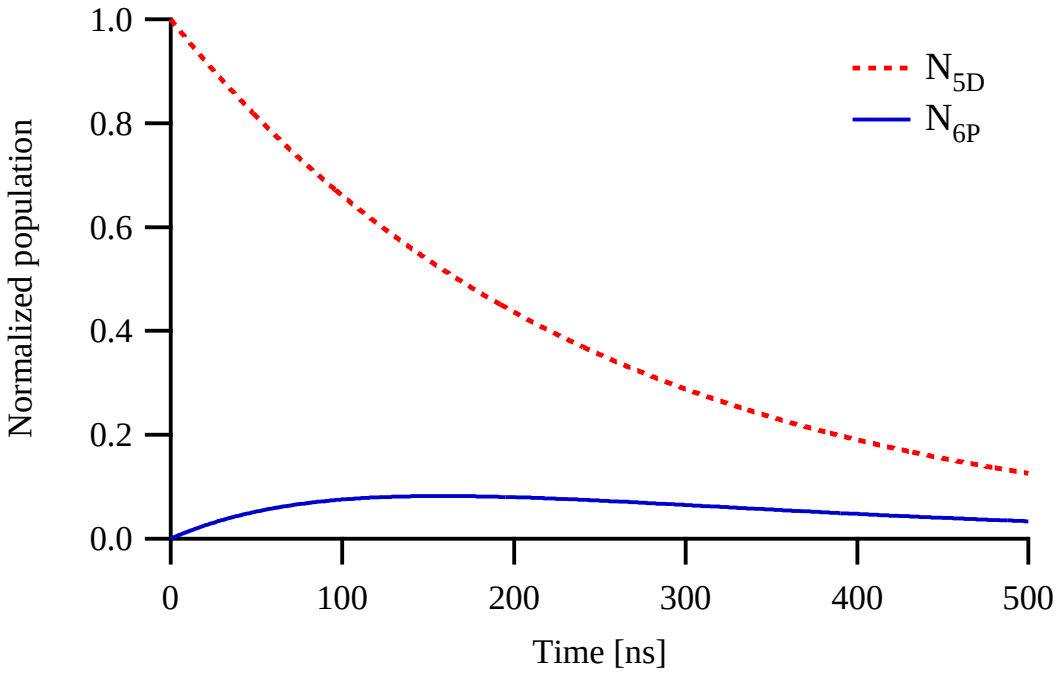

Fig. 4.11: Population in the 5D and 6P states as a function of time. The maximum 6P population at time $\tau_{6P} = 109$ ns is 12% of the 5D population at that time.

uncertainty in the measurements we cannot make a stronger statement than that our observed results are consistent with the theoretical predictions.

The data in Fig. 4.8 are fit to Eqn. 4.20 using 241 ns as the 5D lifetime and 109 ns as the 6P lifetime [45]. The cross sections used for the 5D and 6P states at 532 nm are derived from theory, as described below in Section 4.4. The contribution of PI out of the 6P state is also accounted for in the cw measurements at 788 nm and 647 nm. These theoretically calculated 6P cross sections at the 788, 647 and 532 nm wavelengths are 8.5, 6.6 and 4.8 Mb, respectively. On average an atom spends about 16% as much time in the 6P as in the 5D (see Eqn. 4.9; this is also the ratio of the integrals over time of the two curves in Fig. 4.11).

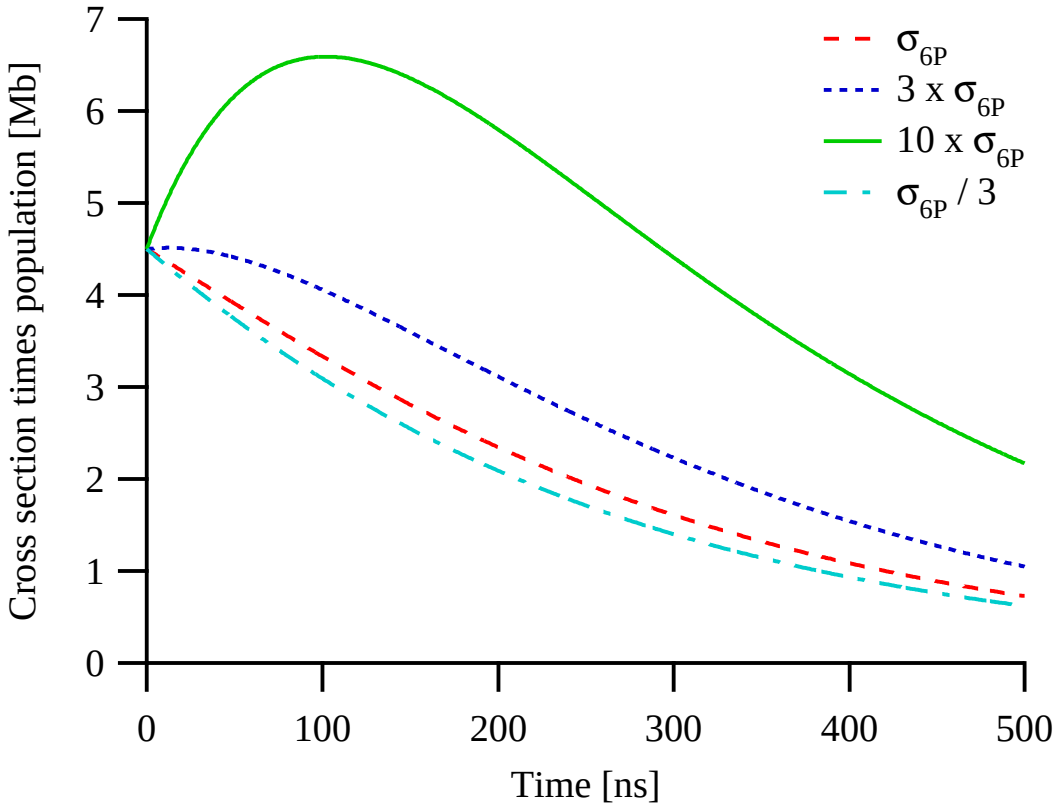

Fig. 4.12: The sum of 5D and 6P populations weighted by their cross sections at 532 nm. The probability of photoionization is directly proportional to these curves. The curve labelled "6P" is used to fit the data in Fig. 4.8.

This percentage times the 6P cross section is subtracted from the measured cross sections. Thus the measured cross section at 788 nm is reduced from 12.2 to 10.9 Mb and at 647 nm from 8.6 to 7.6 Mb.

4.3 Set-up and Technique

Most of the apparatus necessary for this experiment has been described in earlier chapters. Of the new equipment the most important are the lasers providing the ionizing light, a Mitsubishi 64114R diode at 788 nm free-running wavelength, a Coherent Innova 200 Series Kr ion laser running at 647 nm and (on loan from the National Institute of Standards and Technology) a Continuum Minilite Neodymium-doped Yttrium-Aluminum-Garnet (Nd:YAG) laser running at its first two harmonics at 1064 and 532 nm. The diode laser is mounted on the optics table of the magneto-optical trap. The other two lasers are located in an adjoining laboratory. Their beams are brought to the apparatus through a two inch diameter hole in the wall between the laboratories. In addition to the new lasers the coil-switching circuit and the SRS DG535 Pulse Generator, both described in Chapter 2, are used here for the first time. During the pulsed measurements the internal triggering of the Nd:YAG is used as the anchor for all other pulses. LabVIEW programs and IGOR macros used in the acquisition and analysis of data are described in appendices. As mentioned above, STIRAP efficiency is measured directly in the pulsed experiments. Some Kr laser experiments are also run with the Nd:YAG at the same time, so that the Kr laser in turn can act as the calibration standard for the 788 nm diode runs.

A review of Fig. 4.13 shows that all of the windows into the trap are already used by the trapping beams, the STIRAP beams, the charge-coupled device (CCD) camera and the photo-multiplier tube (PMT). Thus some windows had to serve double duty. After being focused, the cw Kr beam is brought through the backside

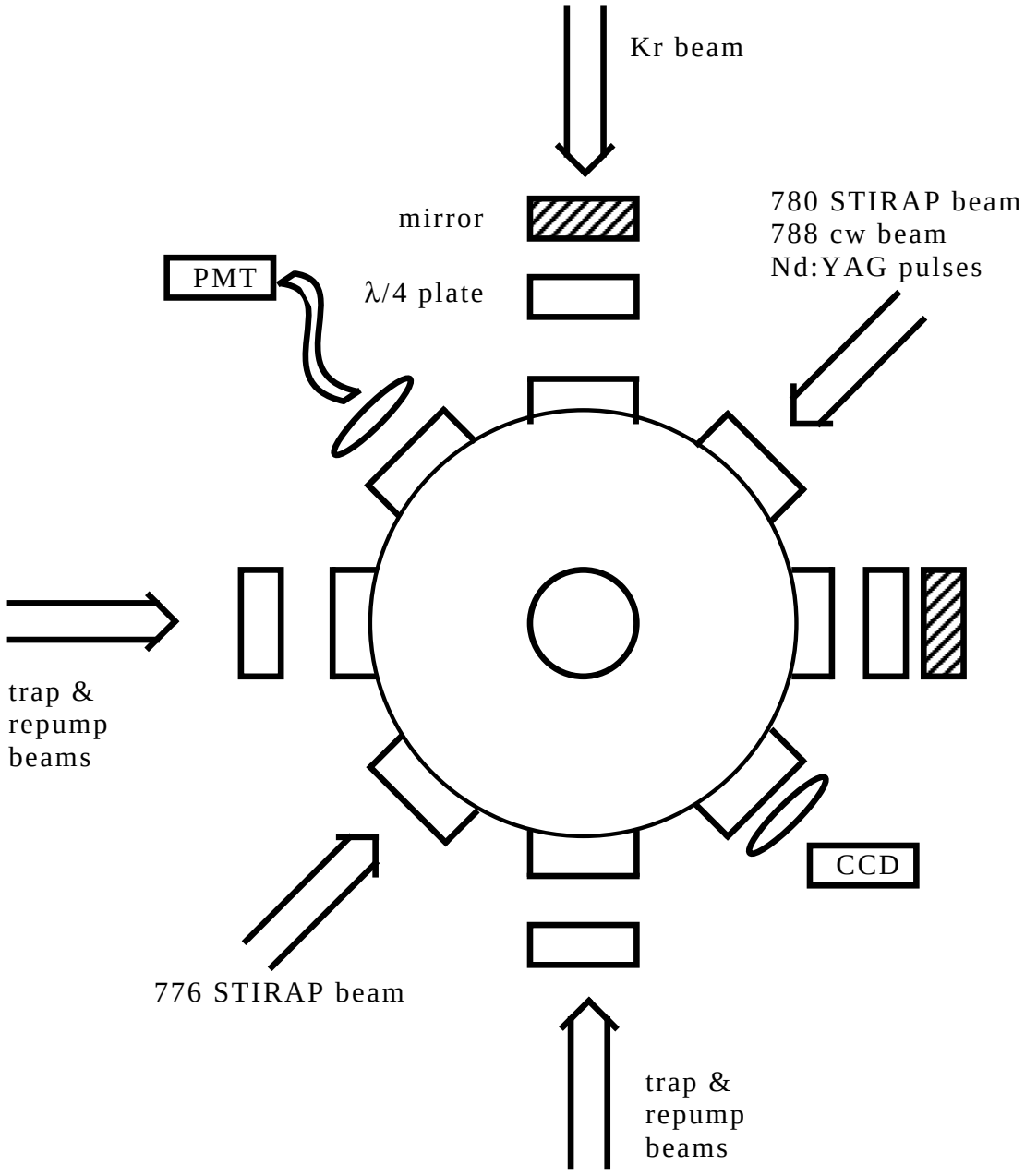

Fig. 4.13: The cell MOT. The trap and repump beams also come in and out of the page.

of a dielectric mirror serving as a retro mirror (at 780 nm) for the trap. At low intensity the power is measured before the light enters the mirror and after it exits the quarterwave plate paired with the mirror. Further 4% losses associated with near-normal incidence on each surface of the window are taken into account. A final factor is determined and used in the Igor macros used to analyze these data. During the experiment the power for the Kr laser is measured before the mirror, using a 1000:1 attenuator. The power of the Kr beam is controlled at its laser's control panel, adjusting the current applied to the plasma tube. The 788 nm beam (from the diode) is focused and sent into a beam-splitting polarizing cube in the beam path of the 780 nm STIRAP beam. The two beams thus copropagate to the trap with perpendicular linear polarizations. The 788 nm beam's power is attenuated by a halfwave plate set before the cube. To control the Nd:YAG's beam path we use mirrors which are specially coated for its wavelengths and dichroic beamsplitters which reflect these wavelengths while allowing wavelengths near 780 nm to pass. A mirror is placed in the beam path, deflecting it to a dichroic beamsplitter in the path of the 780 nm STIRAP beam. This beamsplitter has to be appropriate for the particular Nd:YAG wavelength being used at the time. The fluence of the pulses is adjusted using a polarizer and halfwave plate. Typical 1/e radii for the ionizing beams are 1.25 mm for the 1064 nm, 750 μm for the 532 nm, 450 μm for the 647 nm, and 380 μm for the 788 nm. The beam profiles are measured by a photodiode with a pinhole before it (the diode and the Kr laser) or by a power meter with a razor blade before it, the pinhole and razor blade each mounted on a precision translation stage. These radii compare with the average 450 μm 1/e radii of the STIRAP beams and contrast with the 100 to 130 μm 1/e radii of the cloud of trapped atoms (somewhat smaller than during the STIRAP experiment). The cloud then experiences a near-uniform spatial intensity of STIRAP and ionizing light.

Initially the high-power STIRAP diodes had no optical isolators. This proved to be a problem in this experiment, in particular for the 776 nm diode, where feedback (perhaps from the face of the AOM crystal or lens) created noise. This was solved by moving one isolator from the injection path and placing it in the 776's path to the experiment. The injection light is now sent into the polarizing beam-splitting cube on the side of the isolator away from the diode, through the face perpendicular to the high-power beam path (see Fig. 4.14). It then has the appropriate polarization to reach the diode. Consider high-power light coming back through the system. The outer PBS cube allows only a certain linear polarization to pass, which happens to be orthogonal to the polarization of the injection-locking beam. As the feedback and the injection beam go through the Faraday isolator, they are rotated 45deg. Upon exiting, the feedback is (nearly) extinguished by the inner PBS cube, but the injection beam has the correct polarization to pass through.

4.4 Theoretical Calculations

The theoretical calculations for this experiment were performed by Hossein Sadeghpour of the Institute for Theoretical Atomic and Molecular Physics (ITAMP). The reader interested in the details is referred to Ref. [55]; a simple epitome is presented here.

The calculations are based on the valence-electron parametric potential method performed in the central field approximation, that is, the valence electron motion is considered in the presence of a "frozen" core. This potential has the form:

$$V_\ell(r) = \frac{Z_\ell(r)}{r} - \frac{\alpha_d}{2r^4}[1 - e^{(-r/r_c^{(\ell)})^6}], \tag{4.21}$$

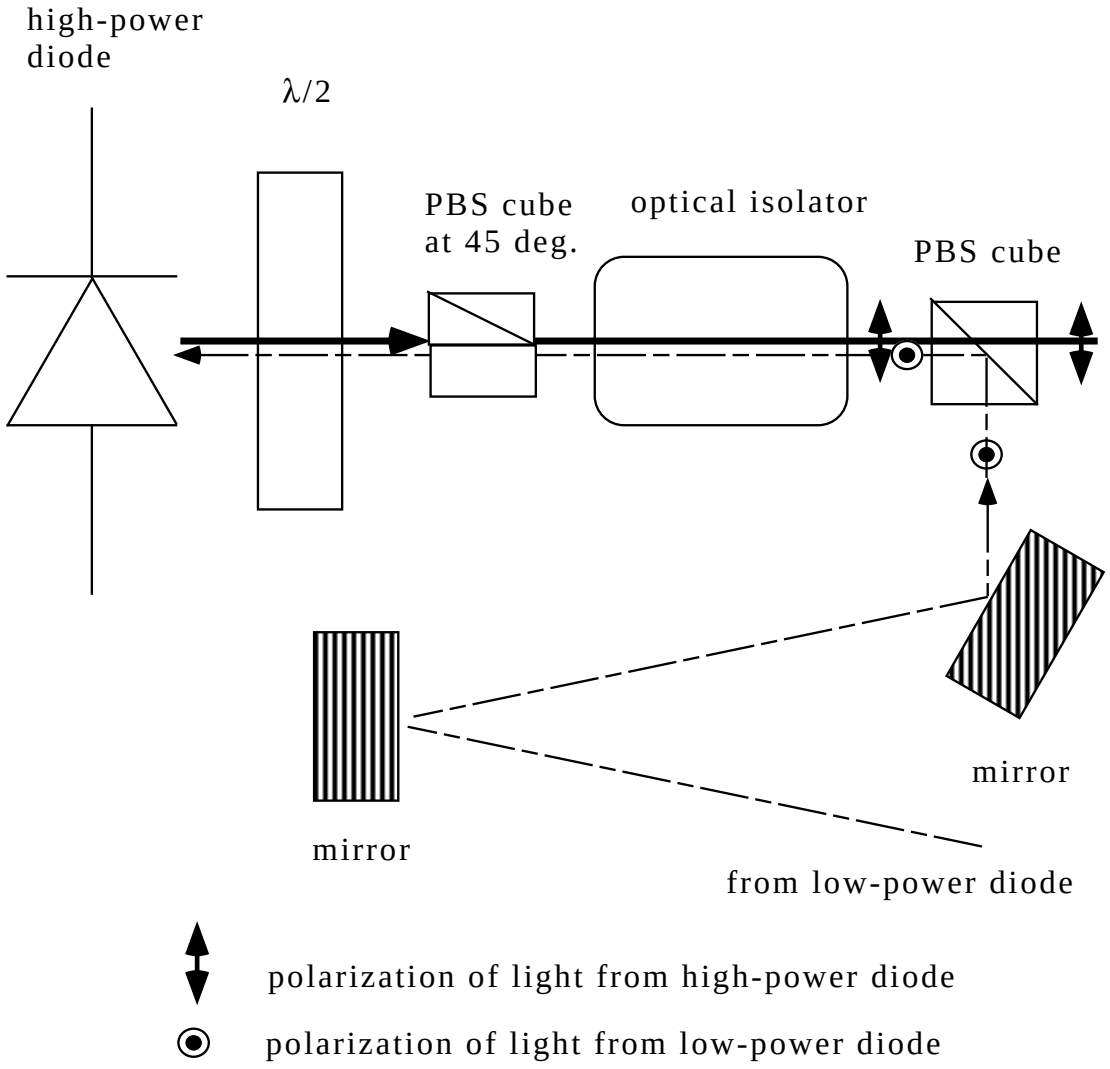

Fig. 4.14: The new arrangement of the optical isolator for the high-power 776 nm diode.

where α_d is the static dipole polarizability of the ionic core and the effective radial charge $Z_\ell(r)$ is given by

$$Z_\ell(r) = 1 + (z-1)e^{-a_1(\ell)r} + r(a_3^{(\ell)} + a_4^{(\ell)}r)e^{-a_2^{(\ell)}r}. \tag{4.22}$$

In Eqn. 4.22 z is the nuclear charge (z = 37 for Rb). The cutoff radius $r_c^{(\ell)}$ prevents application of Eqn. 4.21 near the nucleus, where it becomes unphysical. The cutoff radius and the effective radial charge are determined through a nonlinear fit to one-electron Rydberg energy levels. The partial PI cross section is proportional to the squared norm of the matrix element of the first-rank irreducible dipole tensor $r_q^{(1)}$ acting between the initial and final (continuum) states. The eigenstates are expanded over the fine-structure coupled states, eventually yielding an energy-normalized reduced radial matrix element connecting the intial state to the final state at the photoelectron energy. The initial state in this experiment is

$$|n\ell jIF''M''\rangle = |5D\frac{5}{2}\frac{5}{2}5M''\rangle, \tag{4.23}$$

where the population is assumed to be equally distributed between the m_F levels $M'' = -3$ to $+3$. We assume this because the atoms are promoted to the 5D from the 5S by linearly polarized STIRAP beams, and we assume equal population distribution in the MOT ground state ($5S_{1/2}$, F=3, $M = -3$ to $+3$). (Were the 5D assumed to be distributed among all m_F levels [i.e., $M'' = -5$ to $+5$], the calculated cross sections would be somewhat larger; see Table 4.2.) The theory employed here gives results comparable to previous calculations for Rb(5D), e.g., Ref. [65]. Furthermore, as a check it was applied to the results of Ref. [6] for $Rb(5P_{3/2})$.

4.5 Results

The final results of the experiment and calculations are presented in Fig. 4.15. The data points for 788 nm and 647 nm have been reduced by the contribution of

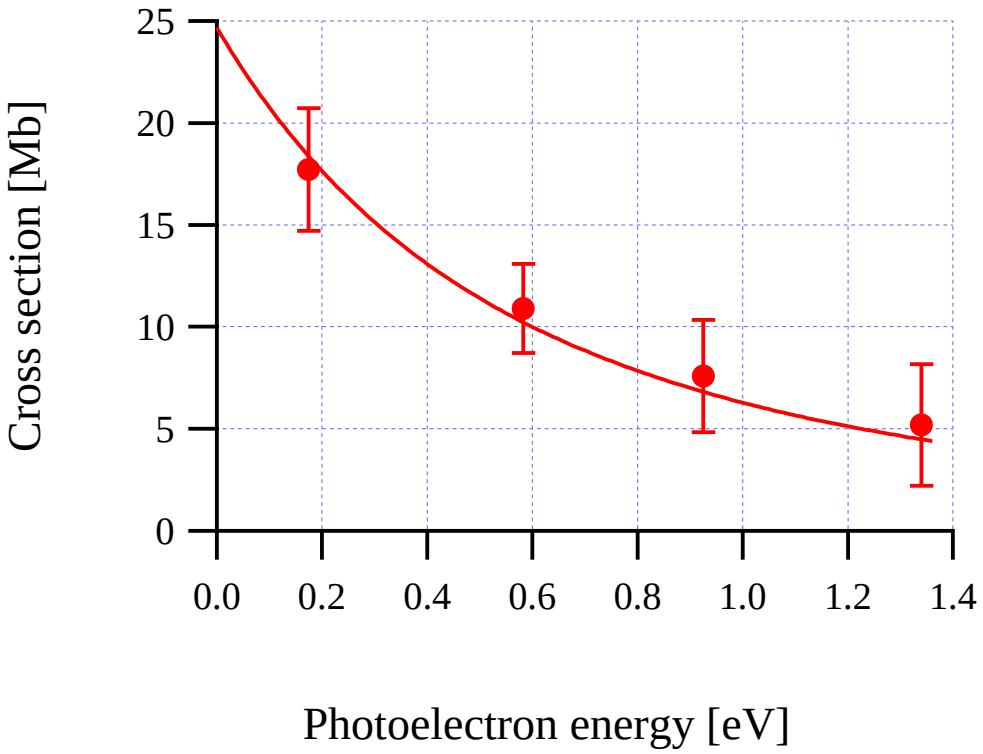

Fig. 4.15: The $5D_{5/2}$ PI cross section versus photon energy above threshold. Left to right, the data points represent the measured cross sections at 1064, 788, 647 and 532 nm. The curve is the theoretical prediction as described in the text.

Table 4.2: Measured and calculated $5D_{5/2}$ photoionization cross sections. The starred cross section is the theoretical prediction if all 11 $5D_{5/2}m_F$ levels were populated.

wavelength [nm]	σ_{exp}[Mb]	σ_{th}[Mb]	σ^*_{th}[Mb]
1064	17.7	18.4	32.13
788	10.9	10.2	17.42
647	7.6	6.83	11.72
532	5.2	4.48	7.734

ionization out of the 6P state. The calculated cross sections have been restricted to the seven m_F levels $M'' = -3$ to $+3$. The uncertainty bars primarily reflect the standard deviation of several experimental runs (typically five) for each photoionizing wavelength. The linearly polarized STIRAP beams were usually at a relative angle of 30°. Changing this angle from 0° to 90° produced a $< 10\%$ effect in trap loss. Changing the polarization of the PI radiation relative to the STIRAP beams from parallel to perpendicular produced a $< 15\%$ effect (refer to Fig. 4.16). While noticeable these polarization effects are not statistically significant when compared to our uncertainties.

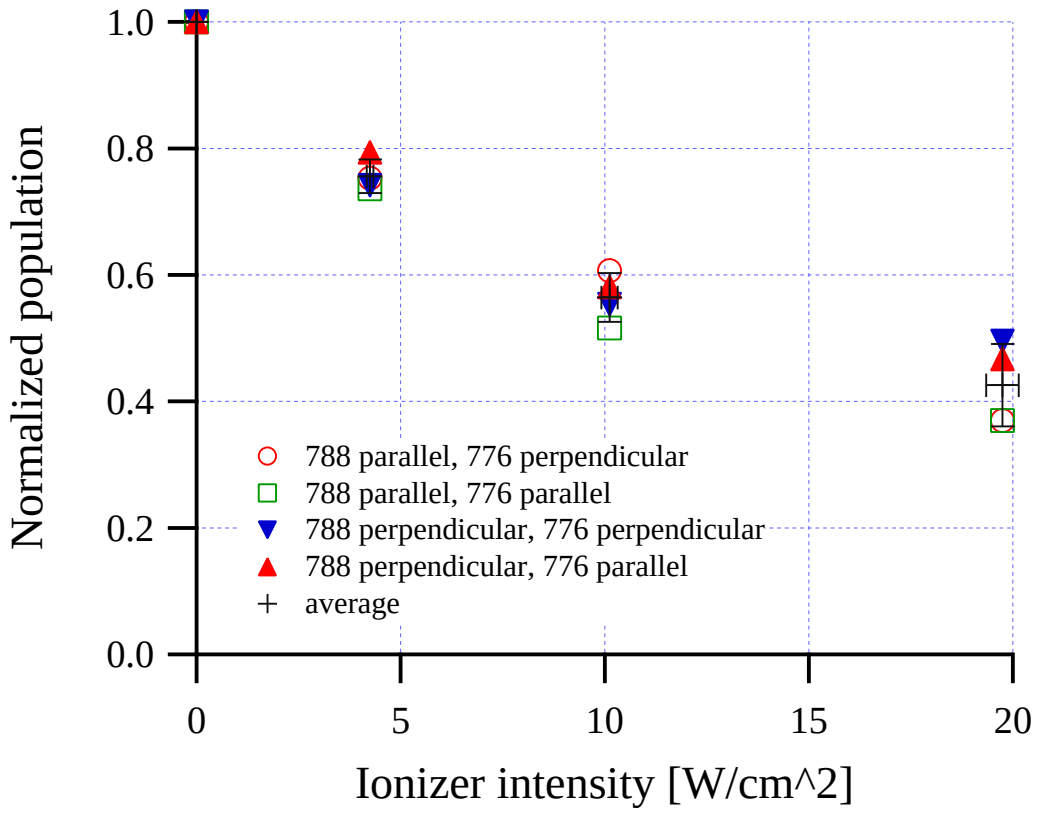

Fig. 4.16: The effect of various combinations of linear polarization (with respect to the 780 nm STIRAP beam) of the 776 nm STIRAP beam and the 788 nm ionizing beam as a function of ionizing light intensity.

Chapter 5

Collisions

5.1 Introduction and Theory

With their relatively simple structure of one valence electron and an atomic core, alkali atoms are a favorite subject for a variety of investigations, including collisions between atoms. Calculation of collisional cross sections are easier for these atoms than for more complex systems. Collisions between alkalis have been studied both theoretically (e.g. [66–68]) and experimentally, including Cs [69,70], Na [71,72] and Rb [8,9,73]. Some of these experiments were conducted in ovens where the temperature exceeded 400 K. Others were conducted in magneto-optical traps (T$\leq$ 1 mK) or in Bose-Einstein condensates (T$\leq$10 nK). Due to the low kinetic energy of the colliding atoms in the cold experiments, weak long-range interatomic forces are important. Furthermore, the collisions occur over long times and thus the atoms are sensitive to spontaneous emission. In an inelastic collision the energy transfer between two atoms may cause one or both to be lost to the trap. Thus the effect of collisional processes are made manifest in the trap fluorescence level. Most of the experiments cited above involve the ground state and the first excited state, although a few involve fine-structure changing collisions of higher-lying levels [74–76]. There have also been experiments involving more than one species (for example [77]). This is to be the first attempt at measuring the Rb 5S-5D cross section for cold atoms.

These collisions provide an interesting contrast to 5S-5P collisions. In the latter the predominant interaction is very long range (R^{-3}), and the relatively short radiative lifetime τ_{5P} (27 ns) makes spontaneous decay important [7]. By comparison the 5S-5D interaction is shorter range (R^{-5} and R^{-6}; see below), and the lifetime τ_{5D} of 241 ns means that spontaneous emission is not important. Experiments involving the 5D are quite challenging. If one increases the intensity of the laser light driving the lower transition (780 nm), the trap will be perturbed, even at the 47 MHz blue detuning at which this experiment is run. The chief contributor to photoionization (PI) is the light driving the upper transition (776 nm), because its intensity is much greater than that driving the lower transition. Increasing the 776 nm beam's intensity increases PI, and this could dwarf trap loss due to collisions. Since we know the 5D PI cross section at various wavelengths, we can now account for the contribution of photoionization to the total trap loss rate, but this does not allow us to increase the 776 nm intensity arbitrarily. The chief remaining loss mechanism is 5S-5D collisions. In this experiment we had hoped to determine the cross section for collisions between 5S and 5D atoms via trap loss measurements. Unfortunately, we were disappointed in this hope.

The likelihood of trapped atoms interacting with one another increases with number density. One interaction is the re-absorption of photons emitted by a neighboring atom, which results in a net repulsive force. While the trap loads, the atoms repel each other. Initially the number density varies linearly with the number of atoms in the trap; however, if the trap is in the collective regime, it quickly reaches a state where the number density remains constant [56]. In this situation as more atoms are added to the trap, the trap grows in size. The time rate of change of the number of atoms trapped is given by

$$\dot{N} = L - \Gamma N - \beta n N \tag{5.1}$$

where L is the loading rate, Γ is the loss rate due to collisions with background gases, and β is the trap loss collisional rate constant due to collisions with other cold rubidium atoms. If a trap is in the collective regime, its number density n is constant, making the solution to Eqn. 5.1 a simple exponential.

We want to identify the contribution to trap loss due to collisions involving atoms in the 5D state. To that end we separate the rate β_{5D} from the trap-laser induced rate β_t. Since it usually is a good idea to have some notion of the order of magnitude of the parameter one is trying to measure, let us consider an analogous experiment. From Fig. 1(a) in [78] for ^{85}Rb we find β_t of about 1-2 $\times 10^{-12}$ cm^3 s^{-1} for a detuning Δ of about -1 to -2 Γ and I_t of 12 mW/cm^2 (in that measurement the beam size was 6.3 mm e^{-2} diameter and the magnetic field gradient dB_z/dz was 4.8 G/cm). Combining this value of β with our density, we obtain a trap-laser-induced collision rate $\beta_t n$ of 3 to 6 $\times 10^{-2}$ s^{-1}, which is less than 10% of our typical total loss rate. This implies that our loss rate is usually dominated by collisions with background gas.

Now let us see what theory predicts, beginning with the long-range coefficients. At long-range, the lowest order interaction terms between an S-state atom and a D-state atom are $-C_5/R^5$ and $-C_6/R^6$, where R is the internuclear separation. Marinescu and Dalgarno [67] give $C_5 = 0.5079$ and $C_6 = 13.68 \times 10^4$ in atomic units for a Rb 5S-5D collision. We determine the range within which C_6 dominates by setting:

$$\frac{C_5}{R^5} = \frac{C_6}{R^6} \tag{5.2}$$

$$R = \frac{C_6}{C_5} = 2.69 \times 10^5 \text{ a.u.} = 14.2\ \mu\text{m}. \tag{5.3}$$

Thus it seems we need concern ourselves only with the C_6 contribution. We shall try four different estimates for the impact parameter [79]. In the first approach

we consider an initially stationary atom at R_0 accelerated by a potential $U = -C_n/R^n$. With K as the kinetic energy and E_0 as the total energy we have at R_0:

$$E_0 = U_0 = -\frac{C_n}{R_0^n} \tag{5.4}$$

$$K = E_0 - U = C_n \left(R^{-n} - R_0^{-n}\right) \tag{5.5}$$

$$-\dot{R} = \sqrt{\frac{2C_n}{\mu}}\,\sqrt{R^{-n} - R_0^{-n}}, \tag{5.6}$$

where we have taken $K = (1/2)\mu v^2$ and set $\dot{R} = v$, where μ is the reduced mass and v is the relative velocity. Rearranging terms and integrating we obtain:

$$-\sqrt{\frac{2C_n}{\mu}}\int_{R_0}^{R} \frac{dR'}{\sqrt{R'^{-n} - R_0^{-n}}} = \int_0^t dt' = t. \tag{5.7}$$

Since inelastic processes generally occur at short range ($R \ll R_0$), we can replace the upper integration limit with $R = 0$, and calculate the time t it takes for the two atoms to come together. By the transformation of variables $y = R'/R_0$ we see:

$$t = \sqrt{\frac{\mu}{2C_n}}\int_0^1 \frac{R_0\,dy}{\left\{R_0^{-n}\left[\left(\frac{R'}{R_0}\right)^{-n} - 1\right]\right\}^{1/2}} \tag{5.8}$$

$$t = \sqrt{\frac{\mu}{2C_n}}\,\frac{R_0}{R_0^{-n/2}}\int_0^1 \frac{dy}{\sqrt{y^{-n} - 1}}\,. \tag{5.9}$$

Factoring and performing another transformation of variables ($x = y^n$) yields:

$$t = \sqrt{\frac{\mu}{2C_n}}\,R_0^{(2+n)/2}\int_0^1 \frac{x^{(1/2)}\,\frac{1}{n}\,x^{(\frac{1}{n}-1)}\,dx}{(1-x)^{1/2}} \tag{5.10}$$

$$t = \sqrt{\frac{\mu R^{(n+2)}}{2C_n}}\,\frac{1}{n}\int_0^1 \frac{x^{(\frac{1}{n}-\frac{1}{2})}\,dx}{(1-x)^{1/2}}. \tag{5.11}$$

The integral is of the form [80]:

$$\int_0^1 x^{\mu-1}\left(1 - x^{\lambda}\right)^{\nu-1} dx = \frac{1}{\lambda}\,B\left(\frac{\mu}{\lambda}, \nu\right), \tag{5.12}$$

where B is the beta function. The beta and gamma functions have these relationships:

$$B(x,y) = \frac{\Gamma(x)\Gamma(y)}{\Gamma(x+y)} \tag{5.13}$$

$$\Gamma(z) = \frac{1}{z}\,\Gamma(z+1). \tag{5.14}$$

Using the aforementioned relationships and evaluating $\Gamma(1/2)$, we obtain for the parameters of this analysis:

$$B\left(\frac{1}{n}+\frac{1}{2},\frac{1}{2}\right) = \frac{\Gamma(\frac{1}{n}+\frac{1}{2})\Gamma(\frac{1}{2})}{\Gamma(\frac{1}{n}+1)} \tag{5.15}$$

$$= \frac{1}{\frac{1}{n}+\frac{1}{2}}\,\frac{\Gamma(\frac{1}{n}+\frac{3}{2})\sqrt{\pi}}{\Gamma(\frac{1}{n}+1)} \tag{5.16}$$

$$= \frac{2n}{n+2}\,\sqrt{\pi}\,\frac{\Gamma(\frac{1}{n}+\frac{3}{2})}{\Gamma(\frac{1}{n}+1)}. \tag{5.17}$$

Substituting this expression into Eqn. 5.11 results in the following equation for the time it takes the atoms, starting at R_0 and accelerated by the $-C_n/R^n$ attractive potential, to reach short range:

$$t_n = \left(\frac{\mu R_0^{(n+2)}}{C_n}\right)^{1/2} \underbrace{\frac{(2\pi)^{1/2}}{n+2}\,\frac{\Gamma(\frac{1}{n}+\frac{3}{2})}{\Gamma(\frac{1}{n}+1)}}_{\alpha_n} \tag{5.18}$$

Since the 5D atom can decay, we can estimate an upper limit for R_0 by setting this collision time equal to the 5D radiative lifetime. We thus obtain an expression for the distance at which an atom can be excited and still survive to short range.

$$R_0 = \left(\frac{C_n}{\mu}\frac{t_n^2}{\alpha_n^2}\right)^{1/(n+2)}. \tag{5.19}$$

In the case of n=6, $\alpha_6 = 0.305$, $C_6 = 1.309 \times 10^{-74}$ J m^6 and the reduced mass (^{85}Rb) $\mu = 7.057 \times 10^{-26}$ kg, these values give a distance R_0 of 24.2 nm.

In the second approach we assume not an initially stationary atom but one with some kinetic energy K_0. We want to find the distance at which an atom

with some kinetic energy will be captured by the C_6/R^6 potential. A typical MOT temperature of 100 μK corresponds to an energy of 1.38 $\times 10^{-27}$ J = 3.17 $\times 10^{-10}$ a.u. Thus:

$$K_0 = C_6/R^6 \tag{5.20}$$

$$R = \left(\frac{C_6}{K_0}\right)^{1/6}. \tag{5.21}$$

This results in a distance of 14.5 nm.

The third approach is to use the location of the centrifugal barrier as the impact parameter. Including the centrifugal contribution the total potential is:

$$U = \frac{\ell^2}{2\mu R^2} - \frac{C_n}{R^n}, \tag{5.22}$$

where ℓ is the collisional angular momentum. The potential barrier is an extremum of this function:

$$\frac{dU}{dR} = 0 \Rightarrow \frac{\ell^2}{2\mu}(-2)R^{-3} - C_n(-n)R^{-n-1} = 0 \tag{5.23}$$

$$-\frac{\ell^2}{\mu}\,\frac{1}{R^3} + n\frac{C_n}{R^{n+1}} = 0 \tag{5.24}$$

$$\frac{R^{n+1}}{R^3} = n\frac{C_n}{\ell^2/\mu} \tag{5.25}$$

$$R = \left(n\,\frac{C_n}{\ell^2/\mu}\right)^{1/(n-2)}. \tag{5.26}$$

The potential at the barrier is thus:

$$U(R_0) = (\ell^2/\mu)\,\frac{1}{2}\,\left[\left(n\frac{C_n}{\ell^2/\mu}\right)^{1/(n-2)}\right]^{-2} - C_n\left[\left(n\frac{C_n}{\ell^2/\mu}\right)^{1/(n-2)}\right]^{-n} \tag{5.27}$$

$$U(R_0) = \left(n\frac{C_n}{\ell^2/\mu}\right)^{-n/(n-2)}\left[(\ell^2/\mu)\frac{1}{2}\left(n\frac{C_n}{\ell^2/\mu}\right)^{-2/(n-2)+n/(n-2)} - C_n\right] \tag{5.28}$$

$$U(R_0) = \left(n\frac{C_n}{\ell^2/\mu}\right)^{-n/(n-2)}\left[\left(\frac{n}{2}-1\right)C_n\right]. \tag{5.29}$$

We next find that value of ℓ for which $U(R_0) = K_0$:

$$\left(n\frac{C_n}{\ell^2/\mu}\right)^{-n/(n-2)}\left[\left(\frac{n}{2}-1\right)C_n\right] = K_0 \quad (5.30)$$

$$n\frac{C_n}{\ell^2/\mu} = \left[\left(\frac{K_0}{\left(\frac{n}{2}-1\right)C_n}\right)\right]^{-(n-2)/n} \quad (5.31)$$

$$\frac{\ell^2}{nC_n\mu} = \left[\frac{K_0}{\left(\frac{n}{2}-1\right)C_n}\right]^{(n-2)/n} \quad (5.32)$$

$$\ell = (nC_n\mu)^{1/2}\left[\frac{K_0}{\left(\frac{n}{2}-1\right)C_n}\right]^{(n-2)/2n}. \quad (5.33)$$

Equating R_0 with the impact parameter $\ell/(\mu v)$, where v is the velocity associated with K, we obtain:

$$R_0 = \frac{\ell}{\mu v} \quad (5.34)$$

$$R_0 = \frac{1}{v}\left(\frac{nC_n}{\mu}\right)^{1/2}\left[\frac{K}{\left(\frac{n}{2}-1\right)C_n}\right]^{(n-2)/2n}. \quad (5.35)$$

This results in $R_0 = 89.4$ nm for an atom at 100 μK, i.e., a speed of approximately 14 cm/s.

The fourth approach to estimating the impact parameter is to find that distance R which is on resonance for various detunings. The energy detuning is equated to the C_6/R^6 potential.

$$\hbar\Delta = \frac{C_6}{R^6} \Rightarrow R = \left(\frac{C_6}{\hbar\Delta}\right)^{1/6}. \quad (5.36)$$

Fig. 5.1 shows the results for detunings out past 40 MHz, highlighting certain detunings. Note how quickly R levels off.

Having estimated R, we relate it to the collisional cross section σ and the loss rate constant β thus:

$$\sigma_{5D} = \pi R^2 \quad (5.37)$$

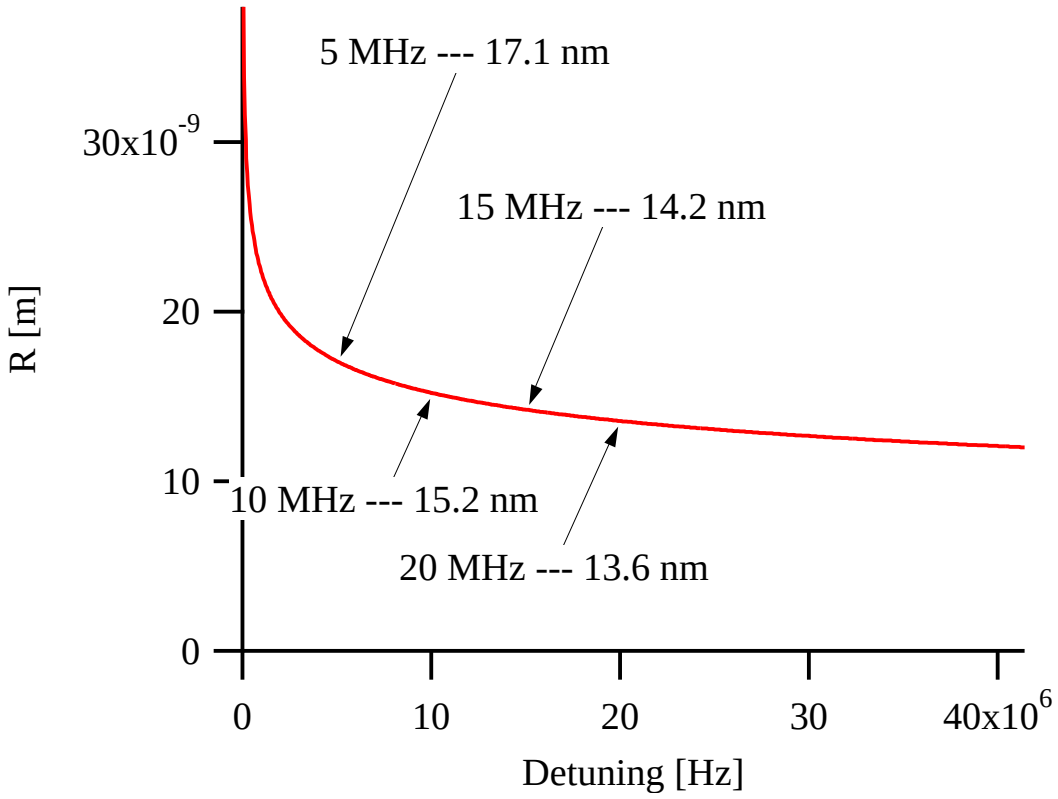

Fig. 5.1: Distance R at which an atom is on resonance with a detuned laser beam.

Table 5.1: R, σ_{5D} and β from diverse approaches.

approach	R [nm]	$\sigma_{5D}[10^{-11}\,cm^2]$	$\beta[10^{-11}\,cm^3s^{-1}]$
initially stable atom	24.2	1.84	12.9
moving atom	14.5	0.661	4.63
centrifugal barrier	89.4	25.1	176
detuning	17.1	0.92	6.45

$$\beta = \sigma_{5D}\, v. \tag{5.38}$$

The results are tabulated in Table 5.1. There are some obvious difficulties. Some of the approaches assume a moving atom (and thus an assumed temperature), one does not and the other does not depend on kinetic energy. The detuning method blows up at zero detuning. It also flattens out rather quickly, requiring that collisions will take place at nearly the same rate over a wide range of detunings. The approach using the centrifugal barrier yields an R nearly four times as large as the second largest R. This large R means that the centrifugal barrier is irrelevant, i.e., it doesn't prevent atoms from getting in close. Therefore, since the other estimates of R are fairly similar, we expect β to be in the range of $10^{-10}\mathrm{cm}^3\mathrm{s}^{-1}$. One must account for the fraction of time that an atom spends in the 5D. These estimates assume that every atom pair is 5S-5D, so the excited state fraction is taken to be 0.5. The numbers for β reported in Table 5.1 reflect this. The experimental determination of the excited state fraction is discussed near the end of the chapter. The estimates also assume that an inelastic process *always* occurs at short range.

The potential curves presented in Fig. 5.2 are calculated by Olivier Dulieu [81] based on [67]. The curves graphically portray the complicated situation at short interatomic separation. The LeRoy radius (here about 2.5 nm) designates the

boundary between the long-range region where all atoms interact principally through the classical physics of independent charge distributions, and the shorter-range region where electron exchange energies take over [82,83]. Among short range processes are fine-structure changing collisions (e.g., see [70]). An atom entering on a $5D_{5/2}$ curve and undergoing a fine-structure changing collision will exit on a $5D_{3/2}$ curve, an energy difference of 2.96 cm^{-1}. Another short-range process is reverse energy pooling, where a 5S-5D pair becomes a 5P-5P pair:

$$5S + 5D \rightarrow 5P + 5P + \mathcal{E}, \tag{5.39}$$

where the energy acquired $\mathcal{E}$ is 66 cm^{-1}. The energies acquired in these processes are sufficient to expel one or both atoms from the trap.

Let us now deal with experimental concerns, in particular how various measurements may be interpreted with regard to a collisional cross section or the collisional loss rate. As has been the case in the other parts of this series of experiments, the steady-state behavior of the trap will be the principal signal. Assuming that the trap is in the constant density regime, we first note that in the absence of the 5D excitation beams Eqn. 5.1 has the following solution for the number of atoms in the trap:

$$N_0 = \frac{L}{\Gamma_b + \beta_l n}, \tag{5.40}$$

where L is the trap loading rate and Γ_b the loss rate due to collisions with background (untrapped) atoms. Let Γ_0 be the total loss rate in the absence of 5D excitation and Γ_{5D} be the loss rate contribution due to 5D excitation. Then, using Eqn. 5.40,

$$\Gamma_0 = \Gamma_b + \beta_l n \tag{5.41}$$

$$N_0 = \frac{L}{\Gamma_0} \tag{5.42}$$

$$N_{5D} = \frac{L}{\Gamma_0 + \Gamma_{5D}} = \frac{\frac{L}{\Gamma_0}}{1 + \frac{\Gamma_{5D}}{\Gamma_0}} \tag{5.43}$$

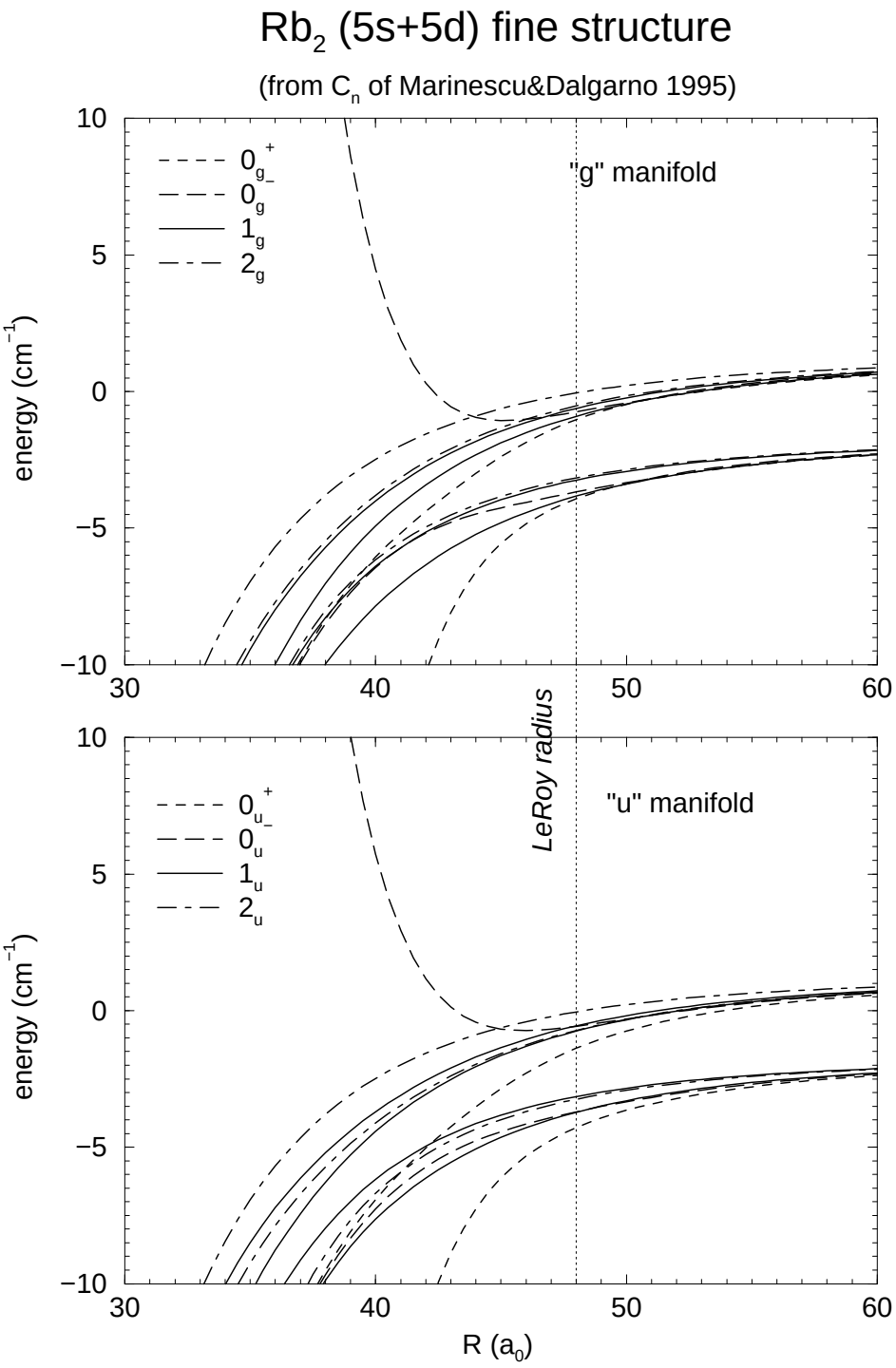

Fig. 5.2: Rb_2 5S + 5D fine structure.

$$N_{5D} = \frac{N_0}{1 + \frac{\Gamma_{5D}}{\Gamma_0}}. \tag{5.44}$$

Dividing both sides by N_0 and inverting one obtains

$$\frac{N_{5D}}{N_0} = \frac{1}{1 + \frac{\Gamma_{5D}}{\Gamma_0}} \tag{5.45}$$

$$1 + \frac{\Gamma_{5D}}{\Gamma_0} = \frac{1}{\frac{N_{5D}}{N_0}}. \tag{5.46}$$

Subtracting 1 from both sides, multiplying through by Γ_0 and getting a common denominator on the right hand side yields

$$\Gamma_{5D} = \Gamma_0 \left(\frac{1 - \frac{N_{5D}}{N_0}}{\frac{N_{5D}}{N_0}} \right). \tag{5.47}$$

This rate includes contributions from photoionization. To isolate the collisional contribution, we run the experiment at high and low densities, denoted by subscript H and L, respectively, thus obtaining

$$\Gamma_{5D,H} = \Gamma_{PI} + \beta_{5D} n_{5D,H} \tag{5.48}$$

$$\Gamma_{5D,L} = \Gamma_{PI} + \beta_{5D} n_{5D,L} \tag{5.49}$$

$$\Gamma_{5D,H} - \Gamma_{5D,L} = \beta_{5D} \left(n_{5D,H} - n_{5D,L} \right) \tag{5.50}$$

$$\beta_{5D} = \frac{\Gamma_{5D,H} - \Gamma_{5D,L}}{n_{5D,H} - n_{5D,L}}. \tag{5.51}$$

The density of the atomic cloud is changed by changing the detuning of the trap laser (e.g., from $\sim$ 12 MHz to $\sim$ 6 MHz). This also necessitates calculating the excited state fraction appropriate for each condition, and this is accounted for in the Igor macros used to analyze the data (see Appendix C.3). Other techniques for changing the density (e.g., changing the magnetic field gradient) were considered and rejected because they also changed other trap characteristics. For both high and low densities the trap characteristics are measured in the presence and absence of 5D excitation, yielding for each of these four combinations a loading rate, the number of atoms in the trap and the number density. From the first two one calculates Γ_{5D}, and with the latter one extracts β_{5D}.

5.2 Determination of Density Regime

As mentioned in Chapter 4, Melanie Kittle's summer research project determined that this MOT usually operates in the collective regime (Fig. 5.3). In order to make that determination, with both a PMT and a CCD camera we observe the trap as it loads. Using a TestPoint program written by Matthew Wright and a LabView program written by this author, we capture images of the trap as it loads and compare them to a loading curve. The images are captured at a rate of about seven/second over four to six seconds. In addition to grabbing the frames, Wright's program analyzes each image, giving the magnitude of the background, the peak magnitude of the trap, Gaussian fits in the x and y directions and standard deviations of these. The LabView program captures the trap fluorescence level from the PMT via the current-to-voltage amplifier as the trap loads.

One function generator puts out a square wave with a period of 12 to 16 seconds. This signal serves two functions: (1) to turn on the anti-Helmholtz coils and hence start the trap loading; and (2) to gate a second function generator. This second generator when gated puts out a train of TTL pulses which enables the TestPoint program to grab a frame. After the program is triggered, it grabs the next frame which the CCD presents, which happens within 34 ms. Refer to Fig. 5.4 for a schematic of this system.

From the amplitudes, the x and y Gaussian radii and the PMT loading curves, the volume, number and number density are calculated as a function of time. Note in Fig. 5.5 that the number continues to grow as the number density remains constant; this is a characteristic signature of the collective regime. We conclude that this MOT operates in the collective regime with a number density of about 3×10^{10} cm^{-3} and contains 3 to 5 $\times 10^5$ atoms. Individual runs exhibited different

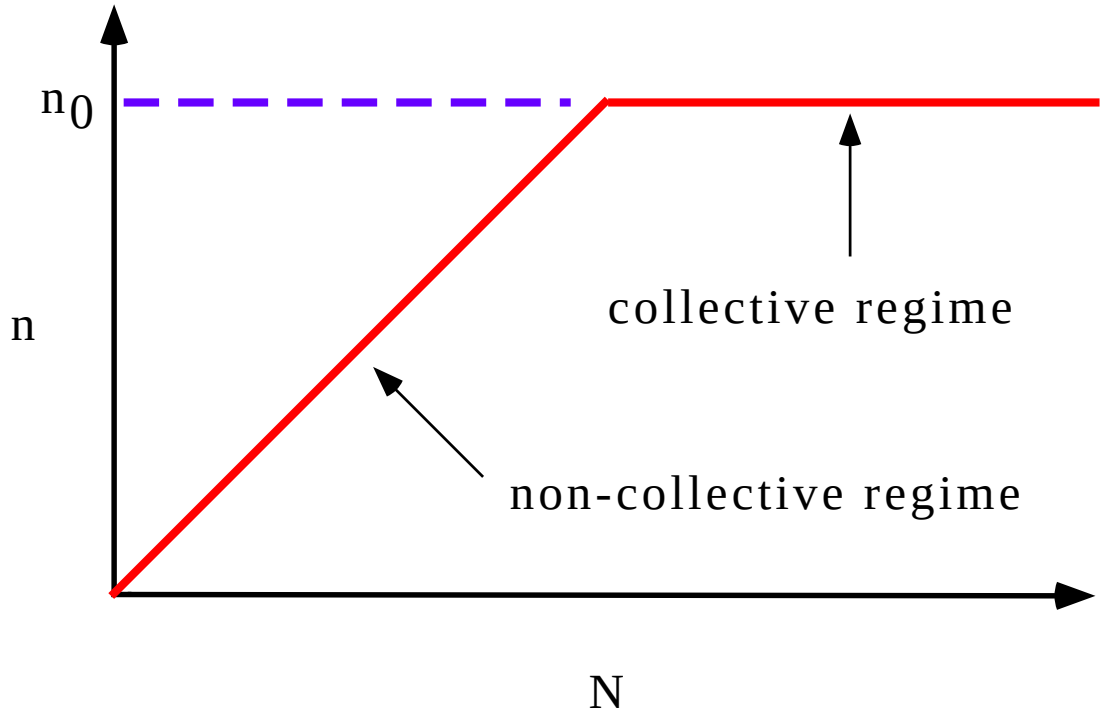

Fig. 5.3: Number density vs. number of atoms in the trap. As a trap loads, it can be in one of two possible regimes: the non-collective and the collective. In the non-collective regime the number density increases proportional to the number. The number density then levels off to a constant, n_0. This is the collective regime. The number increases while the density remains constant, in distinction to the non-collective regime, where both the number and the density are increasing.

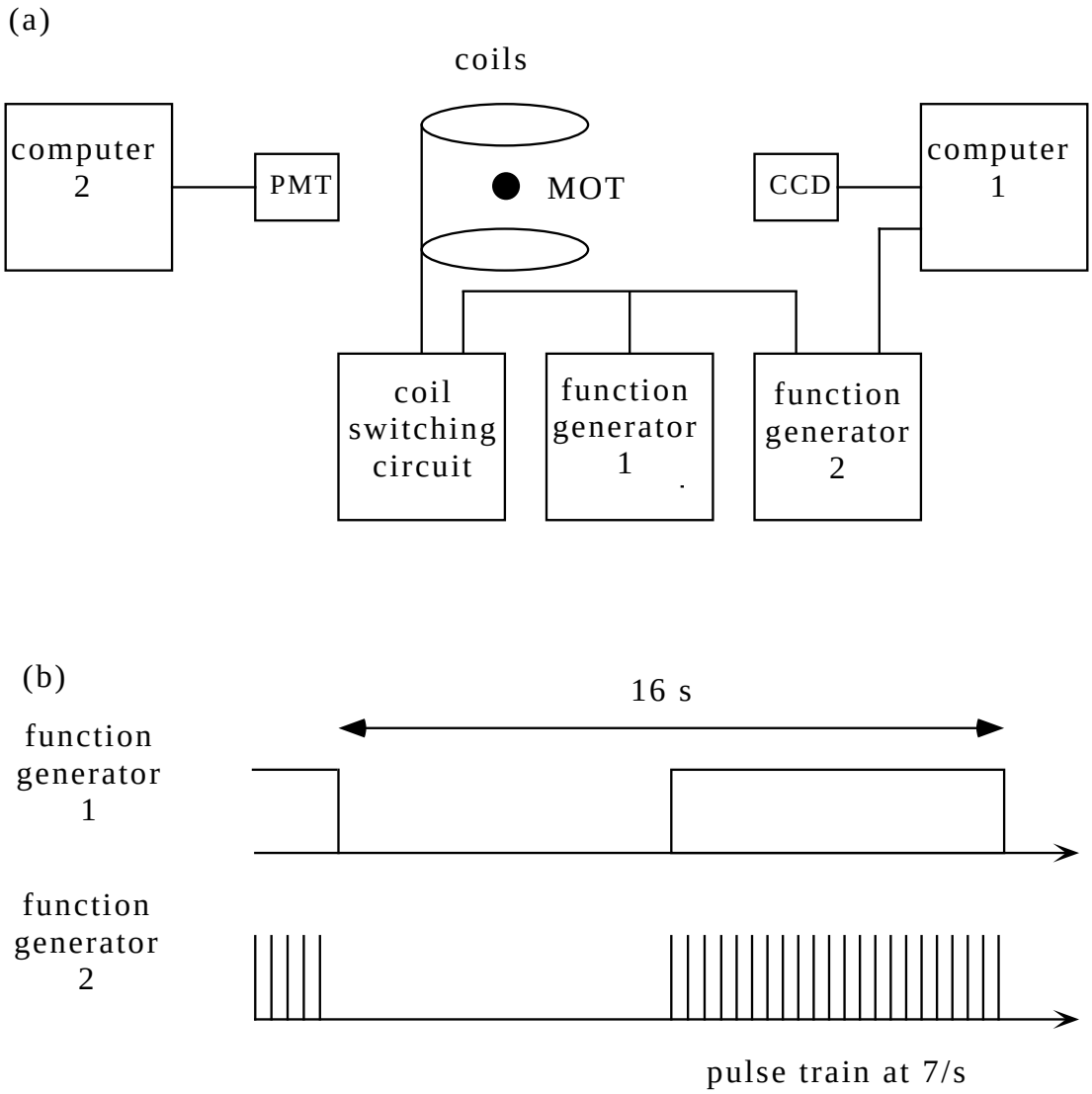

Fig. 5.4: Part (a): A schematic of the apparatus used in Melanie Kittle's measurements of trap density. Part (b): The timing relationship between function generators. The first function generator produces a square wave with a period of 16 s. This both switches the antiHelmholtz coils on and off (and thus too the trap) and gates the second function generator. The latter controls the capturing of trap images taken by a CCD.

behavior near these values.

5.3 Set-up and Technique

No new apparatus is required for this experiment. A Berkeley Nucleonics Corporation 555 Series Pulse/Delay Generator replaces the combination of the Hewlett Packard 8082A Pulse Generator and the Stanford Research Systems Model DG535 Pulse/Delay Generator. We are able to do this because the need for nanosecond timing control is no longer necessary, as will be described below. The repump laser is on continuously for this experiment. The trap laser is on for 17 μs out of a total period of 20 μs (duty cycle of 85%). The six-beam total intensity I_t of the trap laser is 12 mW/cm^2, red detuned about 10 MHz ($\Delta = -1.7\Gamma$). The full width, half maximum size of the trap laser beams is 5 mm by 4 mm. The trap typically loads at a rate of 0.7 s^{-1}, determined from loading curves. The number density is about 3 $\times 10^{10}$ cm^{-3}. The magnetic field gradient is about 23 G/cm. The 776 nm and 780 nm pulses are no longer near-Gaussian pulses of tens of ns but rather "quasi-continuous" near-rectangular pulses of 2 μs duration and are coterminous in time. In order to reduce photoionization effects caused by the excitation beams, their intensities are attenuated. The intensity of the "high power" 780 nm light is reduced to a level where a pulse of this duration has no appreciable effect on the trap. The "high power" 776 nm light is also reduced but not as greatly as the 780. The fields are no longer intense enough to drive the population transfer adiabatically; thus, this is not a STIRAP experiment.

The relevant signal is the trap fluorescence at 780 nm, captured by a PMT in the same manner as in the earlier experiments. Likewise, LabView programs control the experiment and data collection. In the early stages of the experiment the 776 laser was swept slowly back and forth some tens of MHz around resonance (refer to Fig. 5.6). This was accomplished with a function generator set to a long

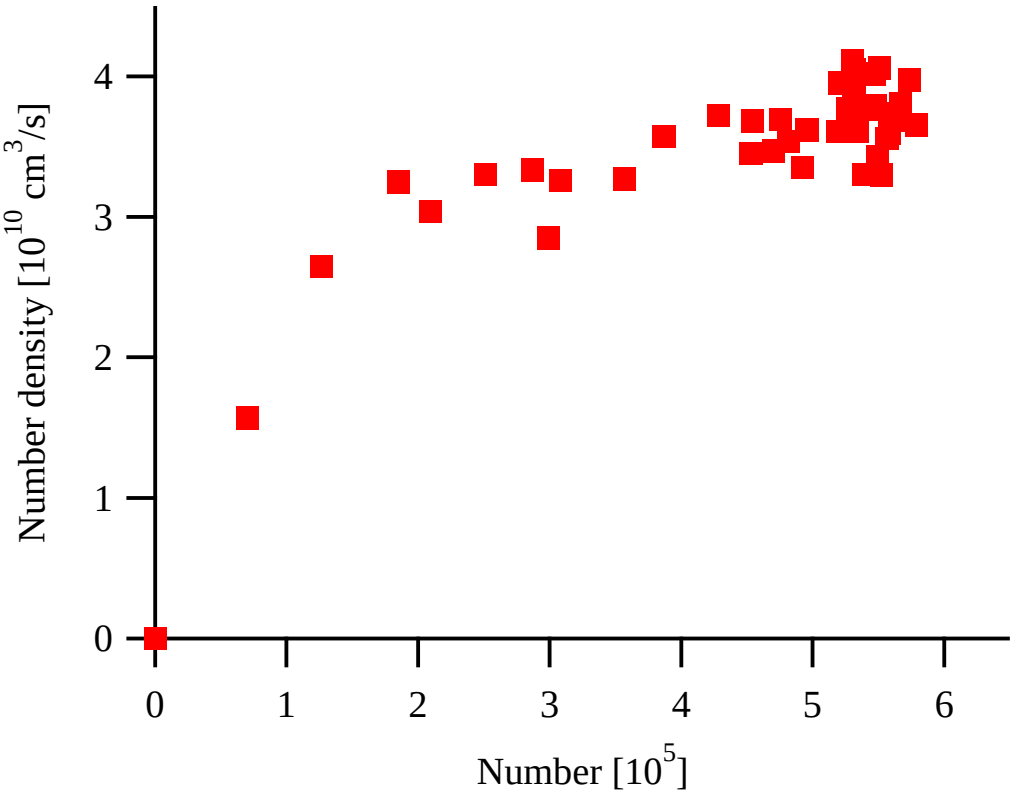

Fig. 5.5: Trap number density vs number of atoms. The peak number of atoms is about 5 $\times 10^5$. In the constant density regime the number could be calculated from the volume: $N = n_c \pi^{3/2} w_x w_y w_z$, where w_i are the radii of the trap. In this experiment the number is determined via the trap fluorescence as acquired by the PMT.

period (roughly a minute), driving the PZT of the EOSI 776 nm low-power laser. Unfortunately, the function generator cannot provide a smooth, steadily-changing signal at the period and amplitude required. Furthermore, the PZT itself exhibits hysteresis. Thus there is some uncertainty in the laser's frequency. To reduce this uncertainty we instead lock the 776 nm laser to resonance and tune its AOM to the desired frequency (as measured by a Tektronics 2712 RF Spectrum Analyzer). The detuning from two-photon resonance is related to the AOM frequency by: Δ = 80 MHz - ν_{AOM}. The limitations here are that the frequencies must be chosen one at time, and that the AOM and its driver are somewhat restricted in the range of attainable frequencies. As the frequency is changed, the angle at which the first-order beam exits the AOM changes slightly, so that for each new frequency the 776 nm beam is realigned. After each detuning the power level of the beam is checked and readjusted if necessary to ensure that the power is the same for every run.

5.4 Results

As mentioned in the beginning of the chapter the results of this experiment are disappointing. Consider these data from 2001.06.19 shown in Fig 5.7. This run should have produced a good result. Although the number of trapped atoms is rather low, the factor of two difference between the high and low density regimes should have given a clear indication of a density-dependent effect. The power of the 776 nm beam is about 0.7 mW (an intensity of about 106 mW/cm^2) and of the 780 nm beam about 0.1 mW ($\sim$ 6 mW/cm^2). The number density in the high density trap is about twice that of the low density trap. The loading rate data do not exhibit monotonic behavior. The rate gradually decreases as the 776 nm light is moved further from two-photon resonance, but at Δ = -20 MHz the high density loading rate shoots up. The higher density trap contains very roughly 50% more atoms until Δ = -20 MHz.

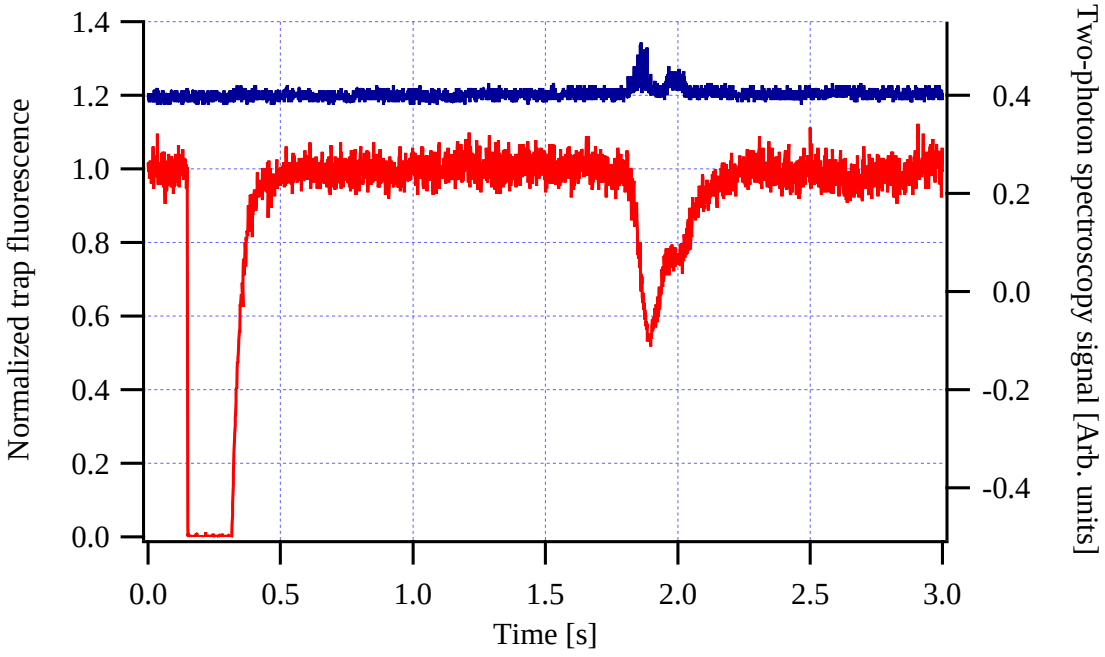

Fig. 5.6: Effect on the trap of sweeping (red to blue) the 776 nm laser. The upper trace is of the two-photon spectroscopy. The two peaks are for the F'=4 $\rightarrow$ F"=5 and F"=4 transitions, left to right. The splitting is about 9.5 MHz, and can also be detected in the lower trace, which is of the trap fluorescence. When the excitation beams are on two-photon resonance, the trap loses about 55% of its atoms. In this case most of the loss is due to photoionization. Also note that there is no structure further to the red.

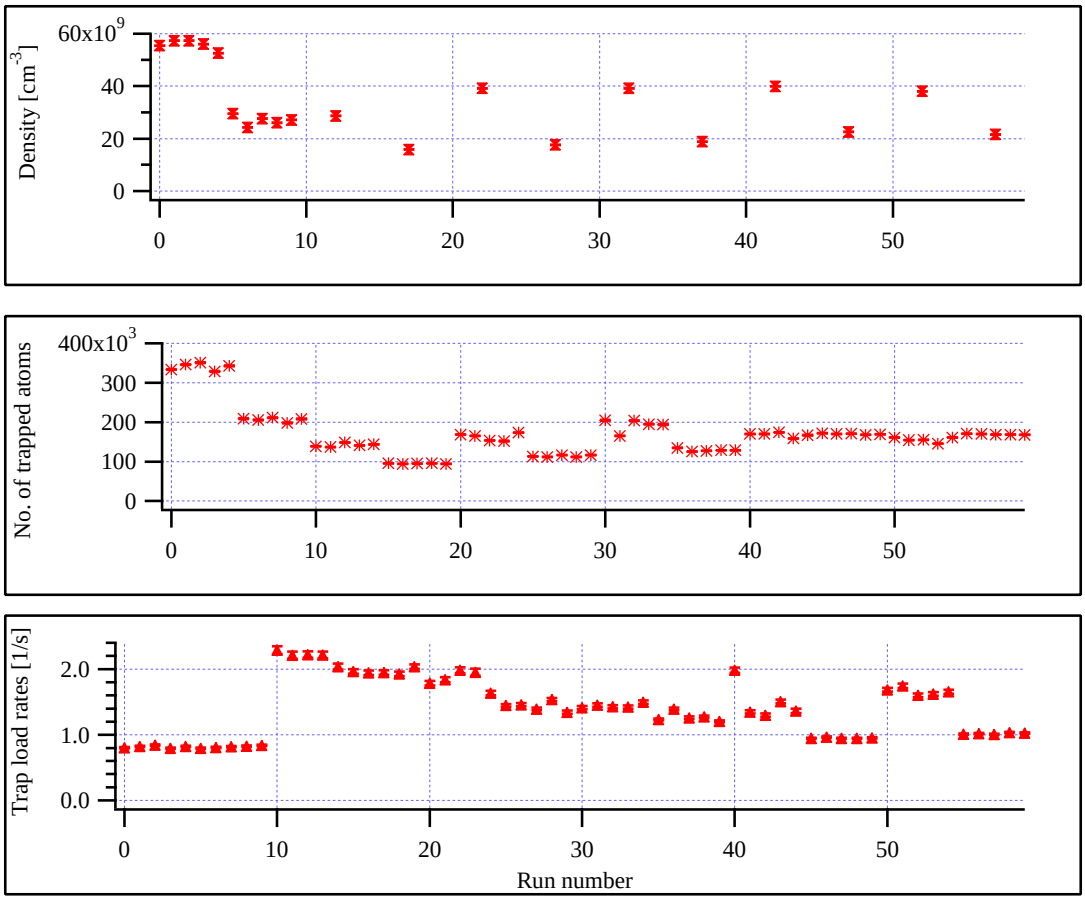

Fig. 5.7: Data from a run of the collision experiment. The top graph presents the number density, the middle graph the number of trapped atoms and the bottom graph the trap loading rate. In each graph the first five data points are for high density traps with no excitation. The second five are for low density traps with no excitation. In the top graph the succeeding points alternate between high and low density traps as the detuning goes from 0 to - 20 MHz in 5 MHz decrements. In the other two graphs groups of five data points alternate between high and low density traps as the detuning is similarly decremented.

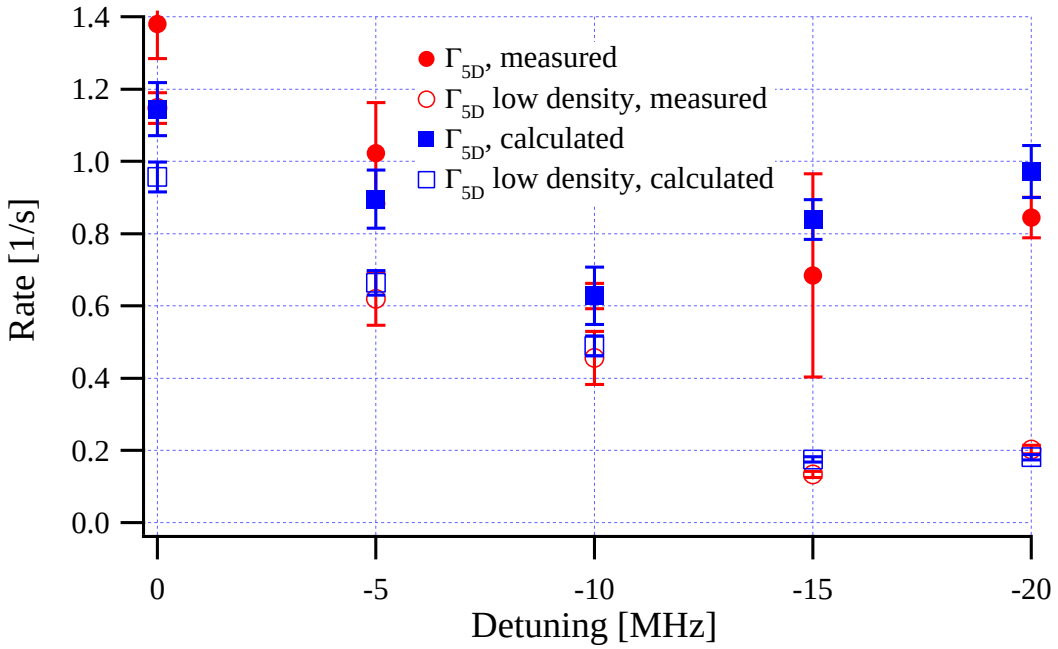

Fig. 5.8: Measured and calculated 5D loss rates. Circles represent measured values and squares the calculated. Filled markers represent the high density case and open ones the low density.

These data are analyzed using Igor, as described in App. C. The results of the analysis are presented in Figs. 5.8 and 5.9. Consider the first of these two graphs. The total 5D loss rate (i.e., the loss rate due to both photoionization and collisions) is displayed as a function of AOM frequency. Four sets of points are presented: Γ_{5D} measured from trap loading curves and Γ_{5D} calculated from the steady-state number of trapped atoms in the 5D state using Eqn. 5.47, each performed in high and low density regimes. There is troubling behavior at large red detunings of -15 and -20 MHz, where the difference in high and low density traps increases greatly. If real, this difference leads to a rather extraordinary situation, shown in Fig. 5.9. Consider Γ_{PI}, the loss rate due to photoionization. Somewhat believable loss rates are given until the higher detunings are reached,

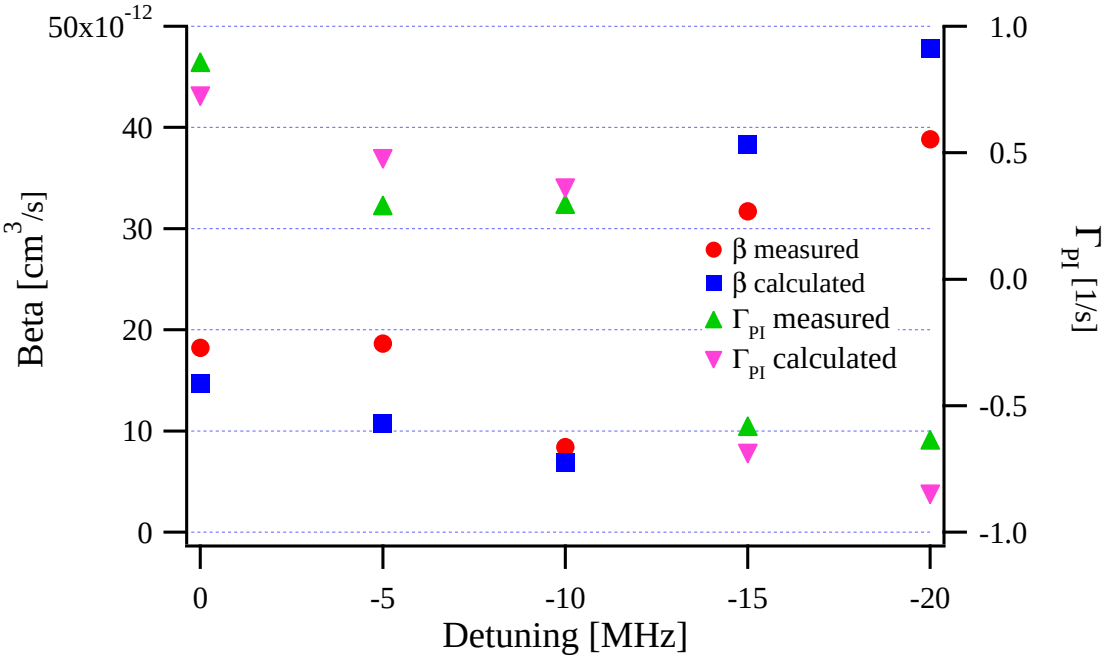

Fig. 5.9: Trap loss rate due to photoionization (right axis) and loss rate due to collisions (left axis). The measured values are determined from trap loading rates. The calculated values are from Eqn. 5.47.

when both measurements and calculations yield a *negative* loss rate, which would correspond to some sort of effect shielding the atoms from PI. Conversely, the determination of the collisional loss rate (β) shows a marked increase in the same detuning region. It could be that this is the actual conduct of the system, because other experimental runs sometimes show this, but most don't. Furthermore, this does not appear in the data from the early experiments employing a swept 776 nm laser (Fig. 5.6), where we see contradictory behavior, namely, that the trap loss has gone essentially to zero at 20 MHz detuning. Attempts at improving the performance of the experiment, including (i) detuning the lower transition laser (780 nm) to the red instead of the blue and (ii) changing the sum of 776 nm and 780 nm laser intensities while keeping the product the same (PI should go as the sum), did not produce significantly different (or better) results.

Near resonance most runs exhibited a β of about 2.2 $\times 10^{-11}$ cm^3/s with a standard deviation of the mean of 0.6 $\times 10^{-11}$ cm^3/s and an experimental uncertainty near the resolution for our apparatus. For the resolution in measuring β, Gensemer has [31]:

$$\Delta\beta = \Delta N \frac{L}{n N_0^2}, \tag{5.52}$$

where ΔN is the resolution in measuring the population and L is the loading rate. For typical parameters in this experiment this yields a resolution of about 3 $\times 10^{-12}$ cm^3/s. Fig. 5.10 presents at five different frequencies of the 776 nm laser our determinations of β (the uncertainty bars are the standard deviation of the means plus the uncertainty in resolution).

To compare our results with the theoretical predictions listed in Table 5.1 we must account for the excited state fraction, either by diluting the predictions by this value or enhancing the measured β. The 5D excited state fraction for the STIRAP-based experiments (refer to Eqn. 4.1 in Chapter 4) is about 1%.

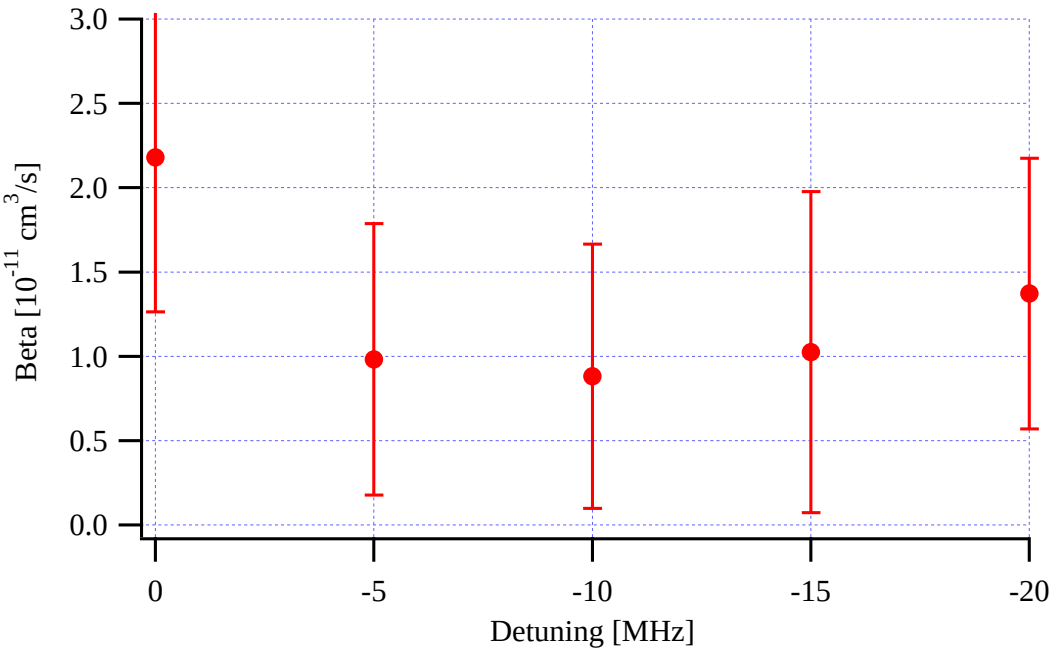

Fig. 5.10: Trap loss rate constant for various red detunings of the 776 nm high-power laser. Compare with Fig. 5.1.

Comparing the ratios of 420 nm fluorescence to 780 nm fluorescence for some PI runs and collisional runs, we see that the excited state fraction (during the excitation period) for the collisions experiment is roughly 20%. Dividing this into the value measured above gives an upper bound on β of 11 $\times 10^{-11}$ cm^3/s, which compares favorably with the predicted values.

5.5 Conclusions

This concludes this series of experiments in cold $5D_{5/2}$ Rb atoms. We have demonstrated that stimulated Raman adiabatic passage is a powerful technique for transferring population from one state to another. The full range of its applications was not even approached here, but it served its purpose well for these experiments. Other applications of STIRAP and the techniques associated with it are electromagnetically induced transparency, transfer of population between molecular states, and possibly STIRAP with Bose-Einstein condensates. With a large ensemble of 5D atoms available, we measured the 5D photoionization cross sections via trap loss. Taking into account that only a subset of the 5D m_F sublevels were populated, the experimental results agreed well with theory. Although the experiment on 5S-5D collisions did not work as well as expected, it does permit an order-of-magnitude upper bound to be placed, which is 10^{-10} cm^3/s. A better way to measure the collisional cross section would be to use a beam-loaded MOT rather than a vapor cell MOT. One could then determine the density-dependent aspect (attributable to collisions) of the decay of a trap. Another improvement would be to go to higher densities. Going to higher densities would also allow one to look for superradiant effects (e.g., the $5D \rightarrow 6P$ transition at 5.2 μm). Superradiance with cold atoms should be interesting because of the lack of Doppler broadening and the spherical shape of the sample.

Bibliography

[1] B. Broers, H. B. van Linden van den Heuvell, and L. D. Noordam, Phys. Rev. Lett. **69**, 2062 (1992).

[2] J. R. Kuklinski, U. Gaubatz, F. T. Hioe, and K. Bergmann, Phys. Rev. A **40**, 6741 (1989).

[3] S. Schiemann, A. Kuhn, S. Steuerwald, and K. Bergmann, Phys. Rev. Lett. **71**, 3637 (1993).

[4] U. Gaubatz, P. Rudecki, S. Schiemann, and K. Bergmann, J. Chem. Phys. **92**, 5363 (1990).

[5] L. S. Goldner, C. Gerz, R. J. C. Spreeuw, S. L. Rolston, C. I. Westbrook, and W. D. Phillips, Phys. Rev. Lett. **72**, 997 (1994).

[6] T. P. Dinneen, C. D. Wallace, K. N. Tan, and P. L. Gould, Opt. Lett. **17**, 1706 (1992).

[7] C. D. Wallace, V. Sanchez-Villicana, T. P. Dinneen, and P. L. Gould, Phys. Rev. Lett. **74**, 1087 (1995).

[8] D. Hoffmann, P. Feng, R. S. Williamson III, and T. Walker, Phys. Rev. Lett. **69**, 753 (1992).

[9] C. D. Wallace, T. P. Dinneen, K. N. Tan, T. T. Grove, and P. L. Gould, Phys. Rev. Lett. **69**, 897 (1992).

[10] P. Feng, D. Hoffmann, and T. Walker, Phys. Rev. A **47**, R3495 (1993).

[11] D. Hoffmann, P. Feng, and T. Walker, J. Opt. Soc. Am. B **11**, 712 (1994).

[12] M. G. Peters, D.Hoffmann, J. D. Tobiason, and T. Walker, Phys. Rev. A **50**, R906 (1994).

[13] P. D. Lett, K. Mølmer, S. D. Gensemer, K. Y. N. Tan, A. Kumarakrishnan, C. D. Wallace, and P. L. Gould, J. Phys. B **28**, 65 (1995).

[14] A. Gallagher and D. Pritchard, Phys. Rev. Lett. **63**, 957 (1989).

[15] J. Kepler, *De Cometis Tres Libelli*, vol. 7, p. 110 in *Astronomia Omnia Opera*, Heyder and Zimmer, Frankfort (1868).

[16] A. Ashkin, Phys. Rev. Lett. **25**, 1321 (1970).

[17] A. Ashkin, Phys. Rev. Lett. **40**, 729 (1978).

[18] W. Hänsch and A. Schawlow, Opt. Commun. **13**, 68 (1975).

[19] D. Wineland and H. Dehmelt, Bull. Am. Phys. Soc. **20**, 637 (1975).

[20] H. J. Metcalf and P. van der Straten, *Laser Cooling and Trapping* (Springer, New York, 1999).

[21] A.L. Migdall, J.V. Prodan, W.D. Phillips, T.H. Bergeman, and H.J. Metcalf, Phys. Rev. Lett. **54**, 2596 (1985).

[22] S. Chu, J. E. Bjorkhom, A. Ashkin, and A. Cable, Phys. Rev. Lett. **57**, 314 (1986).

[23] S. Chu, L. Hollberg, J. E. Bjorkhom, A. Cable, and A. Ashkin, Phys. Rev. Lett. **55**, 48 (1985).

[24] E. L. Raab, M. Prentiss, A. Cable, S. Chu, and D. Pritchard, Phys. Rev. Lett. **59**, 2361 (1987).

[25] C. Monroe, W. Swann, H. Robinson, and D. E. Pritchard, Phys. Rev. Lett. **59**, 2631 (1987).

[26] C. S. Adams and E. Riis, Prog. Quant. Electr. **21**, 1 (1997).

[27] A. Ashkin and J. P. Gordon, Opt. Lett. **9**, 511 (1983).

[28] T. T. Grove, *Rectified Forces in Rubidium*, PhD dissertation, University of Connecticut (Storrs CT, 1994).

[29] T. T. Grove, V. Sanchez-Villicana, B. C. Duncan, S. Maleki, and P. L. Gould, Phys. Scr. **52**, 271 (1995).

[30] T. T. Grove, B. C. Duncan, V. Sanchez-Villicana, and P. L. Gould, Phys. Rev. A **51**, R4325 (1995).

[31] S. D. Gensemer, *Characterization and Control of Ultracold Collisions*, PhD dissertation, University of Connecticut (Storrs CT, 2000).

[32] M. G. Littman and H. J. Metcalf, Appl. Opt. **17**, 2224 (1978).

[33] K. C. Harvey and C. J. Myatt, Opt. Lett. **16**, 910 (1991).

[34] L. Ricci, M. Weidemüller, T. Esslinger, A. Hemmerich, C. Zimmerman, V. Vuletic, W. Köneg, and T.W. Hänsch, Opt. Commun. **117**, 541 (1995).

[35] T. P. Dinneen, C. D. Wallace, and P. L. Gould, Opt. Commun. **92**, 277 (1992).

[36] F. T. Hioe and J. H. Eberly, Phys. Rev. Lett. **47**, 838 (1981).

[37] F. T. Hioe and J. H. Eberly, Phys. Rev. A **25**, 2168 (1982).

[38] F. T. Hioe, Phys. Lett. **99A**, 150 (1983).

[39] J. Oreg, F. T. Hioe, and J. H. Eberly, Phys. Rev. A **29**, 690 (1984).

[40] F. Shimizu, K. Shimizu, and H. Takuma, Phys. Rev. A **31**, 3132 (1985).

[41] M. Becker, U. Gaubatz, K. Bergmann, and P. L. Jones, J. Chem. Phys. **87**, 5064 (1987).

[42] U. Gaubatz, P. Rudecki, M. Becker, S. Schiemann, M. Külz, and K. Bergmann, Chem. Phys. Lett. **149**, 463 (1988).

[43] A. Lindinger, M. Verbeek, and H.-G. Rubahn, Z. Phys. D **39**, 93 (1997).

[44] J. K. Link, J. Opt. Soc. Am. **56**, 1195 (1966).

[45] O. S. Heavens, J. Opt. Soc. Am. **51**, 1058 (1961).

[46] Albert Messiah, *Quantum Mechanics* (John Wiley & Sons, New York, 1962).

[47] M. P. Fewell, B. W. Shore, and K. Bergmann, Aust. J. Phys. **50**, 281 (1997).

[48] W. Süptitz, B. C. Duncan, and P. L. Gould, J. Opt. Soc. Am. B **14**, 1001 (1997).

[49] Bruce W. Shore, *The Theory of Coherent Atomic Excitations* (John Wiley & Sons, New York, 1990).

[50] S. Guérin and H. R. Jauslin, Eur. Phys. J. D **2**, 99 (1998).

[51] T. Nakajima, Phys. Rev. A **59**, 559 (1999).

[52] N. V. Vitanov, J. Phys. B **31**, 709 (1998).

[53] J. Javanainen, Phys. Rev. A **44**, 5857 (1991).

[54] J. Javanainen, Phys. Rev. A **46**, 5819 (1992).

[55] B. C. Duncan, V. Sanchez-Villicana, P. L. Gould, and H. R. Sadeghpour, Phys. Rev. A **63**, 043411 (2001).

[56] T. Walker, D. Sesko, and C. Wieman, Phys. Rev. Lett. **64**, 408 (1990).

[57] K. Gibble, S. Kasapi, and S. Chu, Opt. Lett. **17**, 526 (1992).

[58] C. Gabbanini, S. Gozzini and A. Lucchesini, Opt. Comm. **141**, 25 (1997).

[59] O. Marago, D. Ciampini, F. Fuso, E. Arimondo, C. Gabbanini and S. T. Manson, Phys. Rev. A **57**, R4110 (1998).

[60] B. M. Patterson, T. Takekoshi and R. J. Knize, Phys. Rev. A **59**, 2508 (1999).

[61] F. Ruschewitz, J. L. Peng, R. Degner, H. Hinderthuer, D. Scheller, D. Bettermann, and W. Ertmer, in *Proceedings of the 1996 European Quantum Electronics Conference*, (1996).

[62] R. S. Schappe, P. Feng, L. W. Anderson, C. C. Lin and T. Walker, Europhys. Lett. **29**, 439 (1995).

[63] R. S. Schappe, T. Walker, L. W. Anderson and C. C. Lin, Phys. Rev. Lett. **76**, 4328 (1996).

[64] C. E. Moore, *Atomic Energy Levels* vol. II, U. S. Government Printing Office (Washington D.C.) 1971.

[65] M. Aymar, O. Robaux, and S. Wane, J. Phys. B **17**, 993 (1984).

[66] M. Marinescu, J. F. Babb, and A. Dalgarno, Phys. Rev. A **50**, 3096 (1994).

[67] M. Marinescu and A. Dalgarno, Phys. Rev. A **52**, 311 (1995).

[68] K. Orlovsky, V. Grushevsky, and A. Ekers, Eur. Phys. J. D **12**, 133 (2000).

[69] A. Fioretti, J. H. Müller, P. Verkerk, M. Allegrini, E. Arimondo, and P. S. Julienne, Phys. Rev. A **55**, R3999 (1997).

[70] M. Movre, C. Vadla, and V. Horvatic, J. Phys. B **33**, 3001 (2000).

[71] S. Magnier, M. Aubert-Frécon, O. Bouty, F. Masnou-Seeuws, Ph. Millie, and V. N. Ostrovssky, J. Phys. B **27**, 1723 (1994).

[72] I. Yu Yurova, O. Dulieu, S. Magnier, F. Masnou-Seeuws, and V. N. Ostrovssky, J. Phys. B **27**, 1723 (1994).

[73] J. L. Roberts, N. R. Claussen, J. P. Burke Jr., C. H. Greene, E. A. Cornell, and C. E. Wieman, Phys. Rev. Lett. **81**, 5109 (1998).

[74] H. W. Parker, H. A.Schuessler, R. H. Hill Jr., and B. G. Zollars, Phys. Rev. A **29**, 617 (1984).

[75] B. Bieniak, K. Fronc, S. Gateva-Kostova, M. Głódź, V. Grushevsky, J. Klavins, K. Kowalski, A. Rucińska and J. Szonert, Phys. Rev. A **62**, 022720 (2000).

[76] A. Ekers, M. Głódź, J. Szonert, B. Bieniak, K. Fronc, and T. Radelitski, Eur. Phys. J. D **8**, 49 (2000).

[77] W. Süptitz, G. Wokurka, F. Strauch, P. Kohns, and W. Ertmer, Opt. Lett. **19**, 1571 (1994).

[78] S. D. Gensemer, V. Sanchez-Villicana, K. Y. N. Tan, T. T. Grove, and P. L. Gould, Phys. Rev. A **56**, 4055 (1997).

[79] P. L. Gould, private communication (2001).

[80] I. S. Gradshteyn and I. M. Ryzhik, *Table of Integrals, Series, and Products*, fourth edition (Academic Press, New York, 1980).

[81] O. Dulieu, private communication (2001).

[82] R. J. Le Roy, Can. J. Phys. **52**, 246 (1974).

[83] B. Ji, C.-C. Tsu, and W. C. Stwalley, Chem. Phys. Lett. **236**, 242 (1995).

Appendix A

Calibration of the PMT

The photomultiplier tube (PMT) was calibrated by noting its response to a weak 780 nm laser beam of known power. The fiber optic bundle connecting the gathering lens to the narrow band filter before the PMT was unplugged at the lens and inserted in the beam path. The following measurements were taken with a 50 μA/V gain on the PMT's current amplifier. The number of photons per second is given by dividing the power by the energy per photon. The energy per photon is $h\nu$, where h is Planck's constant and ν is the frequency of the light. Thus

$$\mathcal{E}/\gamma = h\nu = h\frac{c}{\lambda}. \tag{A.1}$$

For 780 nm light the energy per photon is 2.547 $\times 10^{-19}$ J. Taking the first entry in the table as an example,

$$\frac{3 \times 10^{-7}\text{J/s}}{2.547 \times 10^{-19}\text{J}/\gamma} = 1.178 \times 10^{12}\gamma/\text{s}. \tag{A.2}$$

Table A.1: Power meter and photomultiplier tube readings.

power meter [μW]	PMT[V]
0.3	3.68
0.252	3.01
0.200	2.293

Table A.2: Photons/second and photomultiplier tube calibration.

γ /s	PMT current [μA]	PMT calibration [$\gamma \cdot s^{-1} \cdot \mu A^{-1}$]
1.178 $\times 10^{12}$	184	6.4 $\times 10^{9}$
9.894 $\times 10^{11}$	150.4	6.57 $\times 10^{9}$
7.852 $\times 10^{11}$	114.7	6.85 $\times 10^{9}$

From the current amplifier gain we see that the PMT current for that example is 184 μA. The average is 6.6 $\times 10^{9} \gamma \cdot \mathrm{s}^{-1} \cdot \mu \mathrm{A}^{-1}$. The radius of the gathering lens is about 12 mm and it is located about 75 mm from the trap; hence, it subtends

$$\frac{\pi r^2}{4\pi R^2} = \frac{(12)^2}{4\,(75)^2} \simeq 0.6\% \simeq \frac{1}{156}. \tag{A.3}$$

The atoms scatter photons at a rate of the excited state fraction divided by the 5P lifetime (27 ns). The excited state fraction is given by

$$f = \frac{I/I_{sat}}{1 + 4\,(\Delta/\Gamma)^2 + 2\,(I/I_{sat})}, \tag{A.4}$$

where I_{sat} is the m_F-averaged saturation intensity for the transition (7.56 mW/cm^2) and Δ is the detuning from resonance. For typical laser intensities (12 mW/cm^2) at a common detuning (1.2 Γ) we get an excited state fraction of about 0.083 and a scattering rate R of 3.075 $\times 10^{6} \mathrm{s}^{-1}$. The number of atoms in the trap is the product of the PMT calibration, the amplifier gain and the signal amplitude divided by the fractional angle subtended by the gathering lens and the scattering rate. Typical parameters yield:

$$N = \left(6.6 \times 10^{9} \gamma \cdot \mathrm{s}^{-1} \cdot \mu \mathrm{A}^{-1}\right) (1 \mu \mathrm{A/V})\,(0.4 \mathrm{V})\,(156)\left(1 \mathrm{s}/3.075 \times 10^{6}\right), \tag{A.5}$$

or roughly 1.3 $\times 10^{5}$ atoms. Under different conditions there can be three or four times as many atoms.

Appendix B

STIRAP Calculations

B.1 Obtaining the STIRAP Wave Function

There are several different theoretical approaches to the problem of population transfer in a three (or more) state system. The one taken here largely follows Bruce Shore (especially §13.1 in [49]). Among the other methods are the use of Floquet theory (see for instance [50]), dressed states ([51]) and analysis of non-STIRAP processes ([52]).

We use electric dipole allowed (E1) transitions in the rotating-wave approximation. Two monochromatic fields connecting three atomic states create by superposition this electric field:

$$\mathbf{E(t)} = \Re[\boldsymbol{\epsilon_1}\mathcal{E}_1\ exp(-i\omega_1 t) + \boldsymbol{\epsilon_3}\mathcal{E}_3\ exp(-i\omega_3 t)]. \tag{B.1}$$

The state vector is constructed thus:

$$\Psi(t) = \sum_{n=1}^{3} \psi_n C_n(t)\ exp[-i\zeta_n(t)]. \tag{B.2}$$

The phases ζ_n will be chosen to simplify the expressions. Substituting the state vector expansion into the Schrödinger equation yields a set of three coupled equations, the first of which is:

$$\begin{aligned} \hbar\frac{d}{dt}C_1 &= -i[E_1 - \hbar\dot{\zeta}_1]C_1 \\ &\quad + \frac{i}{2}[\mathbf{d_{12}}\cdot\boldsymbol{\epsilon_1}\mathcal{E}_1\ exp(-i\omega_1 t - i\zeta_2 + i\zeta_1) \end{aligned}$$

$$
\begin{aligned}
&+ \mathbf{d_{12}} \cdot \epsilon_{\mathbf{1}}^{*} \mathcal{E}_1^{*}\ exp(+i\omega_1 t - i\zeta_2 + i\zeta_1) \\
&+ \mathbf{d_{12}} \cdot \epsilon_{\mathbf{3}} \mathcal{E}_3\ exp(-i\omega_3 t - i\zeta_2 + i\zeta_1) \\
&+ \mathbf{d_{12}} \cdot \epsilon_{\mathbf{3}}^{*} \mathcal{E}_3^{*}\ exp(+i\omega_3 t - i\zeta_2 + i\zeta_1)]C_2, \qquad \text{(B.3)}
\end{aligned}
$$

where $\mathbf{d_{12}}$ is the atomic dipole moment, $\boldsymbol{\epsilon}$ is a unit polarization vector, $\boldsymbol{\mathcal{E}}$ is the electric field amplitude, ω_i is the frequency of field i and E_1 is the energy level of the first state (usually set to zero). The third coupled equation is of like form to the first, *mutatis mutandis*:

$$
\begin{aligned}
\hbar\frac{d}{dt}C_3 \;=\; & -i[E_3 - \hbar\dot{\zeta_3}]C_3 \\
& + \frac{i}{2}[\mathbf{d_{23}} \cdot \epsilon_{\mathbf{3}} \mathcal{E}_3\ exp(-i\omega_3 t - i\zeta_2 + i\zeta_3) \\
& + \mathbf{d_{23}} \cdot \epsilon_{\mathbf{3}}^{*} \mathcal{E}_3^{*}\ exp(+i\omega_3 t - i\zeta_2 + i\zeta_3) \\
& + \mathbf{d_{23}} \cdot \epsilon_{\mathbf{3}} \mathcal{E}_3\ exp(-i\omega_3 t - i\zeta_2 + i\zeta_3) \\
& + \mathbf{d_{23}} \cdot \epsilon_{\mathbf{3}}^{*} \mathcal{E}_3^{*}\ exp(+i\omega_3 t - i\zeta_2 + i\zeta_3)]C_2. \qquad \text{(B.4)}
\end{aligned}
$$

The second coupled equation has one set of four exponentials for C_1, another set for C_3, and $-i[E_2 - \hbar\dot{\zeta_2}]$ as the factor for C_2:

$$
\begin{aligned}
\hbar\frac{d}{dt}C_2 \;=\; & -i[E_2 - \hbar\dot{\zeta_2}]C_2 \\
& + \frac{i}{2}[\mathbf{d_{12}} \cdot \epsilon_{\mathbf{1}} \mathcal{E}_1\ exp(-i\omega_1 t - i\zeta_2 + i\zeta_1) \\
& + \mathbf{d_{12}} \cdot \epsilon_{\mathbf{1}}^{*} \mathcal{E}_1^{*}\ exp(+i\omega_1 t - i\zeta_2 + i\zeta_1) \\
& + \mathbf{d_{12}} \cdot \epsilon_{\mathbf{3}} \mathcal{E}_3\ exp(-i\omega_3 t - i\zeta_2 + i\zeta_1) \\
& + \mathbf{d_{12}} \cdot \epsilon_{\mathbf{3}}^{*} \mathcal{E}_3^{*}\ exp(+i\omega_3 t - i\zeta_2 + i\zeta_1)]C_1 \\
& + \frac{i}{2}[\mathbf{d_{23}} \cdot \epsilon_{\mathbf{3}} \mathcal{E}_3\ exp(-i\omega_1 t - i\zeta_2 + i\zeta_3) \\
& + \mathbf{d_{23}} \cdot \epsilon_{\mathbf{3}}^{*} \mathcal{E}_3^{*}\ exp(+i\omega_1 t - i\zeta_2 + i\zeta_3) \\
& + \mathbf{d_{23}} \cdot \epsilon_{\mathbf{3}} \mathcal{E}_3\ exp(-i\omega_3 t - i\zeta_2 + i\zeta_3) \\
& + \mathbf{d_{23}} \cdot \epsilon_{\mathbf{3}}^{*} \mathcal{E}_3^{*}\ exp(+i\omega_3 t - i\zeta_2 + i\zeta_3)]C_3. \qquad \text{(B.5)}
\end{aligned}
$$

Consider Eqn. B.3. The phase is chosen so that one exponential term becomes 1 and that a convenient zero-point energy is given. In a ladder system of $E_1 < E_2 < E_3$ one can choose

$$\zeta_2 = \zeta_1 + \omega_1 t, \tag{B.6}$$

to which can be added a constant phase. This phase ζ_2 sets the argument of the second exponential to zero and makes the others:

$$\begin{aligned} -\omega_1 t - \zeta_2 + \zeta_1 &= -2\omega_1 t \\ -\omega_3 t - \zeta_2 + \zeta_1 &= -(\omega_3 + \omega_1)t \\ +\omega_3 t - \zeta_2 + \zeta_1 &= (\omega_3 - \omega_1)t. \end{aligned} \tag{B.7}$$

For the second coupled equation we choose

$$\zeta_3 = \zeta_2 + \omega_3 t, \tag{B.8}$$

which gives

$$-\omega_1 t - \zeta_2 + \zeta_3 = (\omega_3 - \omega_1)t \tag{B.9}$$

$$+\omega_1 t - \zeta_2 + \zeta_3 = (\omega_3 + \omega_1)t \tag{B.10}$$

$$+\omega_3 t - \zeta_2 + \zeta_3 = 2\omega_3 t. \tag{B.11}$$

There are four different frequencies in Eqn. B.7 and B.11, viz., $2\omega_1, 2\omega_3, \omega_1 + \omega_3$ and $\omega_3 - \omega_1$. For the rotating-wave approximation to hold these frequencies must be very large, so that there are many oscillations during the process. The difference of $\omega_3 - \omega_1$ is obviously the smallest of the four. This difference must be much larger than any detuning or Rabi rate. For the parameters of our STIRAP experiment the largest Rabi rate is about $2\pi \times 2 \times 10^8 \mathrm{s}^{-1}$, compared to

$$\begin{aligned} \omega_3 - \omega_1 &= 2\pi(\nu_3 - \nu_1) \\ &= 2\pi c(\frac{1}{\lambda_3} - \frac{1}{\lambda_1}) \\ &= 2\pi c(\frac{1}{776\mathrm{nm}} - \frac{1}{780\mathrm{nm}}) \\ &= 1.24 \times 10^{13}\mathrm{s}^{-1}. \end{aligned} \tag{B.12}$$

Thus we are justified in using the rotating-wave approximation and may set these exponentials to zero. We can add phase constants to ζ_2 and ζ_3, so that the Rabi rates are real and non-negative as long as the phases of the electric fields remain constant. To simplify the presentation let's define

$$\hbar\Delta_i \equiv E_i - \hbar\dot{\zeta}_i \tag{B.13}$$

$$\hbar\Omega_1 = -\mathbf{d_{12}} \cdot \epsilon_\mathbf{1}\mathcal{E}_1. \tag{B.14}$$

Set the lowest energy (E_1) and Δ_1 to zero. Ignoring losses from the various states, we get the following matrix as the Hamiltonian for the atom-field interaction:

$$H = -\frac{\hbar}{2}\begin{bmatrix} 0 & \Omega_1 & 0 \\ \Omega_1 & 2\Delta_2 & \Omega_3 \\ 0 & \Omega_3 & \Delta_3 \end{bmatrix}. \tag{B.15}$$

Consider Eqn. B.13 for the third coupled equation. For the choices of phase made above we get

$$\begin{aligned} \hbar\Delta_3 &= E_3 - \hbar\dot{\zeta}_3 \\ &= E_3 - E_1 - \hbar(\omega_1 + \omega_3) + \hbar\Delta_1. \end{aligned} \tag{B.16}$$

This goes to zero when the energy difference between the first and third states equals the energy of the electric field ($\hbar[\omega_1 + \omega_3]$), i.e., when the system is on two-photon resonance. With that requirement the Hamiltonian becomes

$$H = -\frac{\hbar}{2}\begin{bmatrix} 0 & \Omega_1 & 0 \\ \Omega_1 & 2\Delta_2 & \Omega_3 \\ 0 & \Omega_3 & 0 \end{bmatrix}. \tag{B.17}$$

Setting the determinant of the Hamiltonian to zero yields three eigenvalues, namely:

$$\lambda_0 = 0 \tag{B.18}$$

$$\lambda_\pm = \Delta_2 \mp \sqrt{\Delta_2^2 + \Omega_1^2 + \Omega_3^2}. \tag{B.19}$$

We are interested in the zero eigenvalue. Its normalized eigenvector is

$$|\lambda_0 >= \frac{1}{\sqrt{\Omega_1^2 + \Omega_3^2}} \{\Omega_3|1> -\Omega_1|3>\}. \tag{B.20}$$

By defining the following mixing angle Θ

$$\begin{aligned} \sin\Theta &= \frac{\Omega_1}{\sqrt{\Omega_1^2 + \Omega_3^2}} \\ \cos\Theta &= \frac{\Omega_3}{\sqrt{\Omega_1^2 + \Omega_3^2}} \\ \tan\Theta &= \frac{\Omega_1}{\Omega_3}, \end{aligned} \tag{B.21}$$

we can rewrite Eqn. B.20 as

$$|\lambda_0 >= \cos\Theta|1> -\sin\Theta|3>, \qquad \Theta \in [0, \pi/2]. \tag{B.22}$$

Now consider Eqn. B.13 for the second coupled equation. For the choices of phase made above we get

$$\begin{aligned} \hbar\Delta_2 &= E_2 - \hbar\dot{\zeta}_2 \\ &= E_2 - E_1 - \hbar\omega_1 + \hbar\Delta_1. \end{aligned} \tag{B.23}$$

The choice of energy scale and the various phases makes Δ_2 the one-photon detuning of the lower laser field, and, because the system is two-photon resonant, it is also the detuning of the upper field, with opposite sign. To indicate that this quantity is the detuning of the lower transition, in the main body of this text this quantity is subscripted with a 1 instead of a 2.

B.2 Determining the Dipole Matrix Element

In the following tables are found the dipole matrix elements for Rb 85 and Rb 87. The dipole elements are the product of the absolute value of the Clebsch-Gordan coefficients and the reduced dipole matrix elements (S $\rightarrow$ P 2.96 ea_0 and P $\rightarrow$ D 0.79 ea_0).

Table B.1: Rb 85 dipole moments, 5S, F=3 $\rightarrow$ 5P, F'=4.

transition		$\mu[ea_0]$	$\mu^2[(ea_0)^2]$
5S, F=3 $\rightarrow$ 5P, F'=4, Δm = 0	-3 $\rightarrow$ -3	1.48	2.1904
	-2 $\rightarrow$ -2	1.93777	3.75497
	-1 $\rightarrow$ -1	2.1665	4.69371
	0 $\rightarrow$ 0	2.23755	5.00663
	1 $\rightarrow$ 1	2.1665	4.69371
	2 $\rightarrow$ 2	1.93777	3.75497
	3 $\rightarrow$ 3	1.48	2.1904
	$\bar{\mu}$ =	1.91516	
5S, F=3 $\rightarrow$ 5P, F'=4, Δm = +1	-3 $\rightarrow$ -2	0.559387	0.312914
	-2 $\rightarrow$ -1	0.968887	0.938743
	-1 $\rightarrow$ 0	1.37021	1.87749
	0 $\rightarrow$ 1	1.76894	3.12914
	1 $\rightarrow$ 2	2.1665	4.69371
	2 $\rightarrow$ 3	2.56344	6.5712
	3 $\rightarrow$ 4	2.96	8.7616
	$\bar{\mu}$ =	1.76534	

Table B.2: Rb 85 dipole moments, 5P, F=4 $\rightarrow$ 5D, F'=3.

transition		$\mu[ea_0]$	$\mu^2[(ea_0)^2]$
5P, F=4 $\rightarrow$ 5D, F'=3, Δm = 0	-3 $\rightarrow$ -3	-0.348357	0.121353
	-2 $\rightarrow$ -2	-0.456107	0.208033
	-1 $\rightarrow$ -1	-0.509943	0.260042
	0 $\rightarrow$ 0	-0.526667	0.277378
	1 $\rightarrow$ 1	-0.509943	0.260042
	2 $\rightarrow$ 2	-0.456107	0.208033
	3 $\rightarrow$ 3	-0.348357	0.121353
	$\bar{\mu}$ =	0.450783	
5P, F=4 $\rightarrow$ 5D, F'=3, Δm = +1	-4 $\rightarrow$ -3	0.696715	0.485411
	-3 $\rightarrow$ -2	0.603372	0.364058
	-2 $\rightarrow$ -1	0.509943	0.260042
	-1 $\rightarrow$ 0	0.416367	0.173361
	0 $\rightarrow$ 1	0.322516	0.104017
	1 $\rightarrow$ 2	0.228053	0.0520083
	2 $\rightarrow$ 3	0.131667	0.0173361
	$\bar{\mu}$ =	0.415519	

Table B.3: Rb 85 dipole moments, 5P, F=4 → 5D, F'=4.

transition		$\mu[ea_0]$	$\mu^2[(ea_0)^2]$
5P, F=4 → 5D, F'=4, Δm = 0	-4 → -4	-0.706597	0.49928
	-3 → -3	-0.529948	0.280845
	-2 → -2	-0.353299	0.12482
	-1 → -1	-0.176649	0.031205
	0 → 0	0	0
	1 → 1	0.176649	0.031205
	2 → 2	0.353299	0.12482
	3 → 3	0.529948	0.280845
	4 → 4	0.706597	0.49928
	$\bar{\mu}$ =	0.392554	
5P, F=4 → 5D, F'=4, Δm = +1	-4 → -3	-0.353299	0.12482
	-3 → -2	-0.46737	0.218435
	-2 → -1	-0.529948	0.280845
	-1 → 0	-0.558614	0.31205
	0 → 1	-0.558614	0.31205
	1 → 2	-0.529948	0.280845
	2 → 3	-0.46737	0.218435
	3 → 4	-0.353299	0.12482
	$\bar{\mu}$ =	0.477308	

Table B.4: Rb 85 dipole moments, 5P, F=4 → 5D, F'=5.

transition		$\mu[ea_0]$	$\mu^2[(ea_0)^2]$
5P, F=4 → 5D, F'=5, Δm = 0	-4 → -4	0.353299	0.12482
	-3 → -3	0.471065	0.221902
	-2 → -2	0.539673	0.291247
	-1 → -1	0.576934	0.332853
	0 → 0	0.588831	0.346722
	1 → 1	0.576934	0.332853
	2 → 2	0.539673	0.291247
	3 → 3	0.471065	0.221902
	4 → 4	0.353299	0.12482
	$\bar{\mu}$ =	0.496753	
5P, F=4 → 5D, F'=5, Δm = +1	-4 → -3	0.117766	0.0138689
	-3 → -2	0.203977	0.0416067
	-2 → -1	0.288467	0.0832133
	-1 → 0	0.37241	0.138689
	0 → 1	0.456107	0.208033
	1 → 2	0.539673	0.291247
	2 → 3	0.62316	0.388329
	3 → 4	0.706597	0.49928
	4 → 5	0.79	0.6241
	$\bar{\mu}$ =	0.455351	

Table B.5: Rb 87 dipole moments, 5S, F=2 → 5P, F'=3.

transition		$\mu[ea_0]$	$\mu^2[(ea_0)^2]$
5S, F=2 → 5P, F'=3, Δm = 0	-2→-2	1.70896	2.92053
	-1→-1	2.16168	4.67285
	0→0	2.29281	5.25696
	1→1	2.16168	4.67285
	2→2	1.70896	2.92053
	$\bar{\mu}$ =	2.00682	
5S, F=2 → 5P, F'=3, Δm = +1	-2→-1	0.764269	0.584107
	-1→0	1.32375	1.75232
	0→1	1.87207	3.50464
	1→2	2.41683	5.84107
	2→3	2.96	8.7616
	$\bar{\mu}$ =	1.86738	

Table B.6: Rb 87 dipole moments, 5P, F=3 → 5D, F'=2.

transition		$\mu[ea_0]$	$\mu^2[(ea_0)^2]$
5P, F=3 → 5D, F'=2, Δm = 0	-2→-2	-0.385481	0.148595
	-1→-1	-0.487599	0.237752
	0→0	-0.517176	0.267471
	1→1	-0.487599	0.237752
	2→2	-0.385481	0.148595
	$\bar{\mu}$ =	0.452667	
5P, F=3 → 5D, F'=2, Δm = +1	-3→-2	0.667672	0.445786
	-2→-1	0.545152	0.29719
	-1→0	0.422273	0.178314
	0→1	0.298592	0.0891571
	1→2	0.172392	0.029719
	$\bar{\mu}$ =	0.421216	

Table B.7: Rb 87 dipole moments, 5P, F=3 → 5D, F'=3.

transition		$\mu[ea_0]$	$\mu^2[(ea_0)^2]$
5P, F=3 → 5D, F'=3, Δm = 0	-3→-3	-0.68416	0.468075
	-2→-2	-0.456107	0.208033
	-1→-1	-0.228053	0.0520083
	0→0	0	0
	1→1	0.228053	0.0520083
	2→2	0.456107	0.208033
	3→3	0.68416	0.468075
	$\bar{\mu}$ =	0.390949	
5P, F=3 → 5D, F'=3, Δm = +1	-3→-2	-0.395	0.156025
	-2→-1	-0.509943	0.260042
	-1→0	-0.558614	0.31205
	0→1	-0.558614	0.31205
	1→2	-0.509943	0.260042
	2→3	-0.395	0.156025
	$\bar{\mu}$ =	0.487852	

Table B.8: Rb 87 dipole moments, 5P, F=3 → 5D, F'=4.

transition		$\mu[ea_0]$	$\mu^2[(ea_0)^2]$
5P, F=3 → 5D, F'=4, Δm = 0	-3→-3	0.395	0.156025
	-2→-2	0.517176	0.267471
	-1→-1	0.578221	0.334339
	0→0	0.597184	0.356629
	1→1	0.578221	0.334339
	2→2	0.517176	0.267471
	3→3	0.395	0.156025
	$\bar{\mu}$ =	0.51114	
5P, F=3 → 5D, F'=4, Δm = +1	-3→-2	0.149296	0.0222893
	-2→-1	0.258588	0.0668679
	-1→0	0.365699	0.133736
	0→1	0.472115	0.222893
	1→2	0.578221	0.334339
	2→3	0.68416	0.468075
	3→4	0.79	0.6241
	$\bar{\mu}$ =	0.471154	

B.3 Relevant Clebsh-Gordan Coefficients

The following Clebsch-Gordan coefficients, calculated in Mathematica, were used in determing the dipole matrix elements.

87Rb 5S F=2 $\rightarrow$ 5P F'=3, Δ m = 0

$$\begin{aligned} \langle 2,1,-2,0|2,1,3,-2\rangle &= \langle 2,1,2,0|2,1,3,2\rangle &= 0.57735 \\ \langle 2,1,-1,0|2,1,3,-1\rangle &= \langle 2,1,1,0|2,1,3,1\rangle &= 0.730297 \\ \langle 2,1,0,0|2,1,3,0\rangle & & = 0.774597 \end{aligned}$$

87Rb 5P F=3 $\rightarrow$ 5D F'=4, Δ m = 0 is the same as:

85Rb 5S F=3 $\rightarrow$ 5P F'=4, Δ m = 0

$$\begin{aligned} \langle 3,1,-3,0|3,1,4,-3\rangle &= \langle 3,1,-3,0|3,1,4,-3\rangle &= 0.5 \\ \langle 3,1,-2,0|3,1,4,-2\rangle &= \langle 3,1,-2,0|3,1,4,-2\rangle &= 0.654654 \\ \langle 3,1,-1,0|3,1,4,-1\rangle &= \langle 3,1,1,0|3,1,4,1\rangle &= 0.731925 \\ \langle 3,1,0,0|3,1,4,0\rangle & & = 0.755929 \end{aligned}$$

85Rb 5P F=4 $\rightarrow$ 5D F'=5, Δ m = 0

$$\begin{aligned} \langle 4,1,-4,0|4,1,5,-4\rangle &= \langle 4,1,-4,0|4,1,5,-4\rangle &= 0.447214 \\ \langle 4,1,-3,0|4,1,5,-3\rangle &= \langle 4,1,3,0|4,1,5,3\rangle &= 0.596285 \\ \langle 4,1,-2,0|4,1,5,-2\rangle &= \langle 4,1,2,0|4,1,5,2\rangle &= 0.68313 \\ \langle 4,1,-1,0|4,1,5,-1\rangle &= \langle 4,1,1,0|4,1,5,1\rangle &= 0.730297 \\ \langle 4,1,0,0|4,1,5,0\rangle & & = 0.745356 \end{aligned}$$

87Rb 5S F=2 $\rightarrow$ 5P F'=3, Δ m = +1

$$\langle 2,1,-2,1|2,1,3,-1\rangle = 0.258199$$

$$\begin{aligned}
\langle 2,1,-1,1|2,1,3,0\rangle &= 0.447214 \\
\langle 2,1,0,1|2,1,3,1\rangle &= 0.632456 \\
\langle 2,1,1,1|2,1,3,2\rangle &= 0.816497 \\
\langle 2,1,2,2|2,1,3,3\rangle &= 1
\end{aligned}$$

87Rb 5P F=3 $\rightarrow$ 5D F'=4, Δ m = +1 is the same as:
85Rb 5S F=3 $\rightarrow$ 5P F'=4, Δ m = +1

$$\begin{aligned}
\langle 3,1,-3,1|3,1,4,-2\rangle &= 0.188982 \\
\langle 3,1,-2,1|3,1,4,-1\rangle &= 0.327327 \\
\langle 3,1,-1,1|3,1,4,0\rangle &= 0.46291 \\
\langle 3,1,0,1|3,1,4,1\rangle &= 0.597614 \\
\langle 3,1,1,1|3,1,4,2\rangle &= 0.731925 \\
\langle 3,1,2,1|3,1,4,3\rangle &= 0.866025 \\
\langle 3,1,3,1|3,1,4,4\rangle &= 1
\end{aligned}$$

85Rb 5P F=4 $\rightarrow$ 5D F'=5, Δ m = +1

$$\begin{aligned}
\langle 4,1,-4,1|4,1,5,-3\rangle &= 0.149071 \\
\langle 4,1,-3,1|4,1,5,-2\rangle &= 0.258199 \\
\langle 4,1,-2,1|4,1,5,-1\rangle &= 0.365148 \\
\langle 4,1,-1,1|4,1,5,0\rangle &= 0.471405 \\
\langle 4,1,0,1|4,1,5,1\rangle &= 0.57735 \\
\langle 4,1,1,1|4,1,5,2\rangle &= 0.68313 \\
\langle 4,1,2,1|4,1,5,3\rangle &= 0.788811 \\
\langle 4,1,3,1|4,1,5,4\rangle &= 0.894427
\end{aligned}$$

$$\langle 4,1,4,1|4,1,5,5\rangle \quad = 1$$

87Rb 5P F=3 $\rightarrow$ 5D F'=3, Δ m = 0

$$\begin{aligned}
\langle 3,1,-3,0|3,1,3,-3\rangle &= -0.866025 \\
\langle 3,1,-2,0|3,1,3,-2\rangle &= -0.57735 \\
\langle 3,1,-1,0|3,1,3,-1\rangle &= -0.288675 \\
\langle 3,1,0,0|3,1,3,0\rangle &= 0 \\
\langle 3,1,1,0|3,1,3,1\rangle &= 0.288675 \\
\langle 3,1,2,0|3,1,3,2\rangle &= 0.57735 \\
\langle 3,1,3,0|3,1,3,3\rangle &= 0.866025
\end{aligned}$$

85Rb 5P F=4 $\rightarrow$ 5D F'=4, Δ m = 0

$$\begin{aligned}
\langle 4,1,-4,0|4,1,4,-4\rangle &= -0.894427 \\
\langle 4,1,-3,0|4,1,4,-3\rangle &= -0.67082 \\
\langle 4,1,-2,0|4,1,4,-2\rangle &= -0.447214 \\
\langle 4,1,-1,0|4,1,4,-1\rangle &= -0.223607 \\
\langle 4,1,0,0|,4,1,4,0\rangle &= 0 \\
\langle 4,1,1,0|4,1,4,1\rangle &= 0.223607 \\
\langle 4,1,2,0|4,1,4,2\rangle &= 0.447214 \\
\langle 4,1,3,0|4,1,4,3\rangle &= 0.67082 \\
\langle 4,1,4,0|4,1,4,4\rangle &= 0.894427
\end{aligned}$$

87Rb 5P F=3 $\rightarrow$ 5D F'=2, Δ m = 0

$$\langle 3,1,-2,0|3,1,2,-2\rangle \quad = \langle 3,1,2,0|3,1,2,2\rangle \quad = -0.48795$$

$$\begin{aligned}
\langle 3,1,-1,0|3,1,2,-1\rangle &= \langle 3,1,1,0|3,1,2,1\rangle &= -0.617213\\
\langle 3,1,0,0|3,1,2,0\rangle &&= -0.654654
\end{aligned}$$

85Rb 5P F=4 $\rightarrow$ 5D F'=3, Δ m = 0

$$\begin{aligned}
\langle 4,1,-3,0|4,1,3,-3\rangle &= \langle 4,1,3,0|4,1,3,3\rangle &= -0.440959\\
\langle 4,1,-2,0|4,1,3,-2\rangle &= \langle 4,1,2,0|4,1,3,2\rangle &= -0.57735\\
\langle 4,1,-1,0|4,1,3,-1\rangle &= \langle 4,1,1,0|4,1,3,1\rangle &= -0.645497\\
\langle 4,1,0,0|4,1,3,0\rangle &&= -0.666667
\end{aligned}$$

87Rb 5P F=3 $\rightarrow$ 5D F'=3, Δ m = +1

$$\begin{aligned}
\langle 3,1,-3,1|3,1,3,-2\rangle &= -0.5\\
\langle 3,1,-2,1|3,1,3,-1\rangle &= -0.645497\\
\langle 3,1,-1,1|3,1,3,0\rangle &= -0.707107\\
\langle 3,1,0,1|3,1,3,1\rangle &= -0.707107\\
\langle 3,1,1,1|3,1,3,2\rangle &= -0.645497\\
\langle 3,1,2,1|3,1,3,3\rangle &= -0.5
\end{aligned}$$

85Rb 5P F=4 $\rightarrow$ 5D F'=4, Δ m = +1

$$\begin{aligned}
\langle 4,1,-4,1|4,1,4,-3\rangle &= -0.447214\\
\langle 4,1,-3,1|4,1,4,-2\rangle &= -0.591608\\
\langle 4,1,-2,1|4,1,4,-1\rangle &= -0.67082\\
\langle 4,1,-1,1|4,1,4,0\rangle &= -0.707107\\
\langle 4,1,0,1|4,1,4,1\rangle &= -0.707107
\end{aligned}$$

$$\langle 4,1,1,1|4,1,4,2\rangle = -0.67082$$
$$\langle 4,1,2,1|4,1,4,3\rangle = -0.591608$$
$$\langle 4,1,3,1|4,1,4,4\rangle = -0.447214$$

87Rb 5P F=3 $\rightarrow$ 5D F'=2, Δ m = +1

$$\langle 3,1,-3,1|3,1,2,-2\rangle = 0.845154$$
$$\langle 3,1,-2,1|3,1,2,-1\rangle = 0.690066$$
$$\langle 3,1,-1,1|3,1,2,0\rangle = 0.534522$$
$$\langle 3,1,0,1|3,1,2,1\rangle = 0.377964$$
$$\langle 3,1,1,1|3,1,2,2\rangle = 0.218218$$

85Rb 5P F=4 $\rightarrow$ 5D F'=3, Δ m = +1

$$\langle 4,1,-4,1|4,1,3,-3\rangle = 0.881917$$
$$\langle 4,1,-3,1|4,1,3,-2\rangle = 0.763763$$
$$\langle 4,1,-2,1|4,1,3,-1\rangle = 0.645497$$
$$\langle 4,1,-1,1|4,1,3,0\rangle = 0.527046$$
$$\langle 4,1,0,1|4,1,3,1\rangle = 0.408248$$
$$\langle 4,1,1,1|4,1,3,2\rangle = 0.288675$$
$$\langle 4,1,2,1|4,1,3,3\rangle = 0.166667$$

B.4 Code for STIRAP Simulations

The following code controls the "software atom" written by Juha Javanainen [53,54]. Wenko Süptitz wrote most of the adaptations. The names of variables and constants are generally easily understood, e.g., "pop" for population, followed by the state (s, p or d), and "detl,detu" for lower and upper detuning, respectively (in units of Γ). "Gl" is for gamma-lower, i.e., $\Gamma \equiv \Gamma_1 = 2\pi \times 5.89$ MHz. "Gu" is for gamma-upper, or $\Gamma_3 = .112121 \times \Gamma = 2\pi \times 0.66$ MHz. In this particular example the amplitude of the 776 nm pulse is fixed and that of the 780 nm pulse reduced iteratively. It is a simple matter to switch roles. There are several instructions preparing the output file as input to the Igor program for analysis. Near the end of the program comes the definition of the laser pulses as gaussians. The prime interest in this example is the use of the individual Clebsch-Gordan coefficients to weight the contribution from each m_F level and summing rather than using an average. The result bears out the contention that there is no significant disadvantage in using the average.

```
/*      Copyright (C) 1993 Juha Javanainen. The present software may be
copied, modified, distributed and used freely for the the purposes of
scientific research, provided this copyright notice remains attached
to the software. Any commercial use of the software is expressly
prohibited. */

/*      Numerical Implementation of the Semiclassical Theory of Atom-Field
Interactions.  V. 1.0, May 12, 1993. */

/*      This program demonstrades the STIRAP process in a Rb cascade system
WS 8/13/95 */

#include      "config.h"
#include      <stdio.h>
#include      <math.h>
#include      "l_eqs_td.h"
```

```
#ifdef      MACII
double      Er(double t, void* parms);
#endif      MACII
#ifdef      SUN
double      Er();
#endif      SUN

main()
{
clPtr        Cl;           /* atomic level scheme */
int           S,P,D;      /* names of levels */
LL0Ptr     llp;          /* density matrix eqs. */
LoPtr       pops;      /* population operator for each ground state */
LoPtr       popp, popd;      /* population operator for excited level */
LoPtr       rho;        /* density operator */
LudPtr     lup;         /* control structure for updates */
double      psl[4], psu[4];   /* parameters of "lower" and "upper" pulses */
double      psli0i, psui0i,
               psli0ii,psui0ii;
double      v;           /* state counter */
double      t,tl,tu,h,ps;   /* time, interval for integration, time step, plot
step */
FILE      *output;     /* output file name */
int           count, cut,s;      /* auxiliaries */
double      aux, w;     /* auxiliary */
double      Gl = 1.0;                /* "lower" spontaneous emission rate */
double      Gu = .112121;        /* "upper" spontaneous emission rate */
double      detl, detu;              /* detunings */
double      popdint,popd1,popdmax;
                  /* variables to keep the D-population values */
double      popdsum,popdsum1;
double      ionint,ion1;      /* variables to keep the ionisation values */
char      *program,*date;        /* strings for output documentation */
double      splin[7]={.5,0.655,.731,.756,.731,.655,.5};
```

```
double      pdlin[7]={.596,.683,.730,.745,.730,.683,.596};
double      spcir[7]={.189,.327,.462,.597,.732,.866,1.};
double      pdcir[7]={.365,.471,.577,.683,.789,.894,1.};


program="stirap0max960229j.c";
date="20011113";


psli0ii = 16.0;      /* rabi frequency */
/*      psl[1] =  1.; */      /* delay */
psl[2] =  .70;      /* pulse width */
psl[3] =  1.;        /* polarization */
detl=        8.;      /* detuning */

psui0ii = 4.8;
/*      psu[1] = -1.; */
psu[2] =  .70;
psu[3] =  1.;
detu=       -8.;

tl = -5.;            /* setting integration parameters */
tu = 5.;
h = 0.005;

/*      set up printout */

output = fopen("lin175j776","w");
fprintf(output,"IGOR\n");
fprintf(output,"WAVES\tjdelay\tjdint0\tjdint9\tjdint8\tjdint7\tjdint6
\tjdint5\tjdint4\tjdint3\tjdint2\tjdint1\n");
fprintf(output,"BEGIN\n");
```

```
Cl = initCoups();            /* initiate atomic scheme */
S = putLevel(Cl, "0", 0., 0.);      /* put in ground state, j = 1/2 */
P = putLevel(Cl, "0", 0., 0.);      /* put in first excited state j = 1 1/2 */
D = putLevel(Cl, "0", 0., 0.);      /* put in first excited state j = 2 1/2 */

addCp(Cl, S, P, 1.);      /* declare "lower" radiative coupling */
addCp(Cl, P, D, 1.);      /* declare "upper" radiative coupling */

addS0(Cl, S, P, Gl, "recoil=", 1.);  /* add spontaneous emission at rate Gl */
addS0(Cl, P, D, Gu, "recoil=", 1.); /* add spontaneous emission at rate
Gu=0.112121*Gl */

addI0(Cl, S, P, 0., 0., 0, detl);            /* declare 780 light, detuning  */
addI0(Cl, P, D, 0., 0., 0, detu);           /* declare 776 light, detuning  */

llp = LEQ(Cl);      /* make density matrix eqs. */

/*      generate auxiliary operators */

pops = LaddPopul(LallocOper(Cl), S);
popp = LaddPopul(LallocOper(Cl), P);
popd = LaddPopul(LallocOper(Cl), D);

/*      and go! */

for(v=-2.; v<=2.; v+=.1) {

psl[1] = -v;       /* delay of pulse (switched signs 20011113) */
psu[1] = v;       /* delay of pulse */

fprintf(output, "\n%.4le\t", 2*v);

psli0i =psli0ii;
psui0i =psui0ii;
```

```
for(w=1.;w>0.;w-=.1) {

psli0i=psli0i*sqrt(w);       /* changed from psl to psu 20011101  */
popdsum=0;

for(s=0;s<=6.;s+=1) {

psl[0] =psli0i*splin[s];
psu[0] =psui0i*pdlin[s];

/*      generate auxiliary operators */

      rho = LaddElem(LallocOper(Cl), S, 0, S, 0, 1., 0.);
                                     /* S(m = 0) initially populated */

/*      set up time integration */

lup = LallocUd();
LinsEUd(lup, S, P, Er, NULL, psl , 0);
LinsEUd(lup, P, D, Er, NULL, psu , 0);

popd1=LtraceProd(rho, popd);
popdint=0;

   for(t = tl; t <= tu; t += h)       {
      rk4_step_varies(llp, t, h, rho, lup);

      popd1=LtraceProd(rho, popd);
      popdint=popdint+popd1;
                        }

popdsum=popdsum+popdint*h*Gu+popd1;
```

```
} /* strength */

fprintf(output, "%.4le\t", popdsum/7);

} /* attenuation 780 */

} /* delay (v) */

/*      Finishing touch for IGOR file. */

fprintf(output, "\nEND\n");
fprintf(output, "X DefaultFont/U\"Times\"\n");
fprintf(output, "X Display jdint0 jdint9 jdint8 jdint7 jdint6 jdint5 j
dint4 jdint3 jdint2 jdint1 vs jdelay\n");
fprintf(output, "X Label bottom \"delay [1/\\F'Symbol'G\\F]0]\"\n");
fprintf(output, "X Label left \"5D excitation [Arb. units]\"\n");
fprintf(output, "X Textbox /A=MC \"%-s\\r%-s\\rom780 = %5.2f\\rwi780
=%5.2f\\rdet780=%5.2f \"\n",program,date,psli0ii,psl[2],detl);
    fprintf(output, "X AppendText    \"om776 = %5.2f\\rwi776
=%5.2f\\rdet776=%5.2f\"\n",psui0ii,psu[2],detu);

} /* main */

double      Er(t, parms)
double       t;
void      *parms;

{
double      *p;
p = (double*)parms;

return p[0]*exp( -((t-p[1])/p[2])*((t-p[1])/p[2])/2);
}
```

Appendix C

IGOR Macros

C.1 Macros Used in the STIRAP Experiment

For the STIRAP experiment the data were stored in the digital storage oscilloscope and then read into the computer via a LabVIEW program last modified by Stephen Gensemer. The data subsequently were loaded into the IGOR analysis package. A run of the STIRAP experiment produced data files of 420 nm fluorescence, of 780 nm fluorescence and of the triangle wave (produced by a Leader LFG 1300S Function Generator) controlling the delay between the STIRAP pulses. The following macros were used in the analysis.

"Checkone" takes a letter as input. This letter identifies a group of the aforementioned data files. Extraneous data points inserted by the oscilloscope (and hence not data points) are removed. The "xdat" file (x-axis data from the oscilloscope, i.e., the time axis) needs to have its values doubled due to a problem with the LabView program reading it into the computer. The times at which the ramp voltage turns around are determined. From the ramp signal the file of the time delays between the pulses is calculated. The function used is determined by taking several ramp voltage measurements as a function of pulse delay. Here is a sample from 1996/01/23 (with the atypical problems of the delay range being longer than usual and being shifted 5 ns in the intuitive order): These data are fit to a polynomial function which is used in the macro to determine the pulse delay. The ramp signal is then normalized. The 420 nm fluorescence signal and the ramp signal are displayed versus the delay.

Table C.1: Time during ramp and its associated pulse delay.

Time pulse moved [s]	Delay range covered [ns]
3.7	-100 → -60
7.99	-100 → -20
13.42	-100 → 20
20.87	-100 → 60
31.26	-100 → 100
33.44	-100 → 105

```
Macro checkone (letter4)
      string letter4
      string xdat4, ramp4, sig4, delay4

      xdat4 = letter4 + "xdat"
      ramp4 = letter4 + "ramp"
      sig4 = letter4 + "sig"
      delay4 = letter4 + "delay"

      deletepoints 254,256,$ramp4
      deletepoints 0,2,$ramp4
      deletepoints 254,256,$xdat4
      deletepoints 0,2,$xdat4
      deletepoints 254,256,$sig4
      deletepoints 0,2,$sig4

      $xdat4 = $xdat4*2
      wavestats $ramp4
      $ramp4(251) = $xdat4(V_minloc)
      $sig4(251) = $xdat4(V_maxloc)
      $xdat4 = $xdat4-(V_minloc/5)
      duplicate $xdat4 $delay4
      $delay4 = -99.1153+11.6727*$xdat4
                     -0.252309*$xdat4^2+0.00233541*$xdat4^3
      $ramp4 = $ramp4 - V_min
      wavestats $ramp4
      $ramp4 = $ramp4/V_max
      display $sig4 vs $delay4
      append/r $ramp4 vs $delay4
      deletepoints 251,251,$ramp4
      deletepoints 251,251,$sig4
```

```
        deletepoints 251,251,$xdat4
        deletepoints 251,251,$delay4

        label bottom,"Delay [ns]"
        label left,"Blue fluorescence [Arb. units]"
        label right, "Normalized ramp voltage"
        setaxis left 200,800
        modify grid(left)=2,grid(bottom)=2

EndMacro
```

The "red" macro uses the 780 nm fluorescence from the trap as input. It uses a Lorentzian smoothing algorithm and then normalizes the red fluorescence. This is done by averaging the fluorescence of a zero level, subtracting the average from the entire data set, finding the new maximum value and dividing the data by this maximum. Refer to Figures 3.4 and 3.5. Note the few rightmost points in the two 780 nm files. These give the baseline, showing the light level when the trap is absent. During the STIRAP experiment the trap was wiped out by blocking a retroreflected beam which contributed very little scattered light to the signal. This macro is used after first using "checkone".

```
Macro red (letter3)
      string letter3
      string sig3
      variable min,max

      sig3 = letter3 + "sig"

      smooth 10,$sig3
      wavestats $sig3
      min = V_min
      $sig3 = $sig3 - min
      wavestats $sig3
      max = V_max
      $sig3 = $sig3/max

      label left,"Normalized red fluorescence [Arb. units]"
      setaxis left 0,1

EndMacro
```

The 420 nm (or blue) fluorescence acquired from the experiment can only come from the atoms still trapped. As a cursory examination of the 780 nm (or red) fluorescence reveals, the number of trapped atoms changes during a run. Thus the blue fluorescence must be corrected. The "norm" macro performs this correction. It displays the previously normalized ramp files and red file ("letter2") with the blue file ("letter1") versus their respective delay files. The minimum voltage turning points of the ramp files are used as anchors to line up all the files. Then the blue file is divided by the normalized red file in order to correct for the changing number of atoms involved in the STIRAP process.

```
Macro norm (letter1 letter2)
string letter1 letter2
string xdat1, ramp1, sig1, delay1, xdat2, ramp2, sig2, delay2
variable min1, mindif

xdat1 = letter1 + "xdat"
ramp1 = letter1 + "ramp"
sig1 = letter1 + "sig"
delay1 = letter1 + "delay"
xdat2 = letter2 + "xdat"
ramp2 = letter2 + "ramp"
sig2 = letter2 + "sig"
delay2 = letter2 + "delay"

display $sig1 vs $delay1
append/r $ramp1 vs $delay1
append/r $sig2 vs $delay2
append/r $ramp2 vs $delay2
wavestats $ramp1
min1 = V_minloc
wavestats $ramp2
mindif = min1 - V_minloc

if (mindif == 0)
else
   if (mindif > 0)
            deletepoints 0,mindif,$xdat1
            deletepoints 0,mindif,$ramp1
            deletepoints 0,mindif,$sig1
            deletepoints 0,mindif,$delay1
   else
            mindif = -mindif
            deletepoints 0,mindif,$xdat2
            deletepoints 0,mindif,$ramp2
```

```
            deletepoints 0,mindif,$sig2
            deletepoints 0,mindif,$delay2
      endif
   endif

   $sig1 = $sig1/$sig2
   label bottom,"Delay [ns]"
   label left,"Corrected blue flr [Arb. units]"
   label right, "Normalized red fl & ramp voltage"
   setaxis bottom -100,110
   setaxis left 200,1000
   modify grid(left)=2,grid(bottom)=2
   Modify lstyle($sig2)=3

EndMacro
```

C.2 Macros Used in the Photoionization Experiment

As the photoionization experiment progressed, the various Igor macros developed. What are presented here are late forms. Some did not exist early on, others evolved from their crude beginnings. Some macros are particular to the lasers being used. What are presented here are those for the Kr laser at 647 nm. In the "setintensity" macro a file of power readings is adjusted by losses due to optics and then divided by the beam's area to get the intensity. In this case the Kr beam originated in another laboratory, came through a hole in the wall, bounced off some mirrors and through some lenses, going through the backside of a dielectric mirror and through a quarter wave plate and a window of the cell trap apparatus before impinging on the MOT. The power was measured before the backside of the mirror; the light was attenuated by 25% before the window.

```
   macro setintensity()
     intensity = power
     intensity = intensity * 0.75 * 0.96 * 0.96

     print "The above corrects for losses through the mirror,
               wave plate, window."
     print "The area of the Kr beam is taken to be 0.00643795 cm^2."
     intensity = intensity/  6.43795e-3
     intensity = intensity/1000
     print "the intensity is now in W/cm^2"
endmacro
```

The macro "setks" sets the variables k0 through k4 (other versions go through k5). These are used in subsequent analysis.

```
   macro setks()
print "k0 = flux/intensity, k1 = repetition rate, k2 = 5D lifetime,
          k3 = stirap efficiency,k4 = loss rate (no ion) "
  k0 = 647e-9/((6.626e-34)*(2.997925e8))
  k1 = 50000
  k2 = 241e-9
  k3 = 0.33028
  k4 = 0.893451
  print k0,k1,k2,k3,k4
endmacro
```

"Builditb" displays the trap fluorescence versus time. A letter designates a group of files of the trap under three conditions–the trap experiencing photoionization, the trap experiencing STIRAP but no photoionization, and just the trap–taken sequentially. While these files are displayed, the macros "zeroes" and "peaks" are executed, determining the zero level and the peak levels of the three conditions. Macro "zeroit" then subtracts the zero level from the peaks to determine the actual fluorescence amplitude. "Loads" models the loading of the trap as an exponential.

```
   Macro builditb(letter)
  string letter
  string dat1,dat3,dat5,x1,results

  results = letter + "results"
  dat1 = letter + "10d"
  dat3 = letter + "30d"
  dat5 = letter + "50d"
  x1 = "loadtime"
  display $dat1,$dat3,$dat5 vs $x1
  label left "\\Z09Trap flr [a.u.]"
  Textbox/C/N=text0 "\\Z09\\JCPhotoionization 19990806 Effect on Trap
Flr of Kr 647 nm, xxx mW";DelayUpdate
  Textbox/C/N=text0/F=0/E/A=MT/X=5.00/Y=5.00
  modify grid=2,standoff=0
  showinfo

EndMacro

macro zeroes(letter)
  string letter, ionz,strz,trapz,results
  ionz = letter + "0"
  strz = letter + "2"
  trapz = letter + "4"
```

```
  results = letter + "results"

  wavestats/R=[30,5999] $ionz
  $results[0]=V_Avg
  wavestats/R=[30,5999] $strz
  $results[2]=V_Avg
  wavestats/R=[30,5999] $trapz
  $results[4]=V_Avg
endmacro

macro peaks(letter)
  string letter, ionpeak,strpeak,trappeak,results
  ionpeak = letter + "1"
  strpeak = letter + "3"
  trappeak = letter + "5"
  results = letter + "results"

  wavestats/R=[3000,5999] $ionpeak
  $results[1]=V_Avg
  wavestats/R=[3000,5999] $strpeak
  $results[3]=V_Avg
  wavestats/R=[3000,5999] $trappeak
  $results[5]=V_Avg
endmacro

macro zeroit(letter)
  string letter, results

  results = letter + "results"
  $results[1] = $results[1] - $results[0]
  $results[3] = $results[3] - $results[2]
  $results[5] = $results[5] - $results[4]
endmacro

macro loads(letter)
  string letter, ionload,strload,trapload,results
  ionload = letter + "10d"
  strload = letter + "30d"
  trapload = letter + "50d"
  results = letter + "results"


  wavestats/R=(500,1999) $ionload
  curvefit exp $ionload(0,V_maxloc) /x=loadtime
  $results[6]= k2
  wavestats/R=(500,1999) $strload
  curvefit exp $strload[0,V_maxloc] /x=loadtime
  $results[7]= k2
  wavestats/R=(500,1999) $trapload
  curvefit exp $trapload[0,V_maxloc] /x=loadtime
```

```
  $results[8]= k2
endmacro
```

The "rats" macro crudely determines an average, and "rats2" builds several tables holding the trap fluorescence levels and loading rates during photoionization, just STIRAP and just normal trapping. More sophisticated methods are used in the collisions experiment (see the next section).

```
   macro rats()
  k4 = (aresults[7]+bresults[7]+...+kayresults[7])/11
  print (k4)
endmacro

macro rats2()
  ions[1]=kayresults[1]
  ions[2]=jresults[1]
  ...
  ions[11]=eresults[1]

  stiraps[1]=kayresults[3]
  stiraps[2]=jresults[3]
  ...
  stiraps[11]=eresults[3]

  traps[1]=kayresults[5]
  traps[2]=jresults[5]
  ...
  traps[11]=eresults[5]

  ionload[1]=kayresults[6]
  ionload[2]=jresults[6]
  ...
  ionload[11]=eresults[6]

  stload[1]=kayresults[7]
  stload[2]=jresults[7]
  ...
  stload[11]=eresults[7]

  trapload[1]=kayresults[8]
  trapload[2]=jresults[8]
  ...
  trapload[11]=eresults[8]

endmacro
```

The following are functions (and macros invoking them) to do the actual analysis. As described in the text, the function describing the number of atoms in the trap

as the intensity of the photoionizing light increases should go as 1/(1+x). The "x" includes a variety of factors, most notably the photoionization cross-section (c[0]) but also the variables set above by the macro "setks". The function "onemore" has a parameter c[1], which replaced k3. Sometimes it was more convenient to put the STIRAP efficiency in a file rather than set it as a variable.

```
   function oneover(c,y)
 wave c;  variable y
 return(1/(1+((c[0]*y*k0*k1*k2*k3)/k4)))
endmacro

macro dooneover(control,yfile,xfile)
  string control,yfile,xfile

  FuncFit oneover $control $yfile /X=$xfile /D
  print ($control[0])
  beep
endmacro

function onemore(c,y)
 wave c;  variable y
 return(1/(1+(c[0]*y*k0*k1*k2*c[1])/k4))
endmacro

macro doonemore(control,yfile,xfile)
  string control,yfile,xfile

  FuncFit onemore $control $yfile /X=$xfile /D
  print ($control[0])
  print ($control[1])
  beep
endmacro
```

C.3 Macros Used in the Collisions Experiment

Macro "buildload" displays a trap loading curve and the file of the baseline level, i.e., the fluorescence level when the magnetic field coils are turned off. The average level of the zero level is subtracted from the loading file, and the loading file is fit to an exponential. The parameters and their standard deviations are stored in a file.

```
 Macro buildload(trap)
 string trap,load,zero,trapdata,fit1
```

```
load = trap + "trap"
zero =  trap + "zero"
trapdata = "load" + trap
fit1 = "fit_" + load

display $load,$zero vs tyme
label left "Trap flr [arb. units]"
label bottom "Time [s]"
Textbox/C/N=text0 "\\Z09\\JCCollisions 20010613 776";DelayUpdate
Textbox/C/N=text0/F=0/E/A=MT/X=5.00/Y=5.00
modify grid=2,standoff=0

make /n=6 $trapdata
wavestats $zero
$load = $load - V_avg
CurveFit exp $load /X=tyme /D
$trapdata[0] = k0
$trapdata[1] = k1
$trapdata[2] = k2
$trapdata[3] = W_sigma[2]
$trapdata[4] = W_sigma[0]
$trapdata[5] = W_sigma[1]

ModifyGraph lstyle($fit1)=3,rgb($fit1)=(1,4,52428)

EndMacro
```

Occasionally the automated analysis in the macros does not work. For instance, in the case of "buildload" the trap may have started loading some tenths of a second after the recording of the data began, and the CurveFit function does not give the correct loading rate. "Buildload" cannot be run again, because it creates a file which cannot be created again. Thus a second macro, in this case "update," allows the user to place cursors on the loading file at appropriate places, get an accurate loading rate and not try to make a new "trapdata" file. Other macros similarly have forms which remove the "make" command or permit idiosyncratic analysis. These macros are not listed below.

```
 Macro updateload(trap)
string trap,load,trapdata

load = trap + "trap"
trapdata = "load" + trap
CurveFit exp $load(xcsr(A),xcsr(B)) /X=tyme /D
$trapdata[0] = k0
$trapdata[1] = k1
```

```
  $trapdata[2] = k2
  $trapdata[3] = W_sigma[2]
  $trapdata[4] = W_sigma[0]
  $trapdata[5] = W_sigma[1]
endmacro
```

"Loadfillit" fills up files with data from the loading curves, namely A0, A1 and A2 in the following equation:

$$fit = A0 - A1e^{A2x}. \tag{C.1}$$

The macro depends on several conventions. First, the data files must begin with the word "load" (or "loadbl" for loading files acquired with the excitation beams blocked), followed by a letter, a through e, for the five measurements taken with the same trap parameters. The digits 395 or 475 follow, indicating the trap laser detuning current in mA, and the name ends with the 776 AOM frequency in MHz. The trap laser detuning current is that which passes through a solenoid, Zeeman shifting the saturated absorption lock-point (as described in Chapter 2) of the trap laser. This changes the trap laser detuning and therefore the MOT density. A do loop builds the data file name, adjusting the name through its ASCII code (a = 97, b = 98 etc.) and AOM frequency, kept in a file named "freq". The first five entries in the data files belong to the high number density measurements, the next five to the low, when the excitation beams are blocked. The remaining entries (typically 25) are filled with the loading parameters with the excitation beams in effect.

```
 macro loadfillit()
variable i,j,lett
string loadname,loadnamelow,freq

i=0
lett=97
do
  loadname = "loadbl" + num2char(lett) + "395" + num2str(freq[i])
  loadnamelow = "loadbl" + num2char(lett) + "475" +
num2str(freq[i])
  amp1[i] = $loadname[0]
  amp1[i+5] = $loadnamelow[0]
  amp2[i] = $loadname[1]
  amp2[i+5] = $loadnamelow[1]
```

```
    load[i] = $loadname[2]
    load[i+5] = $loadnamelow[2]
    loadsigma[i] = $loadname[3]
    loadsigma[i+5] = $loadnamelow[3]
    amp1sigma[i] = $loadname[4]
    amp1sigma[i+5] = $loadnamelow[4]
    amp2sigma[i] = $loadname[5]
    amp2sigma[i+5] = $loadnamelow[5]
    lett = lett + 1
    i +=1
  while (i<5)

  i =10
  j=0
  do
    lett=97
    do
      loadname = "load" + num2char(lett) + "395" +
num2str(freq[j])
      loadnamelow = "load" + num2char(lett) + "475" +
num2str(freq[j])
      amp1[i] = $loadname[0]
      amp1[i+5] = $loadnamelow[0]
      amp2[i] = $loadname[1]
      amp2[i+5] = $loadnamelow[1]
      load[i] = $loadname[2]
      load[i+5] = $loadnamelow[2]
      loadsigma[i] = $loadname[3]
      loadsigma[i+5] = $loadnamelow[3]
      amp1sigma[i] = $loadname[4]
      amp1sigma[i+5] = $loadnamelow[4]
      amp2sigma[i] = $loadname[5]
      amp2sigma[i+5] = $loadnamelow[5]
      lett = lett + 1
      i +=1
    while (lett<102)
    i += 5
    j += 1
  while (j<5)

endmacro
```

The fluorescence amplitude must be corrected for the excited state fraction, and this is done in the "corr" macro.

```
 macro corr()
variable i,j,dens,denslow

dens = 3.075e6
denslow = 7.05e6
```

```
  i = 0
    do
      corramp[i] = ((6.6e9)*150/(dens))*amp1[i]
      corramp[i+5] = ((6.6e9)*150/(denslow))*amp1[i+5]
      i +=1
    while (i<5)
  j = 10
  do
    i = 0
    do
      corramp[i+j] = ((6.6e9)*150/(dens))*amp1[i+j]
      corramp[i+j+5] = ((6.6e9)*150/(denslow))*amp1[i+j+5]
      i +=1
    while (i<5)
    j +=10
  while ((i+j)<60)

endmacro
```

Macro "corr2" corrects the fluorescence amplitude standard deviation by the excited state fraction.

```
   macro corr2()
  variable i,j,dens,denslow

  corrsigma = amp1sigma
  dens = 3.075e6
  denslow = 7.05e6

  i = 0
    do
      corrsigma[i] = ((6.6e9)*150/(dens))*corrsigma[i]
      corrsigma[i+5] = ((6.6e9)*150/(denslow))*corrsigma[i+5]
      i +=1
    while (i<5)
  j = 10
  do
    i = 0
    do
      corrsigma[i+j] = ((6.6e9)*150/(dens))*corrsigma[i+j]
      corrsigma[i+j+5] =
((6.6e9)*150/(denslow))*corrsigma[i+j+5]
      i +=1
    while (i<5)
    j +=10
  while ((i+j)<60)

endmacro
```

"Trapfillit" fills data files with the characteristics of the trap size.

```
 macro trapfillit()
  variable i,j,lett
  string trapname,trapnamelow,freq

  i=0
  lett=97
  do
    trapname = "datazblt" + num2char(lett) + "395" +
num2str(freq[i])
    trapnamelow = "datazblt" + num2char(lett) + "475" +
num2str(freq[i])
    trapamp[i] = $trapname[0]
    trapamp[i+5] = $trapnamelow[0]
    trapampsig[i] = $trapname[1]
    trapampsig[i+5] = $trapnamelow[1]
    horrad[i] = $trapname[2]
    horrad[i+5] = $trapnamelow[2]
    verrad[i] = $trapname[3]
    verrad[i+5] = $trapnamelow[3]
    horsigma[i] = $trapname[4]
    horsigma[i+5] = $trapnamelow[4]
    versigma[i] = $trapname[5]
    versigma[i+5] = $trapnamelow[5]
    lett = lett + 1
    i +=1
  while (i<5)

  j=0
  i=10
  lett=97
    do
    print j,i,lett
      trapname = "datazt" + num2char(lett) + "395" + num2str(freq[j])
      trapnamelow = "datazt" + num2char(lett) + "475" + num2str(freq[j])
      trapamp[i] = $trapname[0]
      trapamp[i+1] = $trapnamelow[0]
      trapampsig[i] = $trapname[1]
      trapampsig[i+1] = $trapnamelow[1]
      horrad[i] = $trapname[2]
      horrad[i+1] = $trapnamelow[2]
      verrad[i] = $trapname[3]
      verrad[i+1] = $trapnamelow[3]
      horsigma[i] = $trapname[4]
      horsigma[i+1] = $trapnamelow[4]
      versigma[i] = $trapname[5]
      versigma[i+1] = $trapnamelow[5]
      lett = lett + 1
      i +=2
```

```
    j +=1
  while (lett<102)

endmacro
```

The corrected amplitudes and their standard deviations are averaged. The values for the blocked files are simply copied over.

```
 macro startdens()
variable i, j
i=0
do
  averamp[i] = corramp[i]
  averampsigma[i] = corrsigma[i]
  i += 1
while (i<10)

j=i
do
  wavestats /r=[j,j+4] corramp
  averamp[i] = V_avg
  averampsigma[i] = V_sdev
  i += 1
  j += 5
  print i,j
while (i < 20)

endmacro
```

The following macro calculates the values of Γ_0 and Γ_{5D} for the high and low trap density cases from the loading curves.

```
 macro startgamm()
variable i, j
i=0
j=0
do
  j = j + 10
  wavestats /r=[j,j+4] load
  gamma5dsig[i] = V_sdev
  gamma5d[i] = V_avg
  wavestats /r=[j+5,j+9] load
  gamma5dlow[i] = V_avg
  gamma5dsiglow[i] = V_sdev
  i += 1
while (i < 5)
wavestats /r=[0,4] load
gamma0sig = V_sdev
gamma0 = V_avg
```

```
  wavestats /r=[5,9] load
  gamma0low = V_avg
  gamma0siglow = V_sdev

endmacro
```

The "buildload" macro has to be invoked for every load file. This is done by running various macros like "dosome" below, which simply go through all of them by name, including the files when the excitation beams were blocked (macro "blocked").

```
   macro dosome()

  buildload("a395100")
  buildload("b395100")
  ...
  buildload("e39595")

endmacro

macro blocked()

  buildload("bla39580")
  buildload("blb39585")
  ...
  buildload("ble475100")

endmacro
```

The analysis requires many files to contain the trap and loading curve data. Most are made here.

```
   macro makelookie()

  make/n=60 amp1,amp2,load,loadsigma,amp1sigma,
amp2sigma,corramp,corrsigma
  make/n=20 horamp,horrad,verrad,horsigma,versigma,vol,
volsigma,dens,denssigma,trapamp,trapampsig
  duplicate dens averamp,averampsigma
  make/n=1n0,n0sig,n0low,n0siglow,gamma0,gamma0low,
gamma0sig,gamma0siglow
  make/n=5 n5d,n5dlow,gamma5d,gamma5dlow,gamma5dcalc,
gamma5dlowcalc,ratio,ratiolow
  make/n=5 n5dsig,n5dsiglow,gamma5dsig,gamma5dsiglow,
gamma5dcalcsig,gamma5dlowcalcsig,ratiosig,ratiosiglow
  edit amp1,amp2,load,loadsigma,amp1sigma,amp2sigma,
corramp,corrsigma
  edit horamp,horrad,verramp,verrad,horsigma,versigma,
```

```
vol,volsigma,dens,averamp

endmacro
```

The following macro executes several others and then builds several graphs. It is included here for historical interest, as its analysis is deficient. However, the graphs constructed are useful, once the macro "redonumber" (see below) is run.

```
 macro lookie()
variable i,j

loadfillit()
corr()
corr2()
trapfillit()
vol = (4/3) * pi * ((horrad/10^4)^2 * (verrad/10^4))
volsigma = vol*sqrt(2*(horsigma/horrad)^2 + (versigma/verrad)^2)
display vol
ModifyGraph mode=3,marker=19;DelayUpdate
ErrorBars vol Y,wave=(volsigma,volsigma)
Label left "Trap volume [cm\\S3\\M]";DelayUpdate
Textbox/N=text0/F=0/H=5/A=MT/E "\\JC20010613 Trap Volumes"

display corramp
ModifyGraph mode=3,marker=16;DelayUpdate
ErrorBars corramp Y,wave=(corrsigma,corrsigma)
modify grid = 2
ShowInfo
Textbox/N=text1/F=0/H=5/A=MT/E "\\JC20010613 Corrected Trap
Number"

display load
ModifyGraph mode=3,marker=17;DelayUpdate
ErrorBars load Y,wave=(loadsigma,loadsigma)
label left "Trap loading rates [1/s]"
modify grid=2
Textbox/N=text0/F=0/H=5/A=MT/E "\\JC20010613 Trap Loading
Rates"


startdens()
dens = averamp/vol
display dens
modify grid=2
ModifyGraph mode=3,marker=14
Label left "Density [cm\\S-3\\M]"
Textbox/C/N=text1 /F=0/H=5/A=MT/E "\\JC20010613 Trap
Densities"
```

```
    wavestats /r=[0,4] load
    gamma0sig = V_sdev
    gamma0 = V_avg
    wavestats /r=[5,9] load
    gamma0low  = V_avg
    gamma0siglow = V_sdev

  wavestats /r=[0,4] dens
  n0 = V_avg
  n0sig = V_sdev
  wavestats /r=[5,9] dens
  n0low = V_avg
  n0siglow = V_sdev
  i=0
  j=10
  do
    n5d[i] = dens[j]
    n5dsig[i] = denssigma[j]
    i += 1
    j += 2
  while (i < 5)
  i=0
  j=11
  do
    n5dlow[i] = dens[j]
    n5dsiglow[i] = denssigma[j]
    i += 1
    j += 2
  while (i < 5)

  edit gamma5d,gamma5dlow,gamma5dcalc,gamma5dlowcalc,
gamma0,gamma0low,n5d,n5dlow,ratio,ratiolow,n0,n0low
  startgamm()
  ratio = n5d/n0
  ratiolow = n5dlow/n0low
  gamma5dcalc = gamma0 * (1-ratio)/ratio
  gamma5dlowcalc = gamma0low * (1-ratiolow)/ratiolow
  gamma5d = gamma5d - gamma0
  gamma5dlow = gamma5dlow - gamma0low

  edit freq
  display gamma5dcalc,gamma5dlowcalc,gamma5d,gamma5dlow vs
freq
  ModifyGraph mode=3,marker(gamma5dcalc)=16,
marker(gamma5dlowcalc)=5;DelayUpdate
  ModifyGraph marker(gamma5d)=19,marker(gamma5dlow)=8
  label bottom "AO frequency [MHz]"
  label left "Rate [1/s]"
  modify grid = 2
  Textbox/N=text0/F=0/H=5/A=MT/E "\\JC20010613 Calculated and
```

```
Measured 5D Loss Rates"
  Legend/N=text1/J/F=0/H=5/A=RB "\\s(gamma5dcalc)
\\F'Symbol'G\\F]0\\B5d\\M calculated";DelayUpdate
  AppendText "\\s(gamma5dlowcalc) \\F'Symbol'G\\F]0\\B5d\\M low
dens., calculated";DelayUpdate
  AppendText "\\s(gamma5d) \\F'Symbol'G\\F]0\\B5d\\M
measured\r\\s(gamma5dlow) \\F'Symbol'G\\F]0\\B5d\\M low dens.,
measured";DelayUpdate
  AppendText "\\F'Symbol'G\\F]0\\B5d\M =
\\F'Symbol'G\\F]0\\B0\\M * (1 - n\\B5d\\M/n\\B0\\M)/
(n\\B5d\\M/n\\B0\\M)"
endmacro
```

The following macro prepares to execute and then executes the "goosie" macro, builds some files and fills them, and then calculates the trap volume under the several circumstances.

```
 macro dogoosie()
variable i,j,lett
string trapname,trapnamelow,freq

make/n=22500 bigx
bigx = 7*x

goosie("te395100")
goosie("td39595")
...
goosie("blte475100")

make/n=20 volz,volzsigma,horzrad,horzsigma,verzrad,verzsigma

i=0
j=0
lett=97
do
  trapname = "datazblt" + num2char(lett) + "395" +
num2str(freq[j])
  trapnamelow = "datazblt" + num2char(lett) + "475" +
num2str(freq[j])
  horzrad[i] = $trapname[2]
  horzrad[i+5] = $trapnamelow[2]
  verzrad[i] = $trapname[3]
  verzrad[i+5] = $trapnamelow[3]
  horzsigma[i] = $trapname[4]
  horzsigma[i+5] = $trapnamelow[4]
  verzsigma[i] = $trapname[5]
  verzsigma[i+5] = $trapnamelow[5]
  lett = lett + 1
  j +=1
```

```
    i +=1
  while (i<5)
  i = 12
  j=0
  lett=97
  do
    print j,i,lett
      trapname = "datazt" + num2char(lett) + "395" +
num2str(freq[j])
      trapnamelow = "datazt" + num2char(lett) + "475" +
num2str(freq[j])
      horzrad[i] = $trapname[2]
      horzrad[i+1] = $trapnamelow[2]
      verzrad[i] = $trapname[3]
      verzrad[i+1] = $trapnamelow[3]
      horzsigma[i] = $trapname[4]
      horzsigma[i+1] = $trapnamelow[4]
      verzsigma[i] = $trapname[5]
      verzsigma[i+1] = $trapnamelow[5]
      lett += 1
      i +=2
      j +=1
  while (j<5)

  volz = (4/3) * pi * ((horzrad/10^4)^2 * (verzrad/10^4))
  volzsigma = volz*sqrt(2*(horzsigma/horzrad)^2 +
(verzsigma/verzrad)^2)
  display volz
  ModifyGraph mode=3,marker=19;DelayUpdate
  Label left "Trap volume [cm\\S3\\M]";DelayUpdate
  Textbox/N=text0/F=0/H=5/A=MT/E "\\JC20010613 Trap Volumes"

endmacro
```

"Goosie" is a rather complicated macro. Its input comes from the Image program, an exported 150 × 150 pixel selection of a CCD image of the trap. The matrix-like image is put into a one dimensional array. A background value is determined and subtracted from the array. The array is multiplied by negative 1 to account for the Image program's inversion of values. The maximum value in the entire array is found. The array is searched by the findlevels function for all running averages which meet or approach the maximum. The number of points in the running average is set by the /b= parameter. These maxima are each centered in a 150-point subset which is fit to a gaussian. This gives the horizontal radius of the trap. The array is redimensioned as a two dimensional matrix, transposed and redimensioned as a one dimensional array. The above process is repeated,

but because of the transposing the gaussian fits are in the vertical direction.

```
 macro goosie(trap)
string trap,realin,hor,ver,data,horamp,veramp
variable i,j,k,m

realin = trap + "real"
hor = trap + "hor"
horamp = trap + "horamp"
ver = trap + "ver"
veramp = trap + "veramp"
data = "dataz" + trap

make/n=6 $data
make/n=22500 $realin
$realin = real($trap)
wavestats /R=[0,149] $realin
$realin = $realin - V_avg
$realin = - $realin
wavestats $realin
V_max = V_max + 1
do
  V_max = V_max - 1
  findlevels /b=3 /Q $realin,(V_max)
while(V_flag == 2)
make /n=(2*V_levelsfound) $hor
make /n=(2*V_levelsfound) $horamp

i=0
do
  print W_findlevels[i]
  j =150 * floor((W_findlevels[i])/150)
  k = j + 149
  curvefit gauss $realin[j,k] /x=bigx
  $hor[2*i] = k3
  $hor[2*i+1] = W_sigma[3]
  $horamp[2*i] = k1
  $horamp[2*i+1] = W_sigma[1]
  i += 1
while(i < V_levelsfound)
i=0
  do
    $data[0] = $data[0] + $horamp[2*i]
    $data[1] = $data[1] + ($horamp[2*i+1])^2
    $data[2] = $data[2] + $hor[2*i]
    $data[4] = $data[4] + ($hor[2*i+1])^2
    i += 1
while(i < V_levelsfound)

$data[2] = ($data[2])/i
```

```
  $data[4] = sqrt($data[4])
  m=i

  Redimension/N=(150,150) $realin
  matrixtranspose $realin
  Redimension/N=(22500) $realin
  wavestats $realin
  V_max = V_max + 1
  do
    V_max = V_max - 1
    findlevels /b=3 /Q $realin,(V_max)
  while(V_flag == 2)
  make /n=(2*V_levelsfound) $ver
  make /n=(2*V_levelsfound) $veramp

  i=0
  do
    print W_findlevels[i]
    j =150 * floor((W_findlevels[i])/150)
    k = j + 149
    curvefit gauss $realin[j,k] /x=bigx
    $veramp[2*i] = k1
    $veramp[2*i+1] = W_sigma[1]
    $ver[2*i] = k3
    $ver[2*i+1] = W_sigma[3]
    i += 1
  while(i < V_levelsfound)

  i=0
  do
    $data[0] = $data[0] + $veramp[2*i]
    $data[1] = $data[1] + ($veramp[2*i+1])^2
    $data[3] = $data[3] + $ver[2*i]
    $data[5] = $data[5] + ($ver[2*i+1])^2
    i += 1
  while(i < V_levelsfound)

  $data[0] = ($data[0])/(i+m)
  $data[1] = sqrt($data[1])
  $data[3] = ($data[3])/i
  $data[5] = sqrt($data[5])

  killwaves $realin
endmacro
```

The following macro determines the number of atoms in the high and low density traps under the conditions with and without 5D excitation. The ratio of the number of 5D atoms to those in the unexcited trap is determined. The loss rates Γ_0 and Γ_{5D} are calculated.

```
   macro redonumber()
  variable i,j

  wavestats /r=[0,4] averamp
  number0 = V_avg
  number0sig = V_sdev
  wavestats /r=[5,9] averamp
  number0low = V_avg
  number0siglow = V_sdev
  i=0
  j=10
  do
    number5d[i] = averamp[j]
    number5dsig[i] = averampsigma[j]
    i += 1
    j += 2
  while (i <5)
  i=0
  j=11
  do
    number5dlow[i] = averamp[j]
    number5dsiglow[i] = averampsigma[j]
    i += 1
    j += 2
  while (i < 5)

  rationumber = number5d/number0
  rationumbersig = rationumber*sqrt((number5dsig/number5d)^2 +
(number0sig/number0)^2)
  rationumberlow = number5dlow/number0low
  rationumbersiglow =
rationumberlow*sqrt((number5dsiglow/number5dlow)^2 +
(number0siglow/number0low)^2)

  Gnumber5dcalc = gamma0 * (1-rationumber)/rationumber
  Gnumber5dlowcalc = gamma0low * (1
rationumberlow)/rationumberlow
  Gnumber5dcalcsig =Gnumber5dcalc * sqrt((gamma0sig/gamma0)^2 +
2*((rationumbersig/rationumber)^2))
  Gnumber5dlowcalcsig = Gnumber5dlowcalc *
sqrt((gamma0siglow/gamma0low)^2 +
2*((rationumbersiglow/rationumberlow)^2))

endmacro
```

Appendix D

LabVIEW Programs

In the photoionization and collisions experiments control of the experiment and acquistion of data were largely performed by a computer running programs ("virtual instruments" or vi) in LabVIEW©, a graphical programming package written by National Instruments. Because of the graphical nature of the programs, they cannot directly be included here in any meaningful form. However, a description can be given, and that is what will be done.

The "photoionization.vi" (version 4) has the following standard settings: the channel is 0, the device number is 5 (this is where the National Instruments board is located in the computer), the GPIB address of the SRS DG 535 Pulse Generator is 15, the port controlling the magnetic field circuit is port 0 on line 2 and the port controlling the mechanical shutter used on the cw ionizing beam is port 1 on line 1, when this was used. The rate at which the data port is polled (the "scan rate") is usually 1000 times per second, which was matched by the 1 kHz low-pass frequency filter setting on the SRS SR570 Current Preamplifier. The interval over which data are acquired is typically six seconds, yielding a total of 6000 scans for one run. This vi also allows control of the starting position in time for the 780 nm STIRAP pulse (the position of the 776 nm pulse is fixed), its duration, and the size of the window in the trap period in which the STIRAP pulses came. The program comprises 18 steps. (1) The parameters of the 780 pulse are sent to the pulse generator; (2) the trap window size is set; (3) the

shutter for the ionizing beam is opened; (4) the magnetic field is turned off; (5) trap fluorescence is acquired (this is the background level); (6) the magnetic field is turned on; (7) trap fluorescence is acquired (this is a loading curve of the trap with photoionization); (8) the magnetic field is turned off; (9) the shutter is closed; (10) trap fluorescence is acquired (this is the background with STIRAP beams but without photoionization); (11) the magnetic field is turned on; (12) trap fluorescence is acquired (this is a loading curve of the trap with STIRAP); (13) the magnetic field is turned off; (14) the 780 pulse is moved away from the 776 pulse and is made much shorter, usually 5 ns instead of 39 (effectively extinguishing it); (15) trap fluorescence is acquired (this is the background for a normal trap); (16) the magnetic field is turned on; (17) trap fluorescence is acquired (this is the loading curve of a normal trap); and (18) the six files of acquired fluorescence are assembled and displayed on the monitor in graph form; the user is asked if this group of files should be saved. These files are input to Igor (see Appendix C), which subtracts the average of the appropriate background level from the loading curve and processes the various loading curves.

The "traploadanalog.vi" is a subset of the previous vi, essentially steps (13) and (15) through (18), while "trapload.vi" prepends step (2) to those steps. These vis, especially the former, were used in the collisions experiment when the 776 nm laser was detuned via its AOM. Before that method was used, the EOSI laser (776 nm master laser) was scanned by applying a small, slow (a little faster than 0.01 Hz) triangle wave to its PZT. The data in this method were collected by the "collisions.vi" (version 5).

The "collisions.vi" uses channels 0 and 1. On one channel it takes as input the TTL output from the function generator creating the triangle wave mentioned above. It performs a digital i/o (DIO) port configuration and then a DIO port

read. The pattern coming from the read is determined to be odd or even, and that result is compared to the setting of the "slope" switch on the control panel. This allows the program to start on a rising or falling slope. The program will wait for the appropriate slope should the triangle wave be in the undesired part of the waveform. When the correct slope is present, the program sounds a beep and then typically collects 3000 scans at 30 scans per second (these can be set on the control panel). Thus a run is usually about 100 seconds. During this time both trap fluorescence (sometimes at 780 nm, sometimes at 420 nm) and the two-photon spectroscopic signal are acquired. When the predetermined number of scans has been acquired, the data are presented in a graph and the user is given the option of saving the data. There are several drawbacks to this method. First, as written the program is unable to determine a turning point in the triangle wave. Thus it starts at various points on one leg of the wave if that leg has the desired slope. Presumeably, with enough time and effort (and perhaps an upgrade) it would be possible to detect the turning point, but the benefits gained may not be worth the cost. Consider that the waveform sweeps over the two-photon resonance in an ambiguous manner, i.e., two-photon resonance does not occur at the same point in the ramp from run to run. Second, the triangle wave is not a smooth, linear function in either direction. Attempts to produce such ramp voltages by computer or by specialized circuits failed. Third, even if a perfect ramp voltage could have been made, the results would still have to be correlated to the frequency of laser detuning. Often the two-photon spectroscopy was too noisy to give a reliable basis for the correlation. The present author had already moved on to the method of setting the frequency via the AOM by the time the source of the noise was removed.

ὥσπερ ξένοι χαίρουσι πατρίδα βλέπειν,

οὕτως καὶ τοῖς κάμνουσι βιβλίου τέλος.